To the Graduate Council

I am submitting herewith a thesis written by Jin-woo Jeon entitled "Synthesis, Microstructure, and Mechanical behavior of Fe-Cu composites" I have examined the final electronic copy of this thesis for form and content and recommend that it be accepted in partial fulfillment of the requirements for the degree of Master of Science, with a major in Materials Science and Engineering.

Hahn Choo
Major Professor

We have read this thesis
and recommend its acceptance:

Peter K. Liaw

Raymond A. Buchanan

Accepted for the Council:

Anne Mayhew
Vice Chancellor and Dean of Graduate studies

(Original signatures are one file with official student records)

Synthesis, Microstructure, and Mechanical behavior of Fe-Cu composites

A Thesis Presented for the
Master of Science Degree
The University of Tennessee, Knoxville

Jin-woo Jeon
December 2005

Acknowledgements

I would like to express my great appreciations to everybody who has helped me towards my master's course at the University of Tennessee (UT). Most of all, all of efforts should be attributed to Dr. Hahn Choo, the primary advisor and Dr. Peter K. Liaw, the secondary advisor, who have always discussed with me, about not only the research directions and problems, but also privative of discussions. Also, I am truly appreciated to Dr. Raymond A. Buchanan who had no reluctance to become one of my master committee professors and have kindly helped me to finish my master's dissertation.

I am greatly thankful to two neutron instrument scientist, E.C. Oliver of ENGIN-X, ISIS Facility at Rutherford Appleton Laboratory in U.K. and Bjorn Clausen of Los Alamos Neutron Science Center (LANSCE) at the Los Alamos National Laboratory for the experimental assistance and advices.

Other UT staffs members put a lot of efforts for this thesis. Dr. Jae-il Jang who helped me with nanoindentation hardness tests has to be announced first. Without Dr. Joseph E. Spruiell's advice and efforts, X-ray data could not been attained. Mr. Douglas E. Fielden and other staffs in the department mechanic shop did not have any reluctance to machine specimens and fix mechanical problems. For the SEM training and operation, I am thankful to the Mr. Greg Jones. Although I could not get right data, Dr. David C. Joy, and Dr. John R. Dunlap gave me much advices and input on the TEM observations.

In addition, I am always thankful to all of my team members, Mr. Wan-chuck Woo and Mr. Timothy Wilson, who especially helped me at LANSCE, Joe Wall, who also helped me at ISIS, Mr. Kaixiang Tao, Mrs. Elena Garlea, Dr. Chang Fan, and Dr. Hongqui Li.

Finally, I would like to acknowledge to the NSF International Materials Institutes (IMI) Program for the financial supports under Contract DMR-0231320, with Dr. Carmen Huber as the program director. The research sponsored by the Assistant Secretary for Energy Efficiency and Renewable Energy, Office of Freedom CAR and Vehicle Technologies, as part of the High Temperature Materials Laboratory User Program, Oak Ridge National Laboratory, managed by UT-Battle, LLC, for the U.S. Department of Energy under contract number DE-AC05-00OR22725.

Abstract

The synthesis, microstructure, and mechanical properties of ball-milled nanocrystalline (nc) Fe powder and immiscible Fe-Cu alloy composites are investigated in this thesis. Experimental approaches are described for the characterization of the grain size and hardness of nc Fe powders and the internal stress state of bulk Fe-Cu alloy composites are presented.

The grain size measurements of ball-milled Fe powders obtained from the XRD line broadening analysis (15 nm) and TEM observation (18 nm) showed good agreement between two results. From the nanoindentation tests, the hardness values of the ball-milled Fe powders were increased from 3.5 to 10.5 GPa as the milling time increased and the grain size decreased.

The mechanical behaviors of the coarse-grained (Regular) pure Fe, pure Cu, and Fe-Cu alloy composites were studied. The regular Fe-Cu alloy composites showed significantly higher tensile strengths than expected by a simple rule of mixture due to solid-solution strengthening effects, which were confirmed by SEM and nanoindentation tests. Finally, the intergranular strain evolution during tensile testing is investigated using the neutron *in-situ* loading measurements.

Table of Contents

List of tables

List of figures

1. Introduction

Over the past decades, the research on the behavior of metal-matrix composites has attracted automotive and aerospace industries because of their outstanding mechanical and thermal properties compared to monolithic materials. The understanding deformation mechanism has been one of the greatest interests to the material scientists and is also a focus of the current research.

Recently, nanocrystalline alloys, with grain sizes ranging from a few nano-meters to generally less than 100 nm, have been studied extensively because of their unique mechanical behavior such as enhanced strengths and hardness compared to the coarse-grained counterparts.

Based on the well-known Hall-Petch relationship [42-43], which predicts an increase in strength with a decrease in grain size, nanocrystalline alloys are expected to have exceptionally high strengths. However, many research reports have shown that their strength saturates as the grain size reaches a critical value, so-called inverse Hall-Petch relationship [77-82]. When grain size is decreased to the range of a few nanometers range, grain boundary sliding can be the dominant deformation mechanism rather than conventional dislocation pile-up mechanism. There have been numerous computer-simulation studies that are available in the literature [83, 84] to date. The understanding of the deformation mechanisms of nanocrystalline alloys and nanocomposites is the goal of this research project along with the development of synthesis and processing methods.

In Figure 1[1], detailed research plans are shown as a flow chart. The main focus is the characterization of structural and mechanical properties of nanocrystalline ball-milled Fe powder, bulk "regular" (i.e., micrometer-scale grain sized) Fe and Cu, regular Fe-Cu

1 All tables and figures are located in the Appendix

composites, and ball-milled Fe-Cu composites.

The selected material system, Fe-Cus is a thermodynamically immiscible system. The Fe-Cu alloy system has shown unique mechanical, electrical, and magnetic properties. Another benefit of the Fe-Cu system is that the iron and copper diffraction reflections in composites do not overlap, which allows us to study phase-specific composite micro-mechanics using *in-situ* neutron diffraction.

The "regular" grain-sized immiscible alloy composite system was studied as a baseline for the understanding of nanocrystalline composite behavior. In order to make the bulk-size composites, two sinter-forging consolidation temperatures (high: 1,100°C, low: 570 °C) were evaluated so far for structural and mechanical properties. In the current literature, sinter-forging consolidation method shows relatively good densities and mechanical properties when compared to other powder consolidation methods [1-2].

For the ball-milled Fe powder synthesis, a SPEX 8000D shaker mixer mill was used. In order to measure the grain size of the ball-milled powder, XRD line broadening analysis and TEM observations were performed. The hardness of ball-milled Fe powder was evaluated using nanoindentation as a function of the milling time.

The consolidation of the ball-milled composites was attempted using the same forging temperatures (high: 1,100°C, low: 570 °C) used for the regular composites. The density, grain sizes, and the mechanical properties were compared to those of the regular composites.

To probe the mechanical properties in a small area, such as the micrometer-sized phases in composites, nanoindentation hardness tests have proven to be an effective tool [3]. Furthermore, two types of stress, type□ (or macrostress) and type□ (or microstress)

can be measured simultaneously by neutron time-of-flight diffraction measurements [4-5], and the results can provide us microscopic insights into the properties of bulk materials. The understanding of type□ stresses by diffraction techniques is also useful in multiphase materials studies.

Although positive results from the bulk-sized nanocrystalline materials have not been achieved so far (shown in red color in Figure 1), current studies on the structural and mechanical properties of nanocrystalline powders, regular bulk Cu, regular bulk Fe, and their composites will be the cornerstone for the future research efforts.

2. Literature review

2.1 Nanocrystalline materials

Generally, nano, in the material science category, refers to a feature that is smaller than 0.1 μm (or 100 nm). The definition of nanocrystals is the grain size that is less than 100 nm. Because the grain sizes are very small, the nanocrystalline materials have different properties than conventional coarsed-grain sized materials. Gleiter *et al.* (in 1989) synthesized ultrafine-grained Cu using *in-situ* consolidation, and showed enhanced properties compared to coarse-grain-sized materials [10].

There are other nanostructured materials in the material science area, such as nanoparticles and nanodevices, but this literature review is mainly concerned with nanocrystalline materials' classification, synthesis, characterization, and properties. This report will especially focus on powder-metallurgy processing and mechanical properties. In addition, a literature survey was conducted for this chapter.

2.1.1 Classification

From the reference [11], the nanocrystalline materials were classified by dimensionality, which include layered, filamentary, and crystallite structures (Table 1). Almost all of the research focusing on the three-dimensional crystallites is based on the theories of one and two dimensional structures.

2.1.2 Synthesis of nanocryatalline materials

Many techniques have been developed to make nanocrystalline materials. In Table 2 [11], various techniques are categorized by the starting phase: vapor, liquid, or solid. The selection of each processing method depends on the final requirements, such as chemical composition, purity, and cost [11].

2.1.2.1 Overview of major synthesis techniques

In Table 2, the inert gas-condensation (IGC) method is one of the major processing methods for making nanocrystalline materials from the gas phase. It is similar to other methods, such as physical-vapor deposition, plasma processing, chemical vapor condensation, and chemical reactions. The IGC method, shown in Figure 2, is an *in-situ* nanocrystalline manufacturing process. The atoms are evaporated from the metal by various melting techniques and collide with the inert gas in the ultra-high vacuum (UHV) state, and then they are formed into a very fine and high-purity nanocrystalline powders. After collecting the powder, a compaction process is performed in the same UHV chamber [13-15].

The electro-deposition method is a relatively simple process for producing high quality specimens without any subsequent consolidation, which is developed by Erb. *et al.* [16]. Compared to other powder-based processing methods, this technique fabricates the nanocrystalline materials using electrochemical deposition technique with little porosity by controlling temperature, current density, pH, bath composition, etc [11].

2.1.2.2 Mechanical alloying (MA)

Mechanical alloying (or ball-milling) is one of the severe plastic deformation methods used to produce nanocrystalline powders using the processes of grinding, fracturing, and welding. There are various types of mills available for mechanical alloying, such as SPEX shaker mills, planetary ball mills, attritor mills, and other new designs [17]. The typical capacities are shown in Table 3. The basic components of the attritor mill include a rotating shaft, a tank, a jacket, and balls to grind powders (Figure 3). The benefit of the attritor mill is its ability to make a large amount of powders at one time. In addition, the rotation speed of the shaft, the coolant types, and the atmosphere inside of the tank can be controlled. By controlling these variables, we can control the grain size during milling. The most popular type of mill that can produce nanocrystals is a SPEX shaker mill (Figure 4). Using this shaker mill, the milling parameters, which can be controlled, include the milling container, milling speed, milling time, grinding media, ball-to-powder weight ratio, amount of the total input to the vial, milling atmosphere, process-control agents, and temperature of milling [13]. The choice of the milling container and grinding media can determine the extent of contamination. In addition, the shape of the container, which is round or flat ended, and the size of the container will affect the total milling time necessary. It was report that the combination of large and small size grinding balls during milling minimizes the amount of cold welding and the amount of powder coating on the surface of the balls. Typically, the ball to powder weight ratio for a SPEX mill is 10 to 1, and the extent of filling the vial is recommended to be 50% of the space [13]. When the quantity of the balls and powder is small, the quantity of nanocrystalline powders produced would be small. On the other hand, if the quantities are

too large, then there is not enough free-space for the balls and powders to move. Therefore, the impact energy of the impact will be less. The most common atmosphere used is argon gas, which prevents powder oxidization. The milling temperature can be the most important variable to determine the constitution of the milled powder. Especially for the SPEX 8000D shaker mill system, the temperature has been controlled by either circulating liquid nitrogen around the milling container or by electrically heating the vial to high temperatures.

2.1.2.3 Powder consolidation

The powder-metallurgy processing methods require a consolidation processes to make bulk nanocrystalline materials. When conventional consolidation methods, such as hot extrusion, drawing or hot isostatic pressing are employed, grain growth cannot be avoided. In addition, if the consolidation temperature is kept low to prevent the grain growth, atomic level bonding cannot be achieved. In Table 4, various consolidation methods are summarized [1]. The sinter-forging and plasma forging methods are considered as the viable methods to produce nanocrystalline materials without severe grain growths. Each processing method is summarized below,

- Hot isostatic pressing: Hot isostatic press (HIP) has two main parts: the vessel and a resistance heater. It is suitable for the consolidation of a coarse grain size material.
- Hot pressing: This technique requires a relatively low temperature compared to the sinter forging. Using this method, higher density can be achieved compared to other consolidation processes. However, it is limited by the cross sectional area

(about 1 cm^2) and requires a higher pressure than the sinter forging.

- Transformation-assisted consolidation: This method use ultra high press and specially designed large volume cell for the metastable systems which has severe volume reduction during phase transformation.
- Spark plasma sintering: This processing method uses a pulsed electric current for heating and the sintering take place by diffusion. It was reported that this method can produce nanocomposite materials. Nevertheless, the basic principles and experimental data are not well understood yet.
- Plasma pressure compaction: This is a rapid consolidation method which uses a graphite die, dc-voltage induced plasma, and pressure. It is limited to the hard-to sinter ceramic materials, such as tungsten carbide and aluminum nitride, because of the severe grain growths for the metallic materials.
- Severe plastic torsional straining: This technique can be used on both ceramics and metals, and it is performed at high pressure and at room temperature. It causes large plastic and shear deformation. However, the maximum possible thickness of the final product reported is only 0.15mm.
- Microwave sintering: This technique uses microwaves with lengths between 1mm and 1m in free space and frequencies ranging from 300 MHz to 300 GHz. It is a useful method for its faster heating rate, which could minimize grain growth. However, the reports showed that there was large grain growth, although the density was high. This method has not been successfully used to fabricate bulk specimens.
- Dynamic consolidation using shock waves: Although this method can minimize

the grain growth, the methods of controlling shock wave are not established yet. Moreover, the size limitation of specimens is about 5mm in thickness.

- Plasma forming: Generally, plasma spray has been used as a coating method. Also, the plasma state (10,000□) arc can be used to melt and deposit powders on the rotating mandrel.
- Sinter forging: Sinter forging consolidation has shown positive results on achieving [18] full density while keeping the small grain sizes in the Fe-Cu system (10% Cu). The sinter-forging system is mainly composed of three parts: the plunger, die, and thermocouples. Usually, the plunger is made of a nickel based superalloy, and the induction coils wind around a steel die [18]. The main concept of this technique is that a very high pressure is applied for a short period of time. In Table 5, the results of sinter-forged nanocrystalline Fe, using various forging parameters, are shown [10]. The minimum forging pressure at 575 °C is 525 MPa to achieve > 99 % density. More detailed descriptions of the sinter-forging process used in this study will be presented in Chapter 3.

2.1.3 Characterization of nanocrystalline materials

Figure 5 shows a two dimensional model of the nanostructured materials [10]. The crystal atoms are shown in black and the randomly organized atoms in the grain boundary regions are shown in white. Based on the reference [11], the volume fraction of atoms in grain boundary regions (C) can be expressed using:

$$C = 3\frac{\Delta}{d} \tag{1}$$

- Δ : average grain-boundary thickness
- d : average grain diameter

From the above relation, the grain-boundary volume fractions are increased when the grain size decrease to a few nanometers. Therefore, the studies on grain boundary regions are particularly important for the nanocrystalline materials research.

Normally, the grain structure of nanocrystalline materials is considered to be the same as coarse grains' structure, although smaller in size. In the grain interior "normal" crystal defects, such as dislocations and stacking faults are observed. Furthermore, severe lattice distortion often occurs in nanocrystalline materials [19] due to the super-saturation of the constituent atoms. It has also been reported that the lattice strain of the nanocrystalline materials increased with the decreasing grain size.

To characterize the nano-meter size grains, transmission electron microscope (TEM) and X-ray diffraction (XRD) are often used. TEM can reveal the direct image of grain sizes, dislocations, and stacking faults. However, the reliability of the results strongly depends on the sample preparation. XRD is a nondestructive method, and its simple procedure is favorable for obtaining average information. , There are two main methods for the grain size measurements. One is integral breadth method and the other is the Fourier analysis. The integral breadth method is based on three assumptions, which are Cauchy-Cauchy (CC), Gaussian-Gaussian (GG), and Cauchy-Gaussian (CG) [13]. The three equations are shown below:

$$\text{CC: } \beta = \frac{1}{< L >} + 2es \tag{2}$$

$$\text{GG: } \beta^2 = \frac{1}{< L >^2} + (2es)^2 \tag{3}$$

$$\text{CG: } \beta = \frac{1}{< L >} + \frac{(2es)^2}{\beta} \tag{4}$$

- β : Measured integral breadth or full width at half maximum (FWHM)
- <L> : Column length
- e : Strain
- s : 2sinθ/λ (Scherrer equation)

For the grain size measurements, normally a W-H plot and the Scherrer equation [20] are applied to above equations. The CC equation is suitable for the larger grain size and the smaller strain, whereas the GG equation is suitable for the smaller grain size and the larger strain [7].

The studies on the grain boundary region have been discussed in the literature [refs]. The basic structure is random, like the amorphous state. Although extensive research on these grain-boundary structures has been conducted, the exact properties and states have not been clearly revealed yet [11]. The grain boundary properties and structures of nanocrystalline materials may not be different from those of coarse grained materials [21, 22]. However, in Figure 6 [23], the energy state of the grain-boundary changes as the grain size changes. In addition, the computer simulation results of these grain boundary properties are summarized below [11, 24]:

- There is no long range order
- The energy distribution of grain boundaries is narrower than in bicrystals
- The grain boundary width distribution is narrower than in bicrystal
- The phases are slightly different from the glass phase

Since nanocrystalline materials have large interface areas in grain-boundary regions, the energy state of these regions is much greater than that of the grain boundary area of the coarse-grained materials. Therefore, grain growth is inevitable for the reduction of this high energy when the system is at elevated temperatures. The thermal stability of nanocrystals is important in view of the consolidation. (i.e. keeping the small grain sizes), while achieving the full density [11]. Normally, isothermal grain growth kinetics is expressed using the following two equations:

$$d^n - d_0^{\,n} = Kt \tag{5}$$

$$K = K_0 \exp(\frac{-Q}{RT}) \tag{6}$$

- d : Grain size (d_0: initial grain size)
- n : Grain growth exponent (1/n: time exponent)
- t : Time
- K : Constant (K_0: pre-exponential constant)
- Q : Activation energy for grain growth
- R : Gas constant
- T : Temperature

The ball-milled nanocrystalline Fe shows different thermal properties during

annealing [25]. Below 500°C, the activation energy for grain growth is 125kJ/mol, which is lower than the grain boundary and lattice self-diffusion-activation energy values. Whereas above 500 °C, the activation energy for grain growth is 248 KJ/mol, which is similar to that of the coarse-grained Fe. Thus, the grain-growth mechanisms of nanocrystalline materials can be different with conventional mechanisms at elevated temperatures.

Two examples which prevent grain growth in nanocrystalline materials during consolidation are summarized in the references [11, 26-27]. The first one is solute segregation at the grain boundaries of nanocrystalline materials, which was experimentally proven in the $Pd_{1-x}Zr_x$ system [26]. The other one is the pore drag. It was shown that, if there is more porosity in the TiO_2 system, grain growth was dramatically inhibited.

2.1.4 Properties of nanocrystalline materials

Since nanocrystalline materials have large interface regions, their diffusion paths are relatively short, and this enhanced diffusivity can lead to increased solid solubility limits and low-temperature sinter-ability during consolidation and increased creep rate at lower temperatures [11]. Thus, different electrical, magnetic, chemical and mechanical properties are expected compared to the conventional coarser grained materials properties research areas.

With respect to the electrical properties, ZnO nanocrystalline materials show improved electrical properties than coarse-grained ZnO [30, 31], and the giant magnetro resisstance (GMR) of nanocrystalline ZnO was also reported [30]. For magnetic and

chemical properties, nanocrystalline materials also showed different results as conventional materials [31-36]. The FINEMENT alloy (Fe-Cu-Nb-Si-B) is a good example for having excellent magnetic properties with a low coercivity, high permeability, low magnetostriction, and low core losses [11]. Nanocrystalline Ni alloy exhibited a good corrosion resistance which was better than coarse grained Ni alloy in dissolution rate.

The unique mechanical properties of nanocrystalline materials are discussed in the following section.

2.1.4.1 Elastic properties

From the early research reports [10], there is a large reduction in the elastic modulus of nanocrystalline materials. However, later reports have shown that there are little differences compared to coarse-grained materials with respect to the elastic modulus in the case of a fully dense state [37, 38]. In regarding the porous metal, new relations were considered by Boccaccini *et al.* [39]. This model is based on the previous theory of two-phase composite materials [40]. The apparent Young's modulus, E, is estimated based on the value, E_0, the elastic modulus of a fully dense material, and P, the volume fraction of pores, using:

$$E = E_0 (1 - p^{2/3})1.21s \tag{7}$$

$$S = (\frac{z}{x})^{\frac{1}{3}} \{1 + [(\frac{z}{x})^{-2} - 1]\cos^2 \alpha_d\}^{\frac{1}{2}} \tag{8}$$

- E_0 : Young's modulus of a fully dense material
- P : the volume fraction of pores

A good relationship between porosity and Young's moduli in nanocrystalline materials is established in [41]. Figure 7 exhibits the relation between the volume fraction of pores and Young's modulus. The volume fraction of the pores ranges from 0.02 to 0.35, and the investigated grain size ranges from 4 nm to 90 μm. In this research, the modulus of the 100% dense nanocrystalline Fe is almost identical to the modulus value of a coarsed-grained Fe. Also, the above model showed a good agreement with experimental results shown in Figure 7.

2.1.4.2 Hall-Petch relationship

With the decreasing grain size, simple grain size strengthening effects described by the Hall-Petch relation [42, 43] can be expected. The equation of the relation is expressed below:

$$\sigma = \sigma_0 + Kd^n \tag{9}$$

- σ : Yield strength
- σ_0 : Lattice friction stress to initiate a dislocation motion
- K : Hall-Petch constant
- d : Mean grain size
- n : Grain size exponent (typically -0.5)

Generally, this relationship can be explained on the basis of dislocation pile-up, which can act as an obstacle. However, when the grain size decreased to a few nanometer size, there cannot be a large enough number of dislocations for the pile up to occur. Therefore, the strength and hardness values can decrease after a specific grain size. It is normally

called an inverse Hall-Petch relationship.

2.1.4.3 Plasticity

There have been many studies to improve the ductility of nanocrystalline materials. However, most of the attempts were not so successful so far, except a few results. In Figure 8, typical ductility trends of nanocrystalline materials are illustrated [11]. The poor ductility was attributed to insufficient dislocation activities in the extremely small grain. However, some results show enhanced ductility [9, 44-45]. Two ceramic nanocrystalline materials, TiO_2 and CaF2, show enhanced grain-boundary diffusivities and ductility [44]. Recently, the bimodal grain size distributions have shown to increase the ductility of the ultra-fine grained materials [9]. The balance between high strength and ductility was achieved with a bimodal grain size distribution, the important factors for obtaining enhanced ductility, include high density, Figures 9 and 10, twinning as the dislocation barrier, and the existance of coarse grains showing twin boundaries, dislocations, and sub-grain boundaries.

If the elongations are up to 1,000% without necking during tension tests, the materials are showing superplastic behavior, which is related to the high strain-rate sensitivities. This unique behavior occurs at $T > 0.5\ T_m$ (melting temperature) in the conventional materials [46]. To observe this property, the grain size normally should be less than about 10 μm, and second phases must be present to hinder the grain growth at the elevated temperature [49].

In case of ultra-fine-grained materials (grain sizes are about 100 nm), super-plasticity takes place at relatively lower temperatures compared to the conventional

alloys (grain sizes are up to 1 μm), because of the combined effect of the ultra-fine grain size and enhanced diffusivity [47].

When the materials reach a certain temperatures for plastic-deformation to occur, diffusion creep becomes a dominant mechanism. The diffusion creep, enhanced by the decreased grain sizes is expressed in the following equation [48]:

$$\dot{\varepsilon} = \frac{B\Omega\sigma\delta D_{gb}}{d^3 kT}$$

- $\dot{\varepsilon}$: diffusional creep rate
- d : average grain size
- B : numerical constant
- σ : tensile stress
- Ω : atomic volume
- δ : grain boundary thickness
- D_{gb} : grain boundary diffusivity
- k : Boltzmann constant

Nanocrystalline Cu, which was produced by electro-deposition and subsequent cold rolling, showed a much larger strain rate ($1\times10^{-6}s^{-1}$) than coarse grain-Cu ($8\times10^{-9}s^{-1}$) at 0.23 T_m. This result indicates that there is a possibility of low temperature superplasticity in nanocrystals.

2.1.4.4 Deformation mechanisms

In Figure 11, the detailed deformation mechanism map is shown for various grain sizes of copper (fcc) [50]. The four regimes are determined by TEM and MD (molecular dynamics) theory model. Each of the four different areas, based on the grain sizes, is briefly explained below.

- Nano-1: By the MD simulation, there are only grain-boundaries processes, such as grain-boundary sliding, existing as the plastic deformation mechanism. Also, the simulation can predict that there is tension-compression asymmetry in the yield strength because of free-volume effects on grain boundary processes.
- Nano-2: The partial dislocations are dominant. In Reference [49], this region starts at an 8 nm in copper and 12 nm in nickel because of the different stacking fault energy. The grains can be sheared by Shockley partial dislocations, and they are absorbed in the opposite grain boundaries and then leave an intrinsic stacking fault behind. This regime cannot be present in bcc materials because they do not deform by dissociated partial dislocations.
- Ultra-fine: Lattice dislocations are nucleated in grain-boundaries and shear the grains. In the early stage of plasticity, those dislocations are piled up at the opposite boundaries. Although the conventional material's dislocations existed in the grain boundaries and inside the grain, dislocations are only in the grain boundaries.
- Traditional: This area shows the normal deformation behavior, in which dislocation sources compete with grain boundary dislocation sources for the deformation. In addition, the areas between ultra-fine and traditional areas have

not been clearly studied yet.

2.2 Metal-matrix composites

This chapter introduces the metal matrix composites (MMCs) [51]. Normally, MMCs are categorized into 3 groups based on the reinforcement types, monofilaments, whiskers, and particulates. The general idea of the MMC strengthening mechanism is that the small particles or reinforcements share the applied load or impede the dislocation motion. In order to understand the mechanical behavior, the load partitioning mechanisms between the matrix and reinforcement should be understood. A simple rule of mixture can be expressed in the equation below:

$$\sigma_a = f\,\sigma_m + (1-f)\,\sigma_r \tag{10}$$

- σ_a = Applied stress
- σ_m = Stress applied to the matrix
- σ_r = Stress applied to the reinforcement
- f = Volume fraction of the reinforcement

2.2.1 Basic models

There are four basic models for composite mechanics. These are a slab model, a shear lag model, continuous coaxial cylinder models, and finite element models [51].

The slab model is the simplest. It is composed of two continuous slabs, the matrix and the reinforcement. In this model, the rule of mixtures is dominant in all of the basic mechanical properties, such as elastic modulus, yield stress, Poisson's ratio, and shear

modulus. This model might be able to be adopted for long fiber composites. However the actual composite or at least whisker-reinforced composites cannot be described by this model.

The shear lag model is for describing loading effects on aligned short fibers and was proposed by Cox and others [52-54]. They focused on the load transfer between the matrix and reinforcement by means of interfacial shear stresses. It can roughly predict the elastic properties and the onset of plasticity, but this model is still far from the real mechanical response of composites due to the crude simplifications.

The continuous coaxial cylinder models started from the assumption that, the materials are transversely isotropic. Although this model cannot predict the realistic state of composites, it can give qualitatively good predictions. However, this model can only be used for the fiber composites and for their elastic responses.

When finite element models (FEM) are considered for MMCs (a steady state), they start from the basic equation:

$$F = Ka \tag{11}$$

- F : Force vector
- K : Stiffness
- a : Unknowns (often displacements)

For the unsteady state, above equation is changed to below

$$F(t) = Ka + Ca' + Ma'' \tag{12}$$

- C : Damping effects
- M : Mass

The basic finite element modeling (FEM) procedure consists of the five steps [51]:

(1) Identifying partial differential equation

(2) Spatial discrimination, with the volume elements

(3) Evaluation of K and F for each volume element

(4) Assembly of a set of simultaneous equations

(5) Solution of the set of equations

FEM is very useful to predict the local and global deformation of MMCs with the understanding of numerical techniques and boundary conditions [51]. However, in order to avoid these complexities, the Eshelby method [55], which is based on the volume averaged matrix stresses, is often considered.

2.2.2 Plastic deformation

The onset of yielding can be affected by the internal stress. The internal stress can be produced by the existence of reinforcement and different thermal contractions of matrix and reinforcement during manufacturing. The changes in the matrix microstructure can also affect the flow behavior of the composites.

The first strengthening mechanism to consider is dislocation strengthening. Arsenault and Shi [56] derived the following equation, which can explain the increased dislocation densities related to the thermal residual stresses and the number of reinforcement particles:

$$\Delta\rho = \frac{\Delta\alpha\Delta TNA}{b} \tag{13}$$

- Δρ : Dislocation density
- ΔαΔT : Thermal misfit strain
- N : The number of particles
- b : Burgers vector
- A : Total surface area of each particle

Miller and Humphreys [57] described a similar equation based on cube-shaped particles and the relationship between dislocation densities and particle size

$$\Delta\rho = 12\frac{\Delta\alpha\Delta Tf}{bd} \tag{14}$$

- d : Particle size
- f : Volume fraction of particle

Thus, the matrix in composites can be strengthened by increased dislocation density [87].

The second potential strengthening mechanism is the grain size refinement. Typically, MMCs have a much smaller grain size than unreinforced materials because…. The strengthening effects of decreasing the grain size is normally explained by the Hall-Petch relationship [42, 43], which is expressed below

$$\Delta\sigma_{YM} \approx \beta D^{\frac{-1}{2}} \approx \beta d^{\frac{-1}{2}} \left(\frac{1-f}{f}\right)^{\frac{1}{6}} \quad (15)$$

- D : Grain size
- β : Constant (typically around 0.1 MPa $m^{-1/2}$)
- f : Volume fraction of particle

The last one is Orowan and dispersion strengthening, which impedes dislocation motion with closely spaced particles. Normally, these effects cannot affect MMCs because of the large particle size and large spacing between particles, which are not effective dislocation barriers.

2.3 Nanoindentation hardness test

The nanoindentation, also called, ultra-low load indentation, is a unique technique to measure mechanical properties in the very small area, such as thin films, microcircuit, and individual metal powder particles. Using this well developed, accurate system, a few nN loads and nm displacements can be controlled [58].

2.3.1 Instrument overview

The nanoindentation equipment is mainly composed of three parts: the indenter with a specific geometry, a force actuator, and a indenter displacement sensor. There are 4 different types of indenters. These are pyramidal, spherical, cube-corner, and conical types. In this research, only the pyramidal indenter, (called a Berkovich indenter,) is used. The major benefit of this Berkovich tip is that it can measure mechanical properties in a very small area due to its geometrical property [58].

2.3.2 Hardness and elastic modulus measurements

The hardness and elastic modulus were measured together for the first time using a load and displacement relation in the 1970's [60, 61]. Now, the most popular methods for indentation are those developed by Oliver and Pharr [59]. The normal load and displacement curves and the scanning electron micrograph of a small nanoindentation made by a Berkovich tip are shown in the Figures 12 and 13. During the testing, the load and the displacement are continuously recorded. The Oliver-Pharr methods started from fitting the unloading curve by the power-law relation:

$$P = B\,(h - h_f)^m \tag{16}$$

- P : Load
- h : Displacement
- h_f : Final displacement
- B, m : Fitting parameter by experiment

Then, the unloading stiffness, S is defined as below

$$S = \frac{dP}{dh}(h = h_{\max}) = mB(h_{\max} - h_f)^{m-1} \tag{17}$$

As it is illustrated in the Figure 14, the contact depth, h_c can be also expressed as below:

$$h_c = h_{\max} - \varepsilon \frac{P_{\max}}{S} \tag{18}$$

- P_{max} : peak indentation load
- ε : indenter constant ($\varepsilon_{Berkovich} \approx 0.75$)

The contact area (A) can be expressed with the function of the contact depth, h_c. For the perfect geometry of the Berkovich tip, the function can be expressed by [59]:

$$A = f(h_c) \tag{19}$$

However, normally the tip size is between 10 and 100 nm because of the limitation of making a perfect sharp tip. The hardness, H, and the effective elastic modulus, E_{eff}, are expressed by [59]:

$$H = \frac{P_{\max}}{A} \tag{20}$$

$$\text{and, } E_{eff} = \frac{1}{\beta}\frac{\sqrt{\pi}}{2}\frac{S}{\sqrt{A}} \tag{21}$$

- β : indenter constant (1.034 for the Berkovich tip)

The effective elastic modulus equation show above fits well to most of the indenter and the results also showed pretty good agreement with some of the computer modeling data [3]. The value, E_{eff} is also given by [3]:

$$\frac{1}{E_{eff}} = \frac{1-\nu^2}{E} + \frac{1-\nu_i^{\,2}}{E_i} \tag{22}$$

- E : Young's modulus
- ν : Poisson's ratio
- E_i : 1141 GPa (for diamond)
- ν_i : 0.07 (for diamond)

The continuous contact stiffness(S) method [59] is applied to derive the right value from the amplifier. Using these methods, the hardness and modulus data can be obtained in one simple experiment with accuracies of better than 10% [59]. However, the above equation was only considered as sink-in, which is for the materials with perfectly elastic surfaces,

and it ignored pile-up effects during the measurement. Therefore, finite- element simulations are currently studied to determine the experimental defects.

2.4 Neutron diffraction

In this research, neutron diffraction measurements were conducted to measure the lattice strains in a multiple reflections (crystallographic orientations) of the constituent phases. A brief explanation is given below.

2.4.1 Bragg's law

The diffraction measurements are based on the Bragg's law.:

$$\lambda = 2d \sin \theta_{hkl} \tag{23}$$

The radiated wavelength (λ) is related to the lattice spacing of each hkl lattice plane (d) and the Bragg angle (θ).

2.4.2 Neutron sources

There are two different types of neutron sources that can be used for neutron-diffraction measurements. The first one is the fission reactor (steady-state nuclear reactor) and the other one is pulsed spallation neutron sources. The neutron beam at a typical reactor source goes through a crystal monochromator for a selection of a specific neutron wavelength from the polychromatic beam. However, the spallation source has the series of short pulses of neutrons consist of a wide range of wavelengths. Therefore, each wavelength is measured by traveling time to the neutron detector, and this travel time to

the detector is recorded. Therefore, it is also called a time-of-flight (TOF) technique. Thus, these TOF measurements can record the whole diffraction information at any specific diffraction angles.

2.4.3 Strain measurements

When a specimen is exposed to the incident neutron beam, the initial lattice spacing is defined as d_0 state, and the lattice strain is given as below:

$$\varepsilon_{hkl} = \frac{d_{hkl} - d_{0hkl}}{d_{0hkl}} = \frac{\Delta d_{hkl}}{d_{0hkl}} = \frac{\Delta t_{hkl}}{t_{0hkl}} \tag{24}$$

During the TOF measurement, neutrons hit the specimens. By Broglie relationship, the wavelength (λ) defined by Bragg's law is in proportion to the TOF information. Therefore, the TOF information can be converted into the lattice spacing (d) and lattice strain (ε) data.

TOF-diffractometers can be used for strain measurement in two directions, axial and transverse to the loading axis. It is used at pulsed source which can collect a large range lattice spacing of diffraction. Each detector, which can collect different angular positions of diffraction, is normally aligned at $\pm 45°$ to the loading axis.

2.4.4 Research examples

In 1998, B. Clausen *et al.* published the self-consistent modeling results of the plastic deformation of three fcc materials, which were stainless steel, copper, and aluminum [63]. As shown in Figure 15, aluminum shows the weakest elastic anisotropy,

while the stainless steel showed the strongest anisotropy. The stainless steel and copper show quite similar strain distributions. 200 and 311 showed lower stiffness compared to other reflections. However, the 200 orientation had the largest redistribution in plastic region. In the case of aluminum, the strain distribution was somewhat different to the other two fcc materials. The 111 orientation had the highest strain and 200 had the lowest strain in the plastic region in both axial and transverse directions.

E. C. Oliver *et al.* published a neutron *in-situ* loading test of low-carbon steels, which are a polycrystalline bcc material [64]. In Figure 16, the lattice strain is drawn as a function of the applied stress in the high and low carbon steel. From that result, the Poisson's ratio was calculated as 0.28 by the lattice strain of transverse and the axial direction of high carbon steel. Near the yielding point, the large strain shift was exhibited similar to low yielding point phenomenon in a typical bcc Fe. . In the Figure 17, the macroscopic and intergranular strain evolutions are shown during *in-situ* tensile testing. The model predictions agree quite well with the experimental response. In the elastic region, 110 grain families bear more stress than 310 and 200 grain family. Especially in the low carbon steel, different ferrite orientations make a difference in the internal stress. And also, relatively large shift in intergranular strain in the transverse axis was related to the competition between elastic and plastic anisotropy.

2.5 Immiscible Fe-Cu system

In this section, thermodynamically immiscible metal alloys, which have low positive ΔH in the liquid state and little solubility at room temperature, are going to be described [65].

The immiscible alloys are being studied for the potential applications in the giant magnetroresistance and for the formation of self-assembled lateral multilayer [66, 67]. Numerous research issues of the amorphous immiscible system were introduced, such as alloying formation mechanism and microstructures [65]. However, in this review only polycrystalline materials with the positive ΔH were considered.

Normally the binary polycrystalline immiscible system materials, such as Ag-Cu, Cu-Cr and Fe-Cu, are made via the quenching route. The equilibrium binary phase diagram of Fe-Cu system is shown in Figure 18. When this system is made, usually two phases, which are Fe based bcc phase and Cu based fcc phase, are competing with each other for the meta-stable solid solution. Figure19 shows the phase boundaries for the entire composition of Fe and Cu obtained by liquid quenching (b), thermal evaporation (c), sputtering (d), sputtering on cryogenic substrates (e), and mechanical alloying (f). Based of this figure, the phase selections depend on the processing route. Note that the technique based on the vapor route can give wider single phase region, while the liquid quenching route shows a wider two phase mixture regions.

In 1990s, the mechanical alloying (MA) was extensively used for alloying immiscible systems [17,70] As the equilibrium phase diagram of Fe-Cu system shows, there is little solubility of Cu in Fe (vice versa) at room temperature. However, the MA processing made alloying possible, and its alloying process is shown in Figure 20 [71]. Also, it was studied by using conversion X-ray Mossbauer spectroscopy (CXMS). The CXMS is the thickness-modified Mossbauer spectroscopy, which can exactly predict where the alloying occurs during the MA processing. This result of the $Fe_{50}Cu_{50}$ alloy is shown in the Figure 21. Three phases are shown and the most majority phase is fcc-FeCu,

and small amount of bcc and fcc Fe phases were developed. Other groups published the atomic-scale alloying in the FeCu composite [72, 73]. In addition, to prevent the inhomogeneity of the phase during the MA processing, cold MA processing, using liquid nitrogen, has been considered [70, 74].

3. Experimental procedure

In this chapter, the experimental procedures for the synthesis of powder, consolidation processing, microstructural and mechanical behavior characterization are discussed for the iron-copper alloy composites and their monolithic constituents. The nano-crystalline powder specimens are manufactured using ball milling. The as-received and ball-milled powder specimens were consolidated using sinter-forging process. Optical and scanning-electron microscopy (OM, SEM) and x-ray diffraction (XRD) were used to study microstructure of ball-milled powder and consolidated samples. Nanoindentation hardness test and *in-situ* neutron tensile loading measurements were performed for the mechanical properties characterization.

3.1 Powder synthesis

As mentioned in previous chapters, Fe-Cu systems were chosen for this research (see Figure 1). Two types of alloy composites were processed: a regular, coarse grained composite and ball-milled powder composite. First, a regular, coarse-grained composite was produced using as-received Fe and Cu powders. To make the regular composite, as-received metal powders purchased from Alfa Aesar Inc., (Fe: 99.9 %, spherical, <10 μm particle size ; Cu : 99.9 %, spherical, about 10 μm particle size), were consolidated using the sinter-forging technique. The details of the consolidation processing are explained in Chapter 3.2.

To make the ball-milled composites, 70 vol. % ball-milled iron powders and 30 vol. % as-received copper powders were used. For the ball-milling process, SPEX 8000D

mixer mill (SPEX Industries Inc., Metuchen, NJ), Figure 22 (a), was used with two stainless steel vial sets. Stainless steel balls were used as grinding media, Figure 22 (b). A total weight of 5.9 g of 6.4 mm diameter hardened-stainless steel balls and 5.9 g of iron powder were mixed and sealed in the hardened stainless steel vials in a glove box. The glove box is filled with purified argon gas to prevent oxidation of the powder specimens during milling.

The mixture of the grinding balls and iron powders were milled for times ranging from 10 hours to 100 hours. Ball-milled iron powders (about 5 g from each vial) were periodically collected in the glove box. The rest of the input (about 0.9 g) coated the surface of the grinding balls and the vial. The ball-milled powders were sieved using 100-μm mesh to screen large agglomerated particle chunks.

3.2 Consolidation

3.2.1 Specimens

All of the specimens and their conditions are shown in Table 6. Three different kinds of metal powders; as-received Fe, as-received Cu, and ball-milled Fe; were used as starting materials. The ball-milled Fe powders were made from as-received Fe to characterize the structural and mechanical properties of nanocrystalline Fe powder. As-received Fe and Cu powders were used to make bulk Fe and Cu as well as regular Fe-Cu alloy composites; AR70/30 (high temperature forging), AR50/50 (high temperature forging), and AR70/30 (low temperature forging). Finally, ball-milled Fe-regular Cu alloy composites were also fabricated; BM70/30 (high temperature forging) and BM70/30 (low

temperature forging).

3.2.2 Sinter-forging process

To blend two different kinds of powders (i.e., Fe & Cu), the SPEX 8000 D mixer mill was used without grinding balls. Based on the experience, however, there was not so much of a difference between mixing using SPEX mill or by hand. When the powders were mixed in the SPEX mill, about 30 % of the total vial volume was filled with iron and copper powders (Fe 30 g and Cu 15 g for 70/30 vol. % mixture). Blending inside the glove box was repeated to collect about 600g of the powder mixture. On the other hand, when the powders were mixed by hand, total amounts of Fe and Cu powders (about 600g) are poured into a large plastic jar and then sealed in the argon atmosphere. The jar was shaken by hand for about 1 hour. After the consolidation, little difference was noticed in the homogeneity of the surface and inside of an ingot as observed by the SEM.

When making ingots using powder, two major issues were considered: achieving the full density and preventing grain growth. The sinter-forging consolidation process is illustrated in Figure 23 and the five main steps are summarized below:

(a) Pressing the preform: The powder was poured into an elastomer bag, and the bag was evacuated. Then the powder was consolidated at room temperature under about 350MPa pressure using a cold isostatic press.

(b) Preheating the preform: The perform, soaked in the preheated die cavity, was heated to a target temperature (1,000 ~ 1,100 °C or 570 °C) within 10 to 15 minutes.

(c) Preheating the Pressure Transmitting Media (PTM): A carbon-based PTM was

used to apply quasi-isostatic pressure on heated samples via a fluidized bed technique at a target temperature. It also provides a reducing atmosphere in which the forging preform is protected from oxidation. In addition, different types of pressure transmitting media can be applied depending on the material being consolidated.

(d) Consolidating the preform in the Pressure Transmitting Media (PTM): The PTM is used to put the quasi-isostatic pressure on the heated specimen. The preheated PTM and the specimen preform are filled in a pot die, and then the forging ram is forged into the pot die with 483 MPa stress.

(e) Separating the PTM and the consolidated part. Finally, specimens (e.g., tensile specimens as shown in Figure 24) were machined for characterization.

3.3 Microstructure characterization

The morphology changes of the ball-milled powder particles were observed in the SEM. The changes in grain sizes were investigated as a function of the milling time using the Philips X' Pert XRD using CuK_α radiation ($\lambda_{K\alpha1}$=1.54056□ and $\lambda_{K\alpha2}$=1.54439□).

As mentioned in the literature review, there are two major methods to measure grain size in nanocrystalline materials. Although TEM observation is a direct method, x-ray diffraction (XRD) analysis is widely used to measure average grain size because it is nondestructive and requires simple sample preparation. However, XRD analysis is sensitive to the processing history of materials. Generally, there are two analysis methods: integral breadth methods and Fourier analysis. The details of the methods are mentioned in the section 2.1.3. For our ball-milled Fe powders, the integral breadth

methods with the Gaussian assumption using Williamson-Hall plot was used [7].

There are three major sources that affect the FWHM: instrument, strain, and grain size. To subtract the instrument and strain effects on the measured FWHM, silicon standard 640b and Williamson-Hall plot were used. Figure 25 (a) shows FWHM vs. diffraction angles of Si640b. After linear-fitting of the graph, Y intercept value is taken as the instrument broadening value. As a similar method, the Y intercept value was taken at the strain broadening effect in Williamson-Hall plot, Figure 25 (b). After removing the two effects, the grain-size broadening effect is expected from the XRD peak widths. The Scherrer equation and Gaussian-Gaussian assumption [7] were used to determine the grain sizes as described in section 2.1.3.

Although it is difficult to make powder specimens and estimate average grain size from small thin specimen area, direct TEM observation is necessary to confirm XRD results.

There are several powder specimen preparation methods which include dimpling and ion milling, twin jet polishing after consolidation at room temperature or embedded in a thin foil, mechanical polishing with the tripod polisher, and dispersing powder onto a grid in ultra sonic cleaner. Dispersion of powders using ultra-sonic cleaner was successful in achieving enough thin specimen areas for the TEM observation. Briefly, its procedure is illustrated in Figure 26. The agglomerated ball-milled powders dispersed in methanol were stirred in ultrasonic system for about 10 minutes and then, drop the powders in the carbon taped copper grid.

For the consolidated samples, OM, SEM, and XRD were used to investigate grain sizes and porosities. Energy-dispersive x-ray spectroscopy (EDX) was used to

characterize impurity contamination.

For grinding and polishing, a Buehler Ecomet Variable-Speed Grinder Polisher and 400, 600, 800, 1200 grit papers were used. After grinding, three steps of polishing were performed using micro cloth and 9, 1, and 0.05-μm alumina pastes. To etch the surface of pure iron, 2ml HNO_3 and 98ml methanol was used. Also, to attack grain boundaries, a mixture of Fe $(NO_3)_3$ 5 g, 25 ml HCl, and 70 ml distill water was used.

Neutron diffraction patterns of the consolidated specimens were studied for phase analysis by Rietveld analysis using GSAS (General Structure Analysis System) program [85], which provides average lattice parameters and phase fractions of the constituent phases. More details will be discussed in section 3.4.3.

3.4 Mechanical tests

3.4.1 Nanoindentation test

The hardness of the ball-milled powder and consolidated specimens were measured using an MTS Nanoindenter-XP with a Berkovich triangular pyramid indenter tip whose center line to face angle (Ψ) is 65.3°. The nanoindentation instrument system is composed of three parts; indenter, force actuator, and indenter displacement sensor, Figure 27 [3]. All of the measurements were performed using a 50 mN maximum load and a constant strain rate of 0.01 /s following the Oliver-Pharr method [3]. Generally, between 10 to 20 indentation measurements were performed on each specimen. After the test, SEM was used to examine the indentation area and to observe the absence of crack near the edge of the indentation.

The procedure for the preparation of powder specimens is shown in Figure 28. The first procedure is making epoxy disk with a shallow hole (about 5-mm depths and 5-mm diameter). The purpose of making the hole is to increase the number of powder particles in the small area for several indentation tests. Second, a mixture of epoxy gel and ball-milled Fe powders is packed in the hole, and then ground and polished. The last procedure is the indentation test on the polished particles.

For the consolidated specimens, the general method for mounting, grinding, and polishing was used. The most important issue is to make the surface parallel to the side face of the epoxy disk to achieve a precise triangle indenter shape during the test.

3.4.2 Tensile tests

The tensile tests were performed using an 810 Material Test Systems (MTS) with 647 hydraulic wedge grips at room temperature. The specimens were optimized for neutron diffraction tensile tests and their geometries are illustrated in Figure 24. During the tensile testing displacement control was used and the initial strain rate was 10^{-4} /sec. The strain gauge was removed after 3% strain.

3.4.3 *In-situ* neutron diffraction tensile loading measurements

The neutron diffraction measurements were performed at ISIS, at the Rutherford Appleton Laboratory, in the UK using the ENGIN-X instrument and also at the Manuel Lujan Jr. Neutron Scattering Center at the Los Alamos Neutron Scattering Center (LANSCE), USA using the SMARTS instrument.

At ISIS, flat tensile specimen and wedge grips were used. The tensile specimen

geometry, Figure 24, was decided with a consideration of size limitation of forging process and avoiding beam shadowing effects from the specimen grips during the neutron measurements. In Figure 29, the tensile specimen, wedge grips, and extensometer used in ISIS neutron loading measurements are shown. ARFe, AR70/30 and BM70/30 specimens were tested using load control. The neutron diffraction measurement times during the loadings for the three specimens were 3 minutes for ARFe and 10 minutes for composites, respectively.

At LANSCE ARFe, ARCu, AR70/30, and AR50/50 were tested. During the LANSCE experiment, pin-hole grip sets, made of tool steel and tungsten carbide pins, were used to avoid any bending effects on samples imposed by the heavy grips. For each diffraction pattern from monolithic specimens and composites, 20-minute and 25–minute counting times were decided by monitoring the changes in the error bar of the lattice parameter, respectively. During the loading, load-control was used in the elastic region. Prior to reaching the plastic region, load-control was changed to the displacement control to scan the plastic deformation region, which did not show much hardening with increasing stress. Furthermore, displacement control was necessary for the ARFe and AR70/30 specimens, which showed low-yield point regions. Two or three unloading measurements were performed for each specimen to measure residual strain. The scattering geometry, illustrating the sample orientation and neutron beams, is shown in Figure 30. Both ENGIN-X and SMARTS instruments have two detector banks which measure the flight times of the diffracted neutrons. The tensile loading axis is oriented 45º to the incident neutron beam and each detector bank is oriented ±90º to incident beam in order to measure the lattice strains in the parallel and perpendicular to the loading

direction.

The neutron-diffraction spectra were analyzed by Rietveld analysis using the GSAS (General Structure Analysis System) [85] program, which can fit the whole diffraction pattern, to determine the average lattice strain. Figure 31 shows the fitted diffraction patterns of pure Cu under 10 MPa in the transverse direction (upper) and axial direction (down). The x-axis is the d-spacing and the y-axis is normalized intensity. The red colored crosses represent the measured data, and the green line through the crosses is fitted data. The difference between measured and fitted data was shown with magenta color below the diffraction profile. The red tick marks represent calculated positions of the Cu peak, and the black tick marks are for the Cu oxide peak position. For the specific hkl strain determination, the GSAS Rawplot single peak-fitting program and the equation (24) were used.

4. Results and discussion

The result and discussion part consists of two sections: (1) characterization of ball-milled nanocrystalline Fe powder for structural and mechanical properties and (2) characterization of structural and mechanical properties for consolidated materials.

4.1 As-received and ball-milled powder characterization

For the characterization of grain sizes and mechanical properties of the ball-milled powders, two main issues are considered in this research. First, the measurements of the grain sizes of nanocrystalline Fe powders were performed using x-ray line-broadening measurements and TEM observations. The results can also help finding minimum ball-milling time for the smallest grain size in our ball-milling system. Second, the characterization of the mechanical properties of nanocrystalline Fe powders was performed using nanoindentation hardness tests. The morphology of the Fe powders changes as a function of the ball-milling time, Figure 32. The initial as-received iron powder particle size was about 5μm and the shape was spherical. The SEM pictures show that the particle size was increased to about 30 μm as the milling time increased to 60 hours. The shape was changed from spherical particles of as-received powders to more irregular shape after 10-hr, 30-hr, and 60–hr milling.

4.1.1 Grain size estimation

Figure 33 shows the changes in peak broadening of pure iron powders as a function of the milling time. From the diffraction pattern, 10-hr milled specimen shows a

significant peak broadening compared to the as received one. It continued to broaden and then seems to saturate after 30 hours of milling. It was noticed that the FWHM of 30-hour milled specimen was slightly larger than 60-hr one. Figure 34 summarizes the changes in the grain sizes of the ball-milled Fe powders as a function of the milling time. The results show that the grain sizes of the ball-milled iron powders saturated at about 15nm.

In Figure 35, the TEM bright field image (a) and the diffraction pattern (b) are shown. From the continuous ring pattern in the diffraction pattern, the decreased grain size can be expected. In order to measure the grain size a total of 200 grains were counted and the average grain size was about 18 nm, Figure 35 (c), which is similar to the 15 nm grain size estimated from the XRD results. Thus, the XRD line broadening analysis based on the Gaussian assumption can be continuously used to measure grain size of ball-milled Fe powder instead of TEM observation.

4.1.2 Hardness of the ball-millled powders

To characherize the mechanical property of ball-milled Fe powder, nanoindentation hardness tests were performed on the ball-milled and as-received powder specimens.

Figure 36 (a) shows the load vs. displacement curves of the as-received (blue, dotted line) and 30 hr ball-milled (red, solid line) powders. From the curve, the displacements into the surface in as-received (h0) and 30-hr. ball-milled powder (h30) can be compared. At the same load state, 30 hr. ball-milled value (h30) was smaller than the as-received value (h0), which indicates that the hardness was increased often the ball

milling for 30 hours.

The hardness values are obtained as a function of milling time using the Oliver-Pharr method [3], which describes the relationship between the displacement and applied load. The hardness of powder samples as a function of the different milling times are illustrated in the Figure 36 (b). The hardness was increased as the milling time increased initially. The hardness of the as-received Fe powder is about 3.5 GPa and the sample with 30 hr. milling time showed the highest value of about 10.5 GPa. The overall tendency shows saturation near 10 GPa after 10 hr. milling time.

4.1.3 Grain size vs. hardness

In Figure 37 (a), the grain size and hardness are shown as a function of the ball-milling time. When the grain sizes were saturated after about 10-hr milling time, there were also almost no changes in the hardness values.

In Figure 37 (b), the hardness is shown as a function of the grain size. Although only three data points were shown [42-43], the observed hardness value were increased to 10.5 GPa for 15 nm grain sizes following the Hall-Petch relation. In comparison to the data by Jang *et al.* [62], our result showed simillar trends in terms of the increased hardness values as decreased grain sizes. When our data are linear-fitted, a slope was smaller than the results of Jang *et al.* [62], Figure 38. It might be due to our insufficient data points to plot Hall-Petch curve. From the result [62], it was indicated that the hardness increased down to the 18nm grain size. Also, in Figure 38, inverse Hall-Petch relation [77-82] was exhibited below 18 nm grain size due to the grain boundary aided deformation.

4.2 Characterization of the consolidated materials

The seven bulk specimens listed in Table 6 were consolidated using sinterforging process. From the data of the two monolithic materials, ARFe and ARCu, the sinterforging consolidation conditions will be evaluated. The microstructural and mechanical properties will be used as a baseline for the Fe-Cu alloy composites. The mechanical behavior of three regular Fe-Cu alloy composites, (AR70/30, AR50/50, and AR70/30 (LT)) and 2 ball-milled Fe-Cu alloy composites, (BM70/30 and BM70/30(LT)) will be discussed.

4.2.1 Monolithic Cu

After the consolidation, the density was measured based on the Archimedes methods. In Figure 39, the densities of seven consolidated specimens are shown. The black symbols represent the calculated values based on the rule of mixture. The density of ARCu, compared to a literate value (8.96 g / cm^3), was 97.3 %. In the SEM micrograph, Figure 40, small particles were dispersed in the Cu matrix. Based on the EDX results (not shown here), it was identified as copper oxide particles, which might have been introduced during the consolidation. The presence of the copper oxide, Cu_2O was further identified in the neutron diffraction pattern, Figure 41. Each individual peak of Cu_2O (110, 111, 200, 211, and 220) was indexed in the Figure 41.

The structure of Cu_2O, cuprite structure is shown in Figure 42. The oxygen atom is positioned at the 1/4 1/4 1/4 and 3/4 3/4 3/4 in the face-centered-cubic (fcc) Cu lattice. The vol. % of Cu_2O was estimated based on the measured density of ARCu:

$$\rho_{ave} = \frac{C_{Cu}A_{Cu} + C_{Cu_2O}A_{Cu_2O}}{\frac{C_{Cu}A_{Cu}}{\rho_{Cu}} + \frac{C_{Cu_2O}A_{Cu_2O}}{\rho_{Cu_2O}}} \quad (25)$$

- C : Atomic % ($C_{Cu} + C_{Cu_2O} = 1$)
- A : Atomic weight or molecular weight (Cu: 63.546, Cu_2O: 143.091)
- ρ : Density (Cu: 8.96g/cm^3, Cu_2O : 6 g/cm^3)

After converting the atomic % to vol. %, the vol. % of Cu_2O was about 8 % based on assumption of the full density of ARCu specimen. Based on the SEM picture, Figure 40, the volume % of Cu_2O was estimated using two diagonal line interception method and area measurements. The average value of 6 different estimations was about 7.6 %. Also, the vol. % of Cu_2O was calculated from the Rietveld analysis, Figure 31. After fitting the pattern in the both transverse and axial direction, the vol. % of Cu_2O was 3.1 vol. % and 3.4 vol. %. Thus, the vol. % of Cu_2O from the neutron diffraction was estimated as about 3.3 %. The two volume fraction measurement of Cu_2O, density based calculation and microscope estimation were not so much different. However, the results from Rietveld analysis showed quite a different result. The discrepancy may be due to the fact that the specimens are made from different parts of the ingot and indicate a hetero-geneous distribution of the Cu_2O phase. When the ingot is forged, the outside parts which are used for density measurement and microstructure observation were oxidized more than the inside of the ingot which was used to make tensile specimen for neutron diffraction measurements. Overall, the bulk monolithic Cu specimen contains about 3 ~

8 % Cu_2O.

The presence of Cu_2O affects the tensile properties of ARCu specimens. Figure 43 shows the engineering stress-strain curve. The tensile test showed decreased values of elastic modulus, yield stress, ultimate tensile stress, and elongation % to fracture compared to the fully annealed state pure Cu. The values are summarized in Table 7. When the values are compared to the fully annealed state reference specimen, the elastic modulus and the elongation to fracture were severely decreased. The elastic modulus decreased from 130 GPa to 94 GPa and the elongation decreased from 45 % to 10 % possibly due to the Cu_2O effect.

Using the Rietveld analysis, the stress vs. lattice strain curve was drawn for the Cu phase in Figure 44. Although we couldn't get the average lattice strain data of Cu_2O due to the difficulties of Rietveld refinement of the Cu_2O phase, we can expect the influence on the Cu matrix phase using Figure 44. After 50 MPa we found the decrease of the slope which means the Cu yielding. The decrease of slope was continued until about 105 MPa and then it seems to takes load again.

Figure 45 shows the intergranular lattice strains measured from both Cu and Cu_2O phases along the axial direction (a) and transverse direction (b). The 111 and 220 peaks with relatively high intensities were used to measure intergranular strains of Cu_2O particles in the Cu matrix. We can see 111 and 220 of Cu_2O showed the softest reflectios in plastic region among the seven grain families, otherwise Cu 111 and 220 relfections show the stiffest response.

4.2.2 Monolithic Fe

The density measurements of the ARFe specimen were performed by same measurement as ARFe specimen. The density of ARFe was about 99.7 %, Fig 43. This near full density values can be result in the ductility and elastic modulus, Table 7. When the elongation and the elastic modulus is compared to the book value of fully annealed state pure Fe, they were reasonably close to the reference material. However, the yield stress and ultimate tensile stress showed much larger values than the reference data. In yield stress, the sinterforged sample showed 270 % increase, compared to the reference. It might be due to the grain size strengthening effects. After consolidation, the average grain size was about 15 μm.

During the tensile test, the yield phenomenon was observed. The upper and lower yield point regions are marked with a yellow circle in Figure 46 (a). The yielding phenomenon generally occurs in the bcc iron based alloys due to the solute atoms or vacancy interactions with the lattice dislocation. When it happens, Lüders bands appear. Several bands propagate in the low yield point region until the deformation spreads to the whole gauge length. Then, the homogeneous deformation starts at the end of the low yield point region.

In order to explain the intergranular strain evolution during the yielding phenomenon, the macroscopic stress-strain curve is divided based on the dislocation activities, Figure 46 (b). Before the upper yield point is reached, solute atoms strongly attracted to dislocations. With the increase in the applied load, a number of dislocations start to move through the lattice. The mobility of dislocations is continuously increased and then the load starts to drop to the $\boldsymbol{e1}$. For the dislocation to be completely free from

the solute atoms, the constant stress is applied during low yielding point region until ***e2***. After that, the homogeneous deformation starts from the ***e2***.

In order to measure lattice strain evolution during the yielding phenomenon, the *in-situ* neutron loading measurement was conducted under the displacement control. The Figure 46 (b) shows the magnified upper and low yielding point regions. The lattice strain evolution was monitored during ***a*→ *b*→ *c*→ *d*→ *e1*→ *e2*** in Figure 46 (b).

Figure 47 (a) exhibited the lattice strain change of ARFe in the transverse and axial direction. In the axial direction, Figure 47 (b), lattice strain decrease was clearly exhibited in the low yielding point region, ***e1*** → ***e2***. The lattice starts to plastically deform earlier than the upper yielding point, ***d***. The plastic deformation might start after point ***a*** and the slope of the stress strain curve increase more after point ***b***. The slope changed to negative between the ***c*** and the upper yielding point, ***d***. The movement direction of lattice strain was negative in the low yielding point. The lattice strain is continuously decreased and relaxed until the end of low yield point, ***e2*** Figure 47 (b). This procedure can be explained by dislocation activity. Before the ***c*** point, dislocation activities were more increased after ***a*** point. However, the numbers of dislocations were presumably insufficient to strong influence on the Fe lattice. After the ***c*** point, the accelerated dislocations start to be free from the solute atoms to give relaxation of the Fe lattice. Thus, the Fe lattice strains were shown as decrease until the most of the dislocations were free from the solute atoms before the homogeneous plastic deformation.

4.2.3 Regular composites

The density of three regular composites, AR70/30, AR50/50, and AR70/30(LT) were 99.8%, 100%, and 97.4%, Figure 39. Two high temperature forged specimens showed almost full densities, but the low-temperature forged specimen, AR70/30 (LT), exhibited the lowest density among the seven specimens indicating that the 570 °C forging temperature was not high enough to consolidate the material. The low density of AR70/30 (LT) affects the tensile behavior as shown in Figure 48. When it is compared to the tensile behavior of the AR70/30, the yield stress was decreased about 30%. Also, the specimen was broken near 0.45% elongation.

Figure 49 shows the tensile behavior of four specimens; ARFe, ARCu, AR70/30, and AR50/50; which are consolidated at the high temperature, 1,000 ~ 1,100 °C. Before the tensile test, the yield stress and ultimate tensile stress of the composites were expected to be in between the values of the ARFe and the ARCu based on the ROM of the Fe and Cu. Based on the simple rule of mixture, the yield stress of AR50/50 and AR70/30 were expected to 180 MPa and 260 MPa, respectively. However, the yield stresses of two composites were much higher than the yield stress of the pure Fe. The yield strengths of AR50/50 and AR70/30 were increased to 400 MPa about 220 % and to 450 MPa about 170 %, respectively.

When the two composites, AR50/50 and AR70/30, are compared to the tensile properties of Fe-Cu 50/50 vol. % and Fe-Cu 83/17 vol. % by Daymond *et al.* [86], they exhibited similar trends. The increase in tensile strength with the volume fractions is due to the thermal residual stresses between Fe and Cu. Since the Cu yielded at the lower stress state than Fe phase, the compressive residual stress on Fe phase was removed. Thus,

it was suggested that the Fe in the relatively Cu-rich specimen, AR50/50, was strongly affected by Cu matrix [86]. On the other hand, the Fe in the AR70/30 might be less affected by Cu phase. Thus, the yielding phenomenon of AR70/30 showed similar as ARFe specimen shown in Figure 49.

In addition to the thermal residual stress strengthening mechanism on Fe-Cu alloy composites presented by Daymond *et al.* [86], we will describe another strengthening effect of Fe-Cu composites based on the assumption of the solid solution strengthening.

From the EDX results of AR70/30, in Figure 50, 5 at. % Cu was detected in the Fe matrix. Based on the phase diagram, there are about 6 at. % solubility of Cu in Fe. Also, about 7.5 at. % Fe was detected in Cu phase on AR70/30 specimen, Figure 51. When it is calculated using the phase diagram, the Fe solubility in Cu phase was calculated to be 4 at. %. The calculations were performed based on the non-equilibrium cooling, such as quenching from the consolidation temperature, about 1,050 °C. During the sinterforging consolidation, the specimens were removed from the die mold after forging and then cooled down from 1050 °C in the air. Therefore, the fast cooling process makes solubility in each phase.

In order to investigate the possible solid solution strengthening, nanoindentation hardness measurements were performed on each phase in AR70/30, ARFe, and ARCu. The hardness value of ARFe and ARCu were 2.9 GPa and 1.4 GPa, respectively. The hardness of Fe was 4.0 GPa and the Cu was about 2.1 GPa in the AR70/30 specimen. The hardness of Fe in AR70/30 was increased about 33% and the hardness of Cu in AR70/30 was increased about 50% compared to the ARFe and ARCu specimens, Figure 52. Thus, the increased hardness and tensile value of the AR70/30 and AR50/50 composites may

have been influenced by the solid solution strengthening effects in Fe-Cu alloy composites.

In-situ neutron diffraction loading measurements were performed to investigate the intergranular strains. In Figure 53, the neutron diffraction patterns of AR50/50 (a) and AR70/30 (b) are shown. Similar to the diffraction pattern of ARCu, (Figure 41), the Cu_2O peaks were found in the composites as well. Although the intensities of Cu_2O peaks were not as strong as ARCu, two reflections, (Cu_2O 200 and 220 peaks) are marked in Figure 53 (a) and (b). The lattice strains measured from the two peaks are described later.

In the AR50/50 specimen, there were not as much changed as ARCu in the Cu yield point. From the Figure 54. The yielding points of Cu were seems to be around 150 MPa. However, when the elastic region of Figure 54 is magnified, the Cu phase was yielded in the lower stress level at around 50 MPa. It is almost identical as the yield point of ARCu specimen.

After yielding of the Cu, the load was transferred to the Fe and the Cu did not take the load until the Fe started yielding. When the load reached the Fe yielding point, the load was taken back to the Cu again. The yield point of Fe in AR50/50 specimen was about 400 MPa. After the yield of Fe, the slope of stress-lattice strain of Fe phase was decreased in a few stress levels, however it immediately, took the load again with Cu phase. That might be presence of third phase, Cu_2O.

The AR50/50 did not exhibit any upper low yielding point phenomenon like ARFe probably due to the increased fcc Cu and Cu_2O phase.

In order to investigate the Cu_2O effects on mechanical response, the single peak strains were investigated. In Figure 55, the iron and copper strains were shown as blue

and red colors respectively, and the strains in the two Cu_2O, (200 and 220) are shown with green color. The overall response of Fe and Cu are almost similar as the Rietveld lattice strain data. The Cu phase had two inflections that can explain the load transfer between bcc Fe phase and the fcc Cu phase. From the single peak strains, we observed that the two Cu_2O peaks (200 and 220) started to take more load with the yielding of Fe around 430 MPa.

In the AR70/30 specimen, the Cu yield point is similar to the AR50/50 specimen. The Cu was yielded at about 50 MPa. However, Fe phase in the AR70/30FeCu was yielded at a higher stress about 450 MPa than ARFe and AR50/50 specimen. It might be due to the Cu solid solution strengthening effects in the Fe matrix. Unlike the AR50/50 specimen, the AR70/30 specimen showed upper and lower yielding phenomenon as shown in Figure 49 due to the increased bcc Fe phase. At the low yielding point region, about 450 MPa, the Fe phase showed similar behavior as ARFe. The lattice strain of Fe was decreased about 0.019 % in the low yielding point region while the ARFe exhibited 0.013 % lattice strain decrease.

Before the yielding Fe, (450 MPa), the lattice strain response was almost similar as AR50/50 specimen. After the Cu yielding, the load was taken by Fe phase. Right after Fe low yielding region, the Cu phase was not still taking the load until the abrupt lattice strain shift. When the Cu took the load abruptly near the 475 MPa, the Fe did not take the load for a while. After the large lattice strain shift in Cu phase, the load were transfer to the Fe phase again.

In Figure 55(b), the elastic and plastic behavior of the Cu_2O in the AR70/30 was exhibited with Fe and Cu phase. Similar to the lattice strain response, the AR70/30

specimen showed similar yielding phenomenon as ARFe specimen. Near the yielding point region, the clear strain reductions were not showed in 200 and 211 reflection. However, 110 showed clear strain reduction similar to the average lattice strain response. In the Cu phase, four grain families (111, 200, 220, and 311) moved randomly. The response of Cu_2O (green line) showed quite a large strain increase compared to the increased strains of Cu and decreased strains of Fe after about 5 % macro-strains.

4.2.4 Ball-milled composites

The densities of the two ball-milled composites, BM70/30 and BM 70/30(LT) were 98.5 % and 98.3%, respectively. The lower density values compared to the other specimens might have originated from the typical oxide layer on the powder surface and higher hardness that hinders consolidation.

In Figure 56, the tensile behavior of the two composites is shown. The BM70/30 specimen did not show high yield stress by grain size strengthening. It is probably due to the severe grain growth during consolidation process. The yield stress, 450 MPa is almost identical to AR70/30 specimen. From the XRD results, Figures 57 and 58, the BM70/30 specimen showed severe grain growth. In the Figure 58, the peak width of BM70/30 was almost identical to as-received powder specimen.

The BM70/30 (LT) specimen fractured at about 550 MPa stress and 0.6% strain. Because the density of the two specimens was almost the same, it did not come from the insufficient densities. It might be due to the lack of atomic-level bonding from the low consolidation temperature, (570 °C) and relatively short sintering time, (30 min), than the HT forging case. However, the XRD peak width of BM70/30 (LT) specimen 110 peak

(blue) was still as broad as the ball-milled powder (red) in Figure 58.

Although the BM70/30 specimen did not show the grain size strengthening effects due to the severe grain growth during the consolidation, there were hardly grain growth in the 570 °C forging temperature. Thus, promising future work for nanocrystalline Fe powder consolidation can be performed based on the temperature with additional processing parameter controls for enhancing ductility such as different dwelling time, pressure, and atmosphere.

5. Summary

- The powder metallurgy processes using ball milling and sinter-forging consolidation have been used to make nanocrystalline Fe alloys which have enhanced strength and hardness compared to the coarse-grained counterparts.
- XRD line broadening analysis based on the Gaussian assumption and TEM observation were performed to measure the grain size of ball-milled Fe powders. After 30 hr ball-milling of Fe powders, the particle sizes were increased from about 10 μm to about 20 μm because of the powder welding effects. However, the grain size decreased from several hundreds nm to 18 nm according to the XRD line broadening analysis and the TEM observation.
- When the ball-milled powders from 0 hr to 100 hr were tested by nanoindentation measurements, the hardness values were increased from 3.5 to 10.5 GPa as the ball-milling time increased from 0 to 100 hours. The hardness values were not changed after 30 hr. Thus, the 30 hr. ball-milling time was considered as optimal condition to produce nanocrystalline Fe powders for the bulk consolidation.
- When the hardness was investigated as a function of the grain sizes, the observed hardness values were increased to 10.5 GPa for 15 nm grain sizes following the Hall-Petch relation.
- Four regular specimens, ARFe, ARCu, AR50/50, and AR70/30 were consolidated using sinter forging process. The consolidation temperature ranges between 1,000 ~ 1,100 ºC to achieve the full density. The four specimens, ARFe, ARCu, AR50/50, and AR70/30, showed elongations to fractures of 21 %, 10%, 15%, and

13%, respectively.

- When the tensile property values of the ARCu specimen are compared to the fully annealed reference specimen, the elastic modulus and the elongation to fracture were severely decreased. The elastic modulus was decreased from 130 GPa to 94 GPa and the elongation was decreased from 45 % to 10 % possibly due to the 3 ~ 8 vol. % Cu_2O which were also found in the AR50/50 and AR70/30 composites as well.
- In the ARFe, upper / lower yielding phenomenon was observed during *in-situ* neutron diffraction tensile measurements. In the low yield point, the decreased lattice strain was observed probably due to the dislocation relaxation from the solute atoms or vacancies. Similar lattice strain decreases were observed in the AR70/30FeCu specimens.
- The two Fe-Cu alloy composites, AR50/50, and AR70/30 showed about 170 % ~ 220 % higher strengths than the strengths estimated by a simple ROM due to the solid-solution strengthening.
- In order to investigate the solid solution strengthening effects, EDX analysis and nanoindentation hardness measurements were performed on AR70/30 specimen. From the EDX results, the solubility of Fe in Cu and Cu in Fe were 7.5 % and 5 %, respectively. When the hardness values were compared to the ARFe and ARCu, the hardness of Fe in AR70/30 was increased about 33% and the hardness of Cu in AR70/30 was increased about 50%.
- In order to investigate the Cu_2O effects on AR50/50 and AR70/30 specimen, the single peak strains were investigated during the *in-situ* neutron diffraction loading

measurements. The response of Cu_2O showed a large strain increase compared to the Cu and Fe phases after about 5 % macro-strains.

- Second, two ball-milled specimens, BM70/30 (1,000 ~ 1,100 ºC consolidation temperature for full density) and BM70/30(LT) (570 °C consolidation temperature for minimizing grain growth) were fabricated. The BM70/30 specimen showed severe grain growth, thus it did not present any grain size strengthening in the tensile behavior. Although the BM70/30(LT) specimen was fractured at the 550 MPa stress and 0.6% strain during the tensile test, there were hardly any grain growth. This is a promising future work on the nanocrystalline Fe.

6. Future work

According to the broader research plan discussed in the first chapter of this thesis, detailed future plans are suggested into three large categories.

- For ball-milled powder synthesis and characterization:

  - In order to reach the full density during the ball-milled powder consolidation, powder agglomeration should be prevented: cryo-ball-milling.

  - Ball milling of both Fe and Cu together or alloying with other materials can be solutions for preventing Cu oxidization and better ductility after consolidation.

  - The synthesis and its characterization of Fe-Cu based ball-milled amorphous powder can be considered as another approach to Fe-Cu alloy composites.

- For regular composites fabrication and characterization:

  - Development of optimum consolidation parameter for Fe-Cu alloy composites should be investigated in terms of density and powder bonding

  - Additional processes for preventing Cu oxidation will be considered powder canning and degassing

  - To investigate the micro structure of sinter forged composites, TEM observations will be performed.

  - The Lüders band deformation of sinter-forged pure Fe will be studied in terms of dislocation activities

- For ball-milled or nanocrystalline composite fabrication and characterization:

  - Heat treatment will be the first trial for low-temperature forged ball-milled specimens to increase ductility.

  - Intermediate forging temperature for preventing grain growths and increasing ductility will be investigated.

References

References

1. S. Seal, S.C. Kurity, P. Georgieva, and A. Agrawal, Manufacturing nanocomposite parts :presents status and future challenges, MRS bulletin/ Jan.(2004)
2. F. Tang, H. Meeks, J.E. Spowart, T. Gnaeupel-Herold, H. Prask, I. E. Anderson, Consolidation effects on tensile properties of an elemental Al matrix composites, Materials science and Engineering A 2004 386 p:194-204
3. G.M. Pharr, Measurement of mechanical properties by ultra-low load indentation, Materials Science and Engineering A 1998 253 p:151-159
4. Culity, B.D., Some problems in X-rays stress measurements, Adv. In X-ray Anal., 1977. 20: p.259-271
5. Noyan, I. C. and Cohen, J.B., Residual stress measurement by diffraction and interpretation, Springer-Verlag (1987)
6. Henry S. Meeks, □, Marc S. Fleming Nanocrystalline Aluminum metal matrix composites and production methods, U.S. patent no. 6630008 B1, Oct. 7, 2003
7. H.H. Tian and M. Atzmon, Comparison of X-ray analysis methods used to determine the grain size and strain in nanocrystalline materials, Philosophical magazine A, 1999, Vol. 79, No. 8, 1769-1786
8. George E. Dieter, Mechanical Metallurgy, Mc Graw Hill p:197-201
9. Y.M. Wang, M.W. Chen, F. H. Zhou, and E. Ma, Nature, 419, 912-915(2002)
10 H. Gleiter, Prog. Mater. Sce. 33 (1989) 223
11. C. Suryanarayana, C.C. Koch, Nanocrystalline materials – Current research and

future directions, Hyperfine Interactions 130: 5-44, 2000

12. H. Gleiter, Nanostructured materials: Basic concepts and microstructure, H.Gleiter,Acta Mater. 48 (2000) 1-29

13. P.G. Sanders, G.E. Fougere, L.J. Thompson, J.A. Eastman, and J.R. Weertman, Improvements in the synthesis and compaction of nanocrystalline materials, Nanostructured Materials, vol. 8, No. 3, pp 243-252, 1997

14. H. Konard, T. Haubold, R. Birringer and H. Hleiter, Nanostruct. Mater. 7 (1996) 605

15. W. Chang, G. Skandan, S. C. Danforth, B.H. kear and H. Hahn, Nanostruct. Mater. 4 (1994) 507

16. U. Erb, Nanostruct. Mater. 6 (1995) 533

17. C. Suryanarayana mechanical alloying and milling (2001) Materials science 46 1 -184

18. G.R. Shaik and W.W. Milligan, Consolidation of nanostructured metal powders by rapid forging: Processing, Modelling and Subsequent mechanical behavior

19. M.L. Sui and K. Lu, Mater. Sci. Eng. A 179-180 (1994) 541

20 B.D. Culity, Elements of X-ray diffraction, Second edition, Addison-Wesley publishing company, Inc.

21. R.W. Siegel, Materials interfaces: Atomic Level structure and properties, eds. D. Wolf and S. Yip (Chapman & Hall, London, UK, 1992) p. 431

22. Z. Horita, D.J. Smith, M. Furukawa, M. Nemoto, R.Z. Valiev and T.G. Langdon, J.Mater. Res. 11 (1996) 1880

23. B.S. Murty, M.K. Datta and S.K. Pabi, structure and thermal stability of nanocrystalline materials, Sadhana Vol. 28, Parts 1&2, Feb./Apr. 2003, pp23-45

24. S.R. Phillpot, D. Wolf and H. Gleiter, J.Appl. Phys. 78 (1995) 847

25. T.R. Mallow, C.C. Koch, Grain growth in nanocrystalline iron prepared by mechanical attrition, Acta mater. Vol. 45, No. 5, pp. 2177-2186

26. C.E. Krill, R.Klein, S. Janes, R. Strauss and H. Gleiter, Acta Metall. 37 (1989)

27. H. Hahn, J. Jogas and R.S. Aveback, J. Mater. Res 5 (1990) 609

28. J.T. Lee, J.H. Hwang, J.J. Mashek, T.O. Mason, A.E. Miller and R.W. Siegel, J. Mater. Res. 10 (1995) 2295

29. R.N. Viswanath, S.Ramasamy, R.Ramamoorthy, P. Jayavel and T. Nagarajan, Nanostruct. Mater. 6 (1995) 993

30 R.H. Yu, X.X. Zhang, J. Tejada, M. Knobel, P. Tiberto and P. Allia, J. Phys. D28 (1995) 1770

31. G. Herzer, Scripta Metall. Mater. 33 (1995) 1741

32. L. Schultz, J. Wecker and E. Hellstern, J. Appl. Phys. 61 (1987) 3583

33. R.D. Shull, R.D. McMichael and J.J. Ritter, Nanostruct. Mater. 2 (1993) 205

34. D.D. Beck and R.W. Siegel, J. Mater. Res. 7 (1992) 2840

35. L. Zaluski, A. Zaluska, P. Tessier, J.O. Strom-Olsen and R. Schultz, Mater. Sci. Forum 225-227 (1996) 853

36. M. L. Trudeau and J.Y. Ying, Nanostruct. Mater. 7 (1996) 245

37. L. Wong, D. Ostrander, U. Erb, G. Palumbo and K.T. Aust in : Nanophases and nanocrystalline structures, eds. R.D. Shull and J. M. Sanchez (TMS, Warrendale, PA, 1993) p. 85

38. T.D. Shen, C.C. Koch, T.Y. Tsui and G.M. Pharr, J. Mater. Res. 10 (1995) 2892

39. A. R. Boccaccini, G. Ondracek, P. Mazilu and D. Windelberg, J. Mech. Behav. Mater., 4 (1993) 119

40 P. Mazilu and G. Ondracek, in K.P. Herman and Z.S. Olesiak (eds.), Thermal effects in fracture of multiphase materials, Springer, Berlin, 1989, p. 255

41. G.E. Fougere, L. Riester, M.Ferber, J.R. Weertman, R.W. Siege, young's Modulus of nanocrystalline Fe measured by nanoindentation materials science and engineering A 204 (1995) 1-6

42. E.O. Hall, Proc. Phys. Soc. London, Sect. B 64, 747 (1951)

43. N.J. Petch, J. Iron steel Inst., london 174, 25 (1953)

44. J. Karch, R. Birringer and H. Gleiter, Nature 330 (1987) 556

45. A. Inoue, N. Nakazato, Y. Kawamura and T. Masumoto, Mater. Sci. & Eng. A 179/180 (1994) 654

46. G.E. Dieter Mechanical metallurgy Mcgraw-Hill Book company p. 452-453 (1988)

47. Ruslan Z. Valiev, Superplastic behavior of nanocrystalline metallic materials, Materials science forum Vols. 243-245 (1997) pp. 207-216

48. L. Lu, M. L. Sui, K. Lu, Superplastic extensibility of nanocrystalline copper at room temperature, Science vol. 287 25 Feb. 2000 pp.1463-1466

49. Setsuo Takake, Kenji Kawasaki, Yuji Kimura, Mechanical properties of ultra fine grained steels journal of mterials processing technology 117 (2001) 359-363

50 S. Cheng, J. A. Spencer, W.W. Milligan Strength and tension/compression asymmetry in nanostructured and ultrafine-grain metals, Acta materialia 51

(2003) 4505-4518

51. T.W. Clyne, P.J. Withers, An introduction to metal matrix composites, Cambridge university press 1993

52. T. Mura, Mocromechanics of defects in Solids, Nijhoff, The haque, 1987

53. P.J. Withers, A.N. Smith, T.W. Clyne and W.M. Stobbs (1989), A photoelastic examination of the Validity of the Eshelby approach to the modeling of MMCs, in fundamental relationships between microstructure and mechanical properties of MMCs, Indianapolis, P.K. Liaw and M.N. Gungor (eds.), TMS, pp. 225-240

54. B.D. Saint-Venant (1855) Memories des Extrangers, Paris

55. J.D. Eshelby (1957) The determination of the elastic field of an ellipsoidal inclusion and related problems, Proc. Roy. Soc., A241 pp. 376-96

56. R.J. Arsenault and N. Shi (1986) Dislocation generation due to differences between coefficients of thermal expansion, Mat. Sci. & Eng., 81, pp. 175-187

57. W.S. Miller and F.J. Humphreys (1990) Strengthening mechanisms in metal matrix composites, in Fundamental relationships between microstructure and mechanical properties of metal-matrix composites, P.K. Liaw and M.N. Cungor (eds.), TMS, Warrendale, pa.,pp.517-541

58. J.L. Hay, G.M. Pharr, Instrumented indentation testing, ASM Handbook vol. 8 p.222-243

59. W.C. Oliver G.M. Pharr, An improved technique for determining hardness and elastic modulus using load and displacement sensing indentation experiments, Journal of Materials Research 7 (6): 1564-1583 Jun

60 A.P. Ternovskii, V.P. Alekhin, M.Kh. Shorshorov, M.M. Khruschov, V.N. Skvortsov, Zavod Lab. 39 (1973) 1242

61. S.I. Bulychev, V.P. Alekhin, M.Kh. Shoroshorov, A.P. Ternovskii, G.D. Shnyrev, Zavod Lab. 41 (1975) 1242

62. D. Jang, M. Atzmon, Grain-size dependence of plastic deformation in nanocrystalline Fe, Journal of applied physics, vol. 93, no. 11, 1 June 2003

63. B. Clausen, T. Lorentzen and T. leffers, Self-consistent modelling of the plastic deformation of FCC Polycrystals and its implications for diffraction measurements of internal stresses, Acta mater. Vol. 46, No. 9, pp. 3087-3098, 1998

64. E.C. Oliver, M.R. Daymond, P.J. Withers, Interphase and intergranular stress generation in carbon steels, Acta Materialia 52 (2004) 1937-1951

65. E. Ma, Alloys created between immiscible elements, Progress in material science 50 (2005) 413-509

66. Childress Jr. Chien Cl. Phys Rev B 1991;43:8089

67. Krack BD, Ozolins V, Asta M, Daruka I. “Devil’s staircases” in bulk-immiscible ultrathin alloy films. Phys Rev Lett 2002; 81:186101

68. Massalski TB, editor. Binary alloy phase diagrams, vol 1-3. materials Park, OH:American society for metals; 1986

69. Chien CL, Liou SH, Kofalt D, Yu W, Egami T, McGuire T. Phys Rev B 1986;33:3247

70. Koch CC. Mater Trans JIM 1995;36:85

71. Jiang JZ, Gente C, Bormann R. Mater Sci Eng A 1998;242:268

72. Schilling PJ, He J-H, Cheng J, Ma E. EXAFS of bcc and fcc metastable structures in ball-milled Cu-Fe. Appl Phys Lett 1996;68:767-9

73. Harris VG, Kemner KM, Das BN, Koon NC, Ehrlich AE, Kirkland JP, et al. Phys Rev B1996;54;6929

74. Xu J, Herr U, Klassen T, Averback RS. J appl Phys 1996;19:3935

75. Sheng HW, Wilde G, Ma E. The competing crystalline and amorphous solid solutions in the Ag-Cu system. Acta Mater 2002;50:475-88

76. Shaik GR, Milligan WW, Consolidation of nanostructured metal powders by rapid forging: Processing, modeling, and subsequent mechanical behavior, Metallurgical and Materials Transactions A – Physical Metallurgy and Materials Science 28 (3A): 895-904 MAR 1997

77. G. Palumbo, S. J. Thorpe and K. T. Aust, Scripta Metall. Mater. 24, 1347 (1990).

78. C. Suryanarayana, D. Mukhopadhyay, S. N. Patankar, and F. H. Froes, J. Mater. Res. 7, 2114 (1992).

79. N. Wang, Z. Wang, K. Aust, and U. Erb, Acta Metall. Mater. 43, 519 (1995).

80. R. O. Scattergood and C. C. Koch, Scripta Metall. Mater. 27, 1195 (1992).

81. J. Lian, B. Baudelet, and A. A. Nazarov, Mater. Sci. Eng. A. 172, 23 (1993).

82. V. G. Gryaznov, M. Yu. Gutkin, A. E. Romanov, and L. I. Trusov, J. Mater. Sci. 38, 4359 (1993).

83. H. Van Swygenhoven and A. Caro, Phys. Rev. B. 58, 11246 (1998).

84. H. Van Swygenhoven, M. Spaczer, and A. Caro, Acta Mater. 47, 3117 (1999).

85. A.C. Larson and R.B. Van Dreele, General Structure Analysis System, MSH805, Los Alamos National Laboratory, Neutron Scattering Center (Copyright, The

Regent of the University of California, 1993). V.M. Belova and V.I. Nikolaev, Sov. Phys. Solid State 14 (1972) 111

86. Mark R Daymond, Christian Hartig, and Heinrich Mecking, Interphase and intergranular stress generation in composites exhibiting plasticity in both phases Acta Materialia 53 (2005) 2805–2813

87. N. Hansen, The effects of grain size and strain on the tensile flow stress of Al at room temperature, Acta metal., 25, (1977) pp. 863-869

Appendices

Appendix A - Tables

Table. 1 Classification of nanocrystalline materials.

Dimensionality	Designation	Typical method(s) of synthesis
One-dimensional (1D)	Layered (lamellar)	Vapor deposition Electrodeposition
Two-dimensional (2D)	Filamentary	Chemical vapor deposition
Three-dimensional (3D)	Crystallites (equiaxed)	Gas condensation Mechanical alloying/milling

C. Suryanarayana, C.C. Koch, Nanocrystalline materials – Current research and future directions, Hyperfine Interactions 130: 5-44, 2000

Table. 2 Methods for the synthesis of nanocrystalline materials.

Starting phase	Technique	Dimensionality of product
Vapor	Inert gas condensation	3D
	Physical vapor deposition – Evaporation and sputtering	1D
	Plasma processing	3D
	Chemical vapor condensation	3D, 2D
	Chemical reactions	3D
Liquid	Rapid solidification	3D
	Electrodeposition	1D, 3D
	Chemical reactions	3D
Solid	Mechanical alloying/milling	3D
	Devitrification of amorphous phases	3D
	Spark erosion	3D
	Sliding wear	3D

C. Suryanarayana, C.C. Koch, Nanocrystalline materials – Current research and future directions, Hyperfine Interactions 130: 5-44, 2000

Table. 3 Typical capacities of various types of mills

Mill type	Sample weight
Mixer mills	Up to 2 × 20 g
Planetary mills	Up to 4 × 250 g
Attritors	0.5–100 kg
Uni-ball mill	Up to 4 × 2000 g

C. Suryanarayana, C.C. Koch, Nanocrystalline materials – Current research and future directions, Hyperfine Interactions 130: 5-44, 2000

Table. 4 Changes in grain size of nanocomposites processed using various consolidation techniques

		Grain Size (nm)		
Techniques	Materials[a]	Initial	Final	Reference
Hot isostatic pressing	Ti-48Al	15	150	22
	Ti-55Al	10	220	23
	Ti-24Al-11Nb	5	1000	23
	Fe-10wt%Cu	18	350	24
Sinter forging	ZrO_2	10	45	25
	Fe-29Al-2Cr	15	100	26
	Fe-10Cu	20	50	27
Hot pressing	Al_2O_3-12vol%SiC	50	300	28
	Al-33.3Fe-33.3Ti	5	30	29
Transformation-assisted consolidation	TiO_2 (anatase)	50	185	30
	TiO_2 (anatase)	15	20	31
Spark plasma sintering	γ-Al_2O_3-10vol%TiO_2	15	1000	36
	Fe-Fe_3C	8	45	37
	WC-10Co	100	300	38
Severe plastic torsional straining	Cu-5vol%SiO_2	50	10	42
	Al-5vol%SiO_2	50	25	42
Microwave sintering	TiO_2	30	300	47
Dynamic consolidation using shock waves	$TiSi_2$ and Ti_5Si_2	5	40	49
	Ti-55Al	10	15	23
	Ti-24Al-11Nb	5	25	23
	Fe-28Al-2Cr	7	80	51
Plasma forming	W-HfC, Cr_3C_2, Al_2O_3-TiO_2, ZrO_2, micro-nano Al_2O_3, Ni-Al_2O_3, Al-Al_2O_3 and hypereutectic Al-Si, Al-Si/Al_2O_3 bulk parts	Micro-nano	20–100	61–69

[a]Unless stated otherwise, all compositions are in at.%.

S.Seal, S.C.Kurity, P.Georgieva, and A.Agarwal, Manufacturing Nanocomposite Parts:Present Status and Future Challenges, MRS Bulletin/January(2004)

Table. 5 Pressure parameters used during sinter forging of nc Fe

Consolidation at 575 □			
Maximum Pressure(MPa)	Loading Rate (MPa/s)	Hold Time at Maximum pressure(s)	Relative Density
70	35	0	0.831
123	35	0	0.916
245	35	0	0.935
350	35	0	0.970
525	35	0	0.997
525	525	0	0.975
525	525	4	0.986
525	525	14	0.995

G.R.Shaik and W.W.Milligan, Consolidation of Nanostructured Metal Powders by Rapid Forging:Processing, Modeling, and Subsequent Mechanical Behavior.

Table. 6 List of all powder and bulk specimens

Specimen ID	Condition	Composition (in vol.%)	Form	Consolidation Temperature [°C]
ARFe(P)	as-received	100	powder	-
ARCu(P)	as-received	100	powder	-
BMFe(P)	ball-milled	100	powder	-
ARFe	as-received	100	consolidated	1000~1100
ARCu	as-received	100	consolidated	1000~1100
AR70/30	as-received Fe as-received Cu	70 30	consolidated	1000~1100
AR50/50	as-received Fe as-received Cu	50 50	consolidated	1000~1100
AR70/30 (LT)	as-received Fe as-received Cu	70 30	consolidated	570
BM70/30	Ball-milled Fe as-received Cu	70 30	consolidated	1000~1100
BM70/30 (LT)	Ball-milled Fe as-received Cu	70 30	consolidated	570

Table. 7 Tensile properties of two monloithic specimens

		Y.S. [MPa]	U.T.S. [MPa]	El. [%]	Elastic Moculus [GPa]	C.T.E. [10-6·□-1]
Pure Fe	Book Value (Fully annealed)	130	262	25	211	11.8
	Exp. Value	**350**	**363**	**21**	**197**	-
Pure Cu	Book Value (Fully annealed)	69	200	45	130	17.0
	Exp. Value	**50**	**194**	**10**	**94**	-

Table. 8 Tensile properties of high temperature forged specimens

	ARFe	ARCu	AR70/30FeCu	BM70/30FeCu
Y.S [MPa]	271	60	464	436
El. To Failure [%]	18	26	17	10

Appendix B - Figures

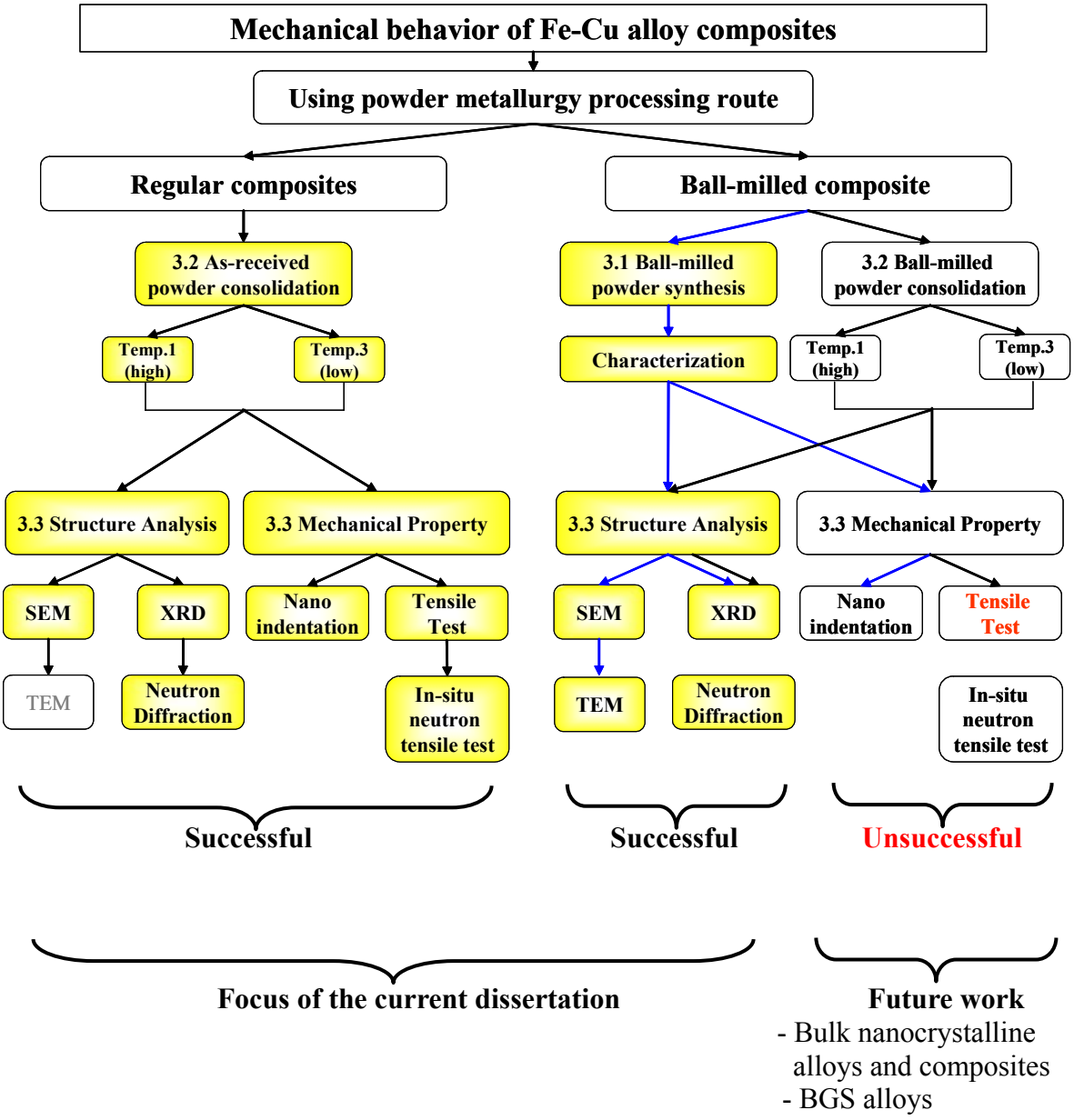

Fig. 1 A flow chart of detailed research plan

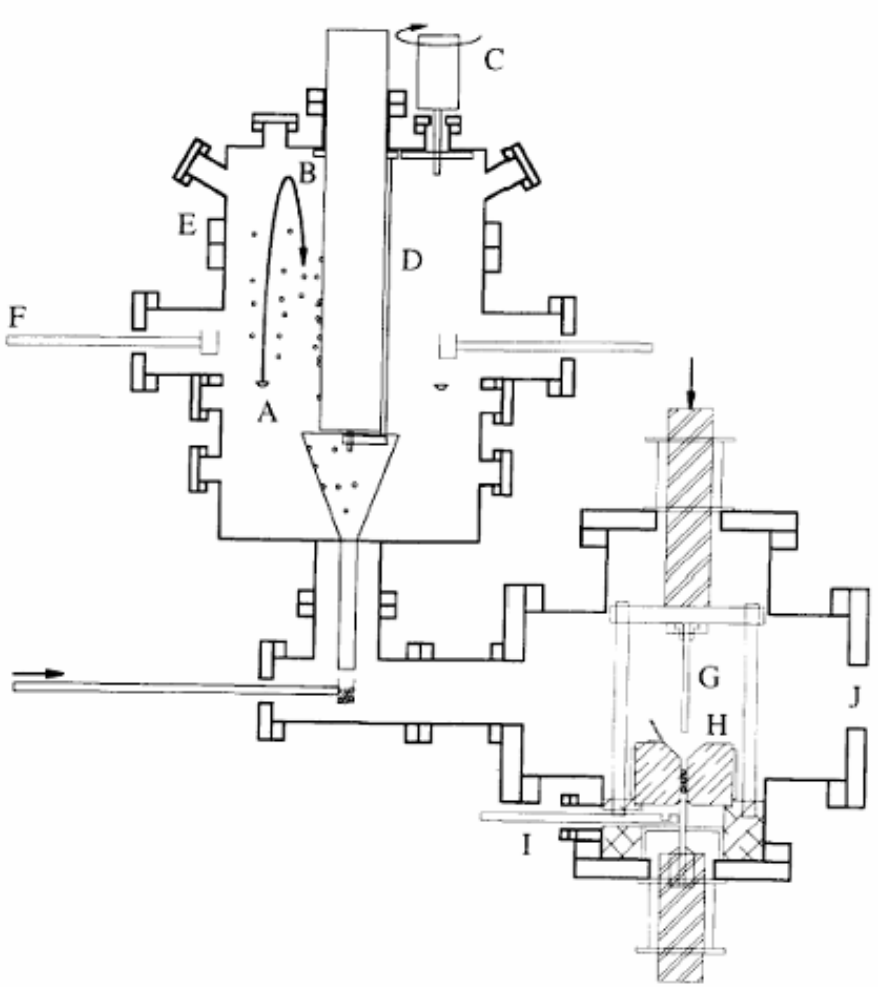

Fig. 2 Cross-section of new synthesis chamber (NSC) and new compaction unit(NCU). The labels refer to the following: (A)resistively-heated evaporation source, (B)cold finger collector, (C)scraper driver, (D)scraper(only 1 of 3 vanes shown), (E)large, viton-sealed flange, (F)boat reloader, (G)upper(moving)piston, (H)die(with heating capability), (I)sample remover, and (J)port to electron beam n-powder preparation system. P.G.Sanders, G.E.Fougere, L.J.Thompson, J.A.Eastman, and J.R.Weertman, Improvements In the Synthesis and Compaction of Nanocrystalline Materials, Nanostructured Materials, Vol.8, No.3, pp 243-252, 1997

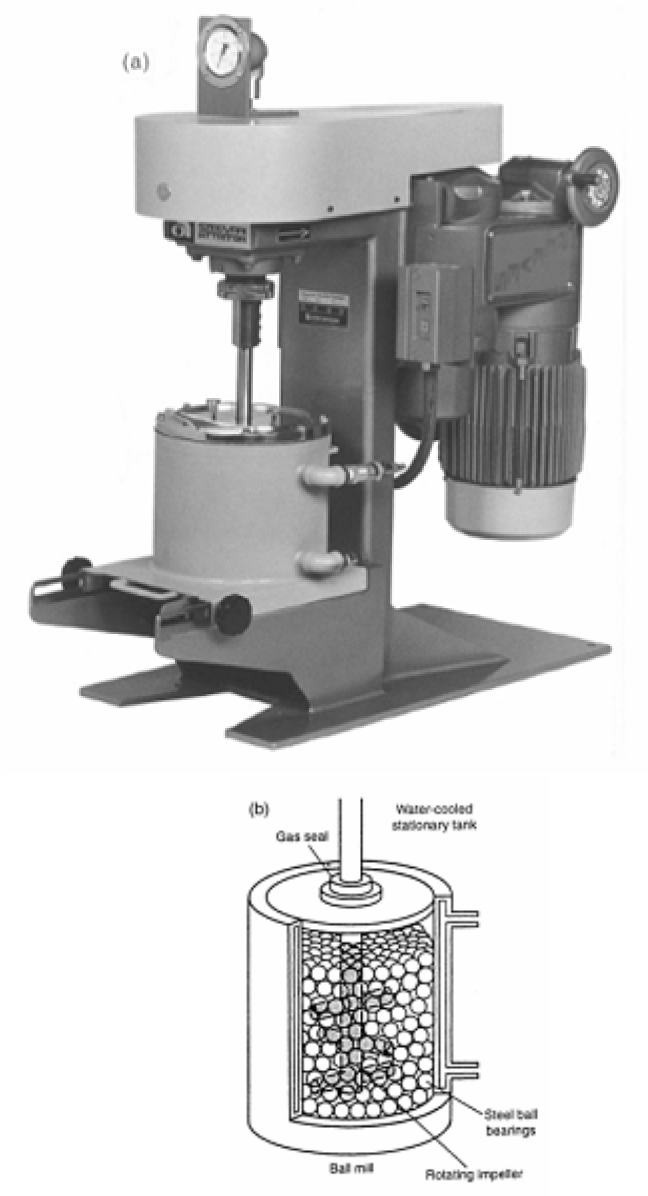

Fig.3 An example of the attritor mill. (a) Model 1-S attritor mill (b) Arrangement of rotating arms on a shaft in the attrition ball mill. Courtesy of Union Process, Akron, OH.
C.Suryanarayana Mechanical alloying and milling(2001) Matereals science 461-184

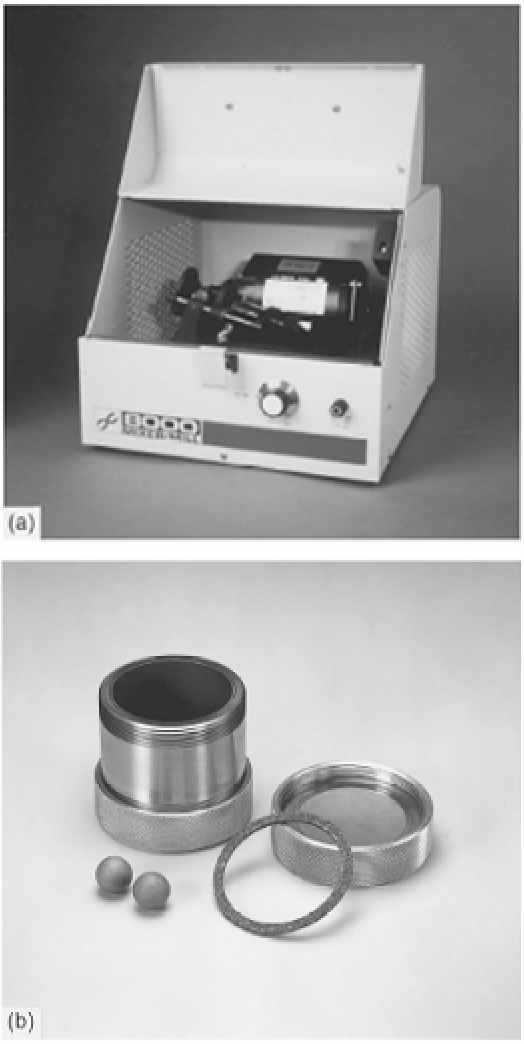

Fig. 4 SPEX 8000 mixer/mill. (a) SPEX 8000 mixer/mill in the assembled condition. (b) Tungsten carbide vial set consisting of the vial, lid, gasket, and balls. Courtesy of SPEX CertiPrep, Metuchen, NJ.
C.Suryanarayana Mechanical alloying and milling(2001) Matereals science 461-184

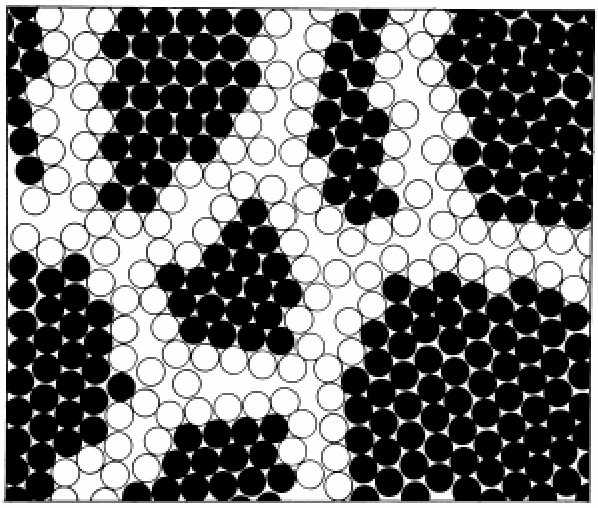

Fig. 5 Two-dimensional model of a nanostructured material. The atoms in the center of the crystals are indicated in black. The ones in the boundary regions are represented as open circles
H. Gleiter, Prog. Mater. Sci., 1998, 33, 223.

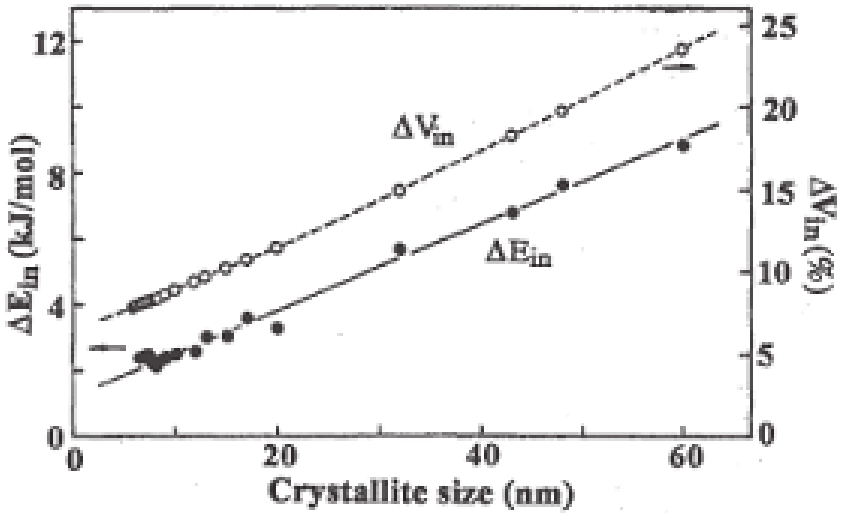

Fig. 6 Variation of the interfacial excess energy changes in the ΔE and ΔV with the average grain size in the nanocrystalline Ni-P alloy (Lu et al 1993; Lu 1996).
B. S. MURTY, M. K. DATTA and S. K. PABI, Structure and thermal stability of nanocrystalline materials, Sadhana Vol. 28, Parts 1&2, February/April 2003, pp23-45

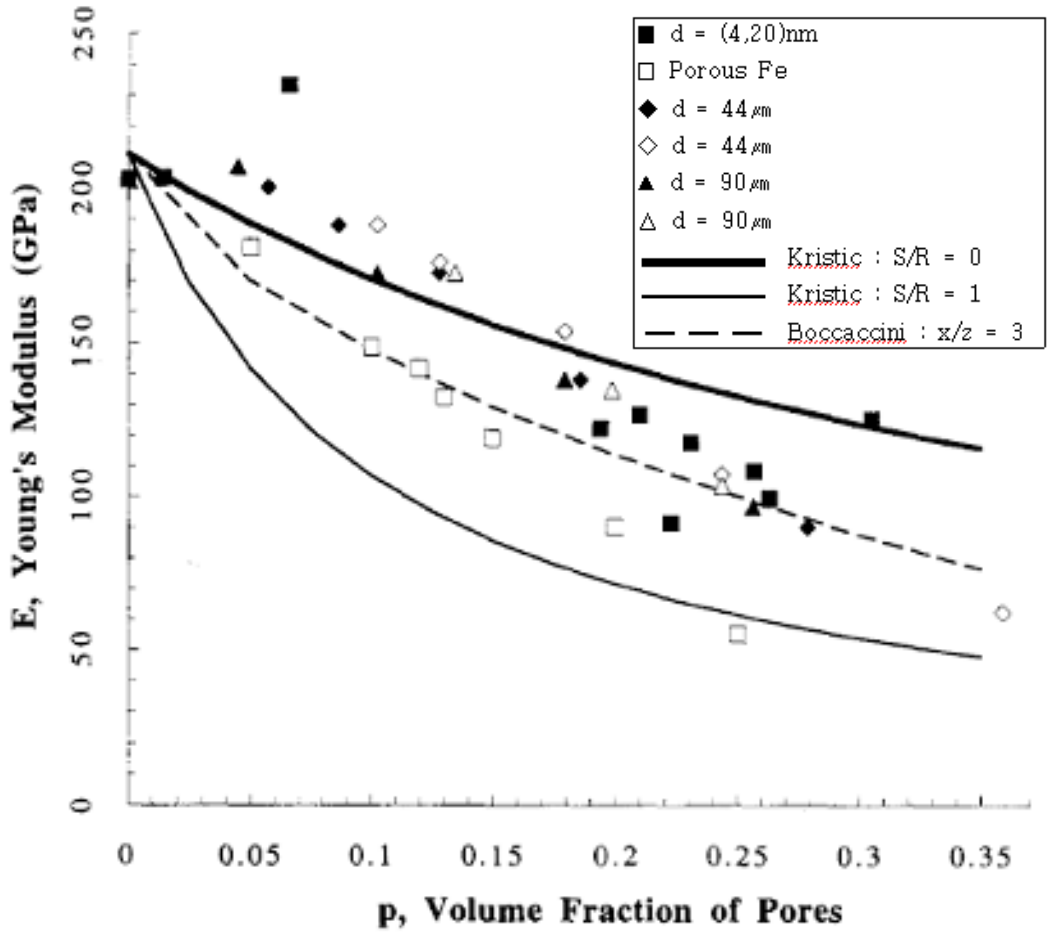

Fig. 7 Young's modulus of porous nanocrystalline Fe and conventional Fe samples plotted against the volume fraction of pores.
G. E. Fougere, L. Riester, M. Ferber, J. R. Weertman, R. W. Siege, Young's Modulus of nanocrystalline Fe Measured by Nanoindentation Materials Science and Engineering A204(1995) 1-6

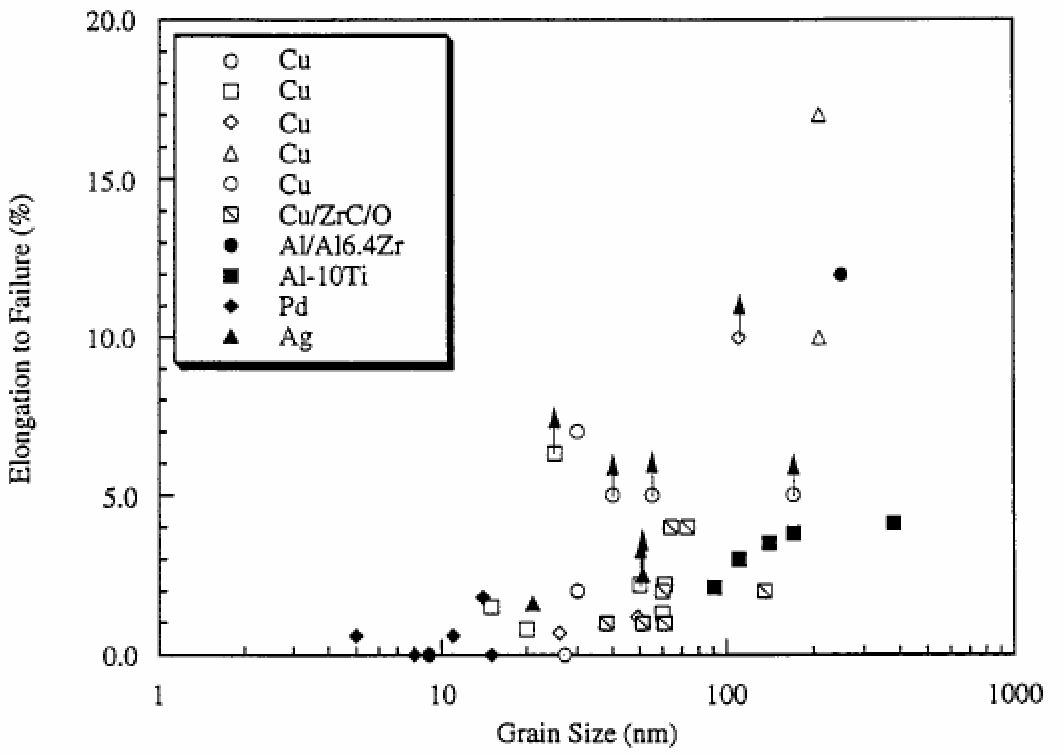

Fig. 8 Elongation to failure in tension vs. grain size for some nanocrystalline metals and alloys.
C. Suryanarayana, C. C. Koch, Nanocrystalline materials – Current research and future directions, Hyperfine Interactions 130: 5-44, 2000

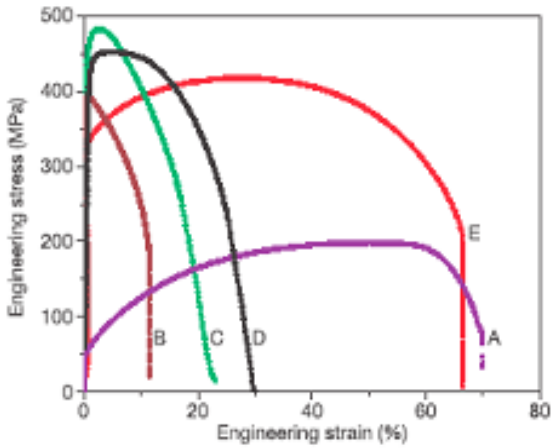

Fig. 9 Engineering stress-strain curves for pure Cu. Curve A, annealed, coarse-grained Cu; B, room temperature rolling to 95% cold work (CW); C, liquid-nitrogen temperature rolling to 93% CW; D, 93% CW . 180 ºC, 3 min.; and E, 93% CW. 200 ºC, 3 min. Note the coexisting high strength and large uniform plastic strain as well as large overall percentage elongation to failure for curve E

Y. Wang, M. Chen, F. Zhou & E. Ma, High tensile ductility in a nanostructured metal Nature vol419 31 October 2002

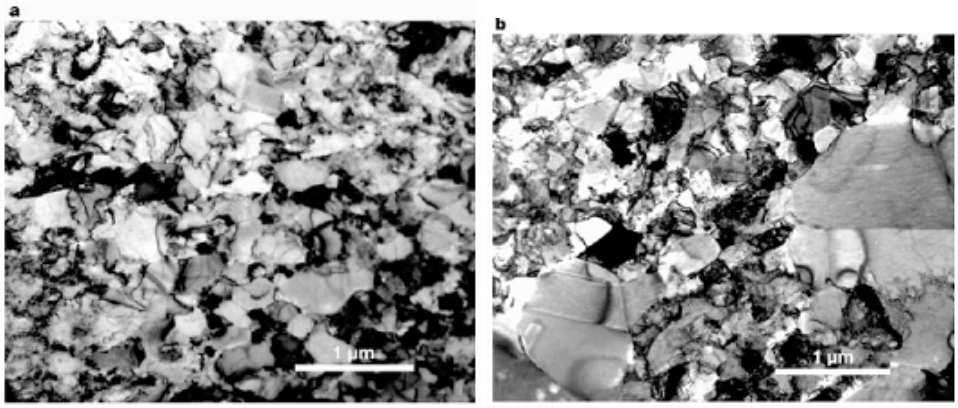

Fig. 10 Transmission electron micrographs showing the evolution of the Cu microstructure. Panels a and b show the samples used to obtain the curves D and E in the previous fig. a. respectively. After annealing at 180 ºC for 3 min (a), recovery has occurred, and the dislocation density is much reduced. The vast majority of the grains are in the nanocrystalline/ultrafine range, with some recrystallized regions. Heat-treating at 200 ºC for 3 min led to full recrystallization followed by secondary recrystallization (b).

Y. Wang, M. Chen, F. Zhou & E. Ma, High tensile ductility in a Nanostructured metal Nature vol419 31 October 2002

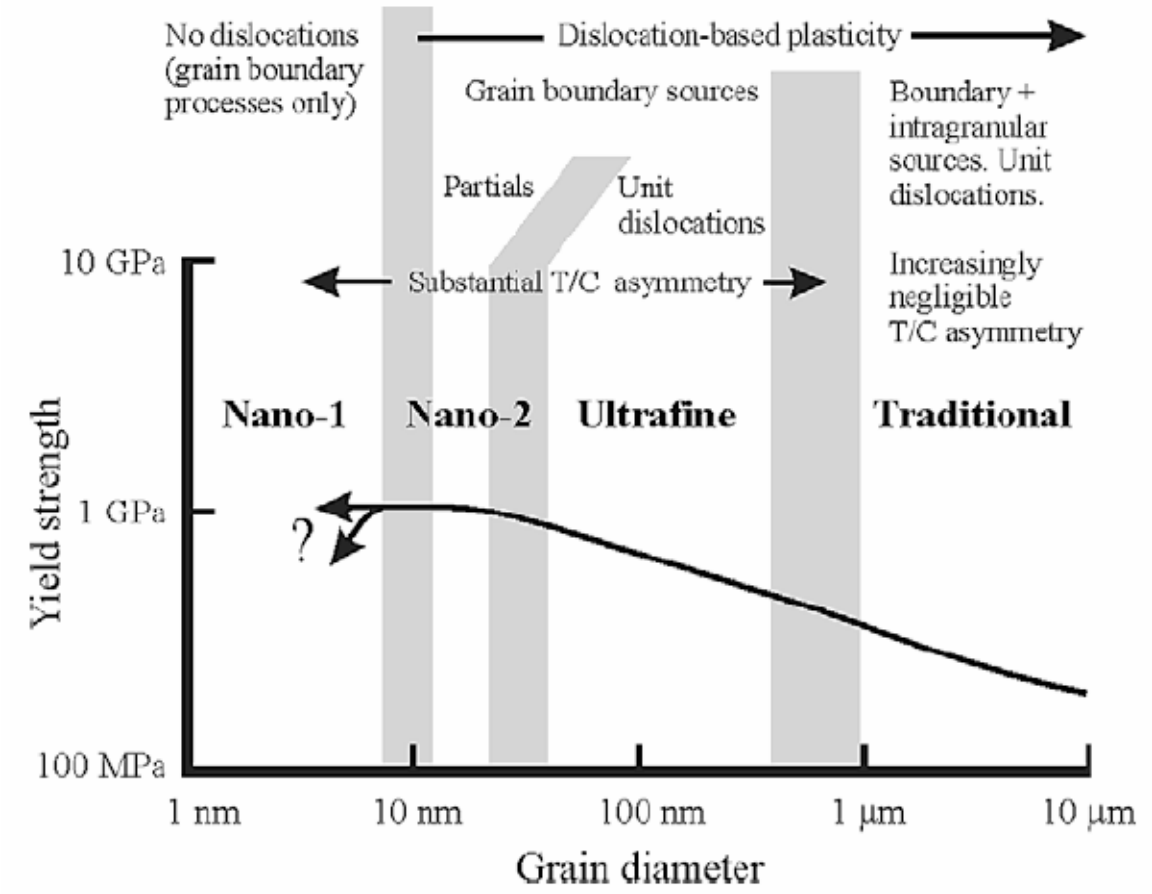

Fig. 11 Deformation mechanism map for FCC metals. Strength curve is based on cop per, which is presented for example purposes.
S. Cheng, J. A. Spencer, W. W. Milligan, Strength and tension/compression asymmetry innanostructured and ultrafine-grain metals Acta Materialia 51 (2003) 4505–4518

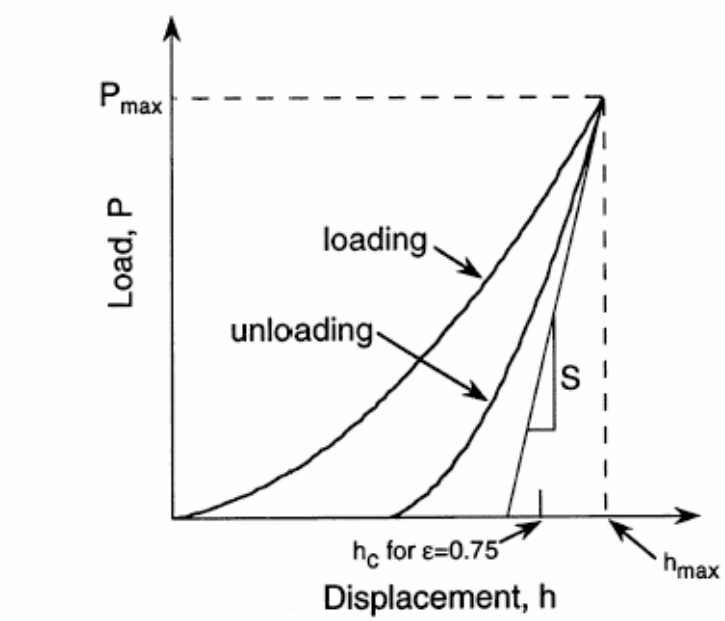

Fig. 12 Typical indentation load-displacement data defining key experimental quantities.
W. C. Oliver, G. M. Pharr, An improved technique for determining hardness and elastic modulus using load and displacement sensing indentation experiments, Journal of Materials Research 7 (6):1564-1583 Jun 1992

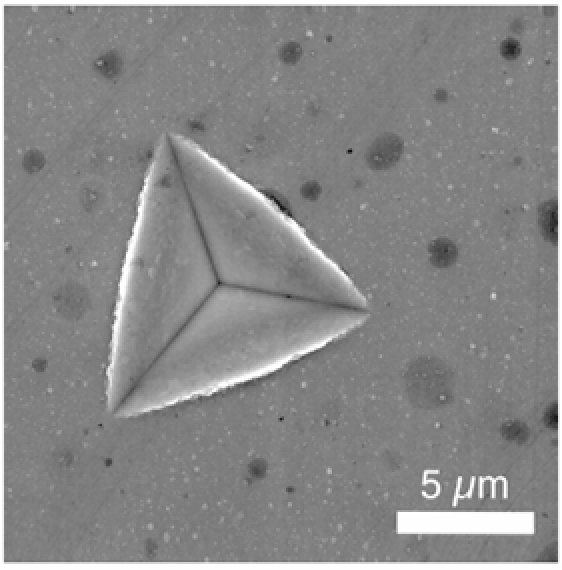

Fig. 13 Scanning electron micrograph of a small nanoindentation made with a Berkovich indenter in a 500 nm aluminum film deposited on glass.
W. C. Oliver, G. M. Pharr, An improved technique for determining hardness and elastic modulus using load and displacement sensing indentation experiments, Journal of Materials Research 7 (6):1564-1583 Jun 1992

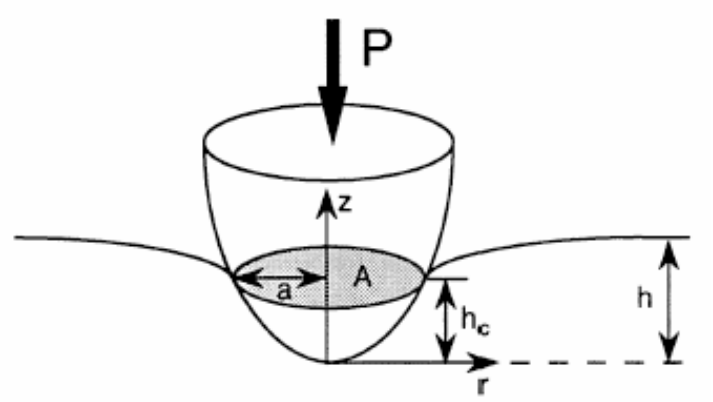

Fig. 14 The physical processes involved in indentation.
W. C. Oliver, G. M. Pharr, An improved technique for determining hardness and elastic modulus using load and displacement sensing indentation experiments, Journal of Materials Research 7 (6):1564-1583 Jun 1992

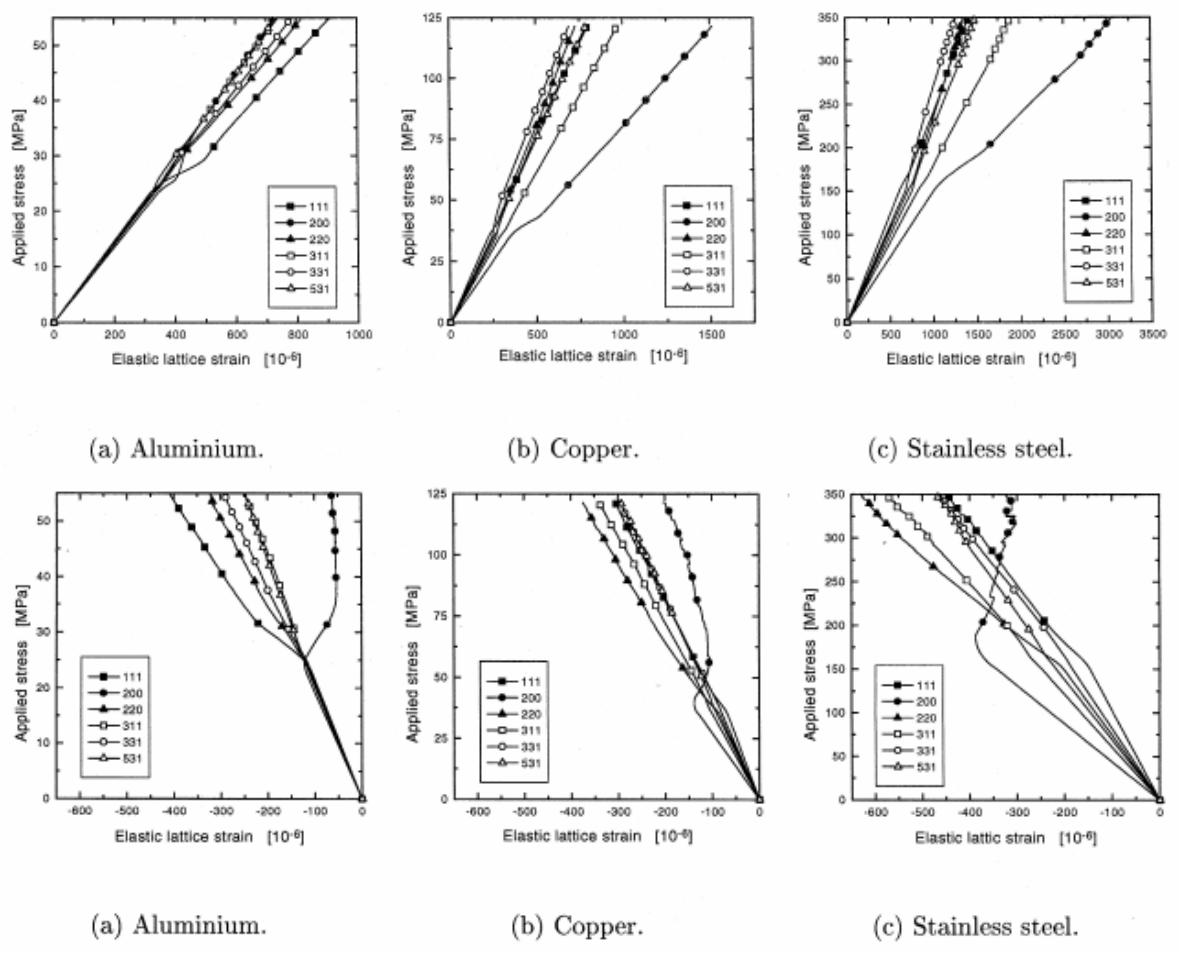

Fig. 15 Stress-strain response parallel and perpendicluar to the tensile axis, givenfor six reflections. (a)-(c) axial; (d)-(f) transverse direction
B. Clausen, T. Lorentzen and T. Leffers, Self-consistent modelling of the plastic deformation of FCC polycrystals and its implications for diffraction measurements of internal stresses, Acta mater. Vol. 46, No.9, pp. 3087-3098, 1998

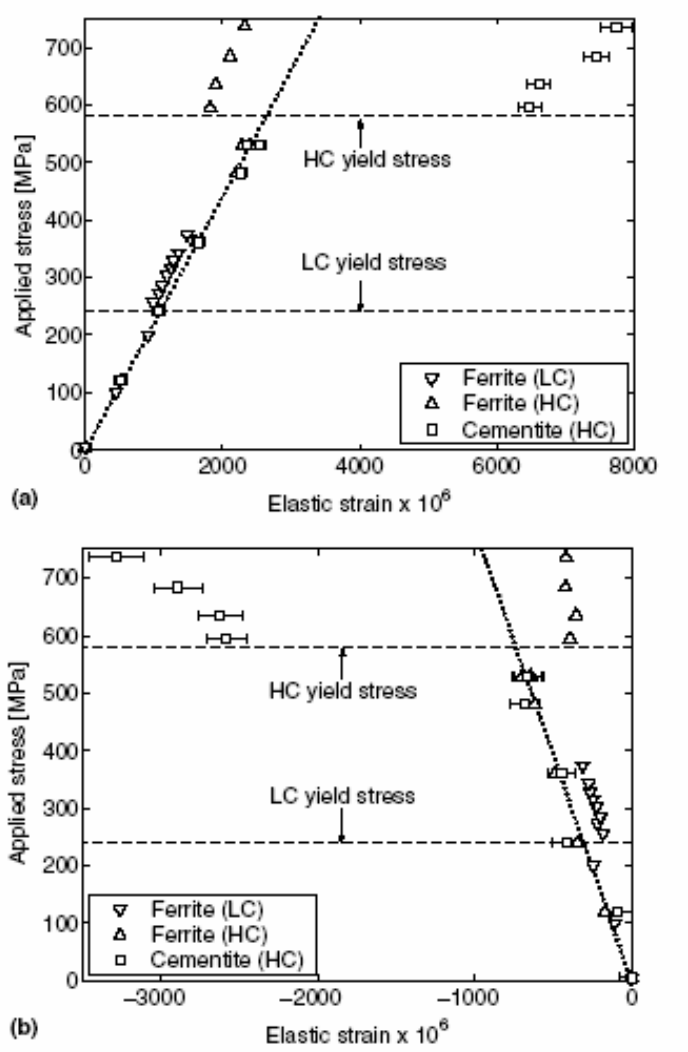

Fig. 16 Lattice strains determined by Rietveld refinement as a function of applied uniaxial tensile stress: (a) axial; (b) transverse strain. The dotted lines passing through the origin are best fits to the initial linear elastic response of the ferrite phase in HC steel. Statistical fitting uncertainties are shown for cementite but are too small to represent for the ferrite phase.
E. C. Oliver, M. R. Daymond, P. J. Withers, Interphase and intergranular stress generation in carbon steels, Acta Materialia 52 (2004) 1937-1951

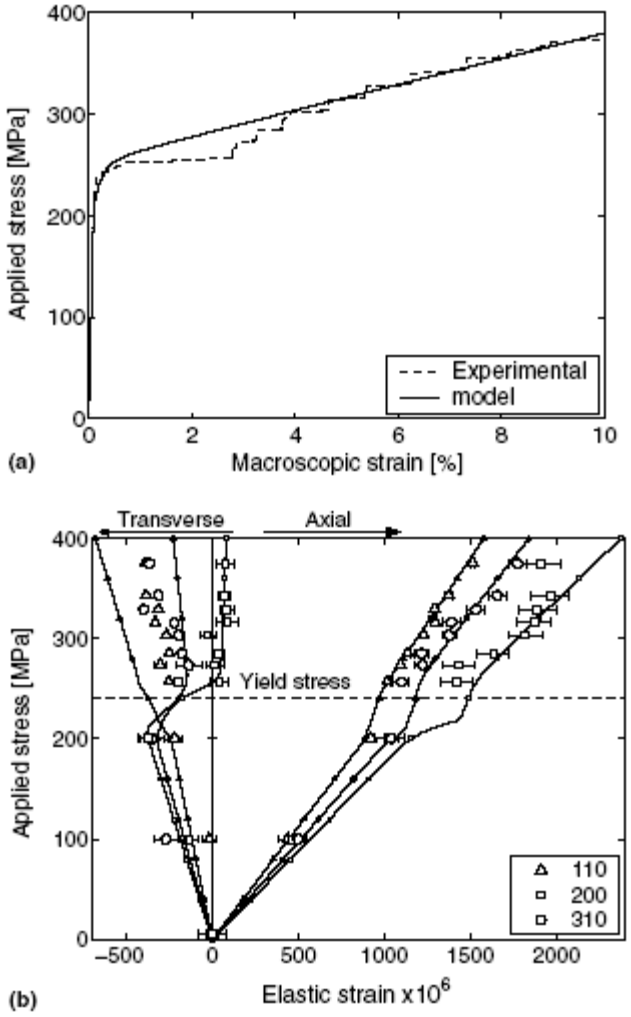

Fig. 17 Comparison of EPSC simulation of LC steel to experimental data: (a) modeled and experimental macroscopic stress–strain curves;(b) modeled and experimental evolution of average grain family elastic strains, against applied stress. In (b), experimental measurements are represented by large datapoints, model calculations by continuous lines joined by small datapoints. E. C. Oliver, M. R. Daymond, P. J. Withers, Interphase and intergranular stress generation in carbon steels, Acta Materialia 52 (2004) 1937-1951

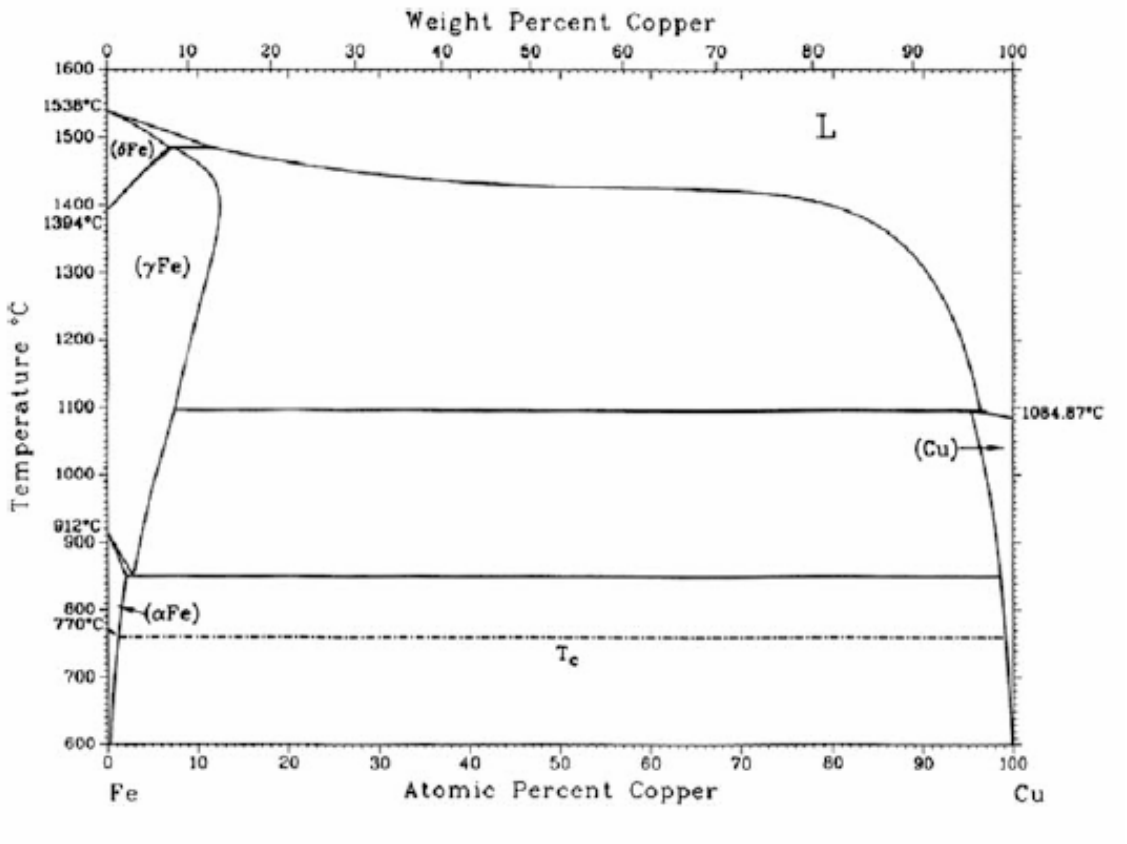

Fig. 18 The equilibrium Fe–Cu phase diagram.
T. B.Massalski editor, Binary alloy phase diagrams, vol 1–3. Materials Park, OH: American Society for Metals; 1986.

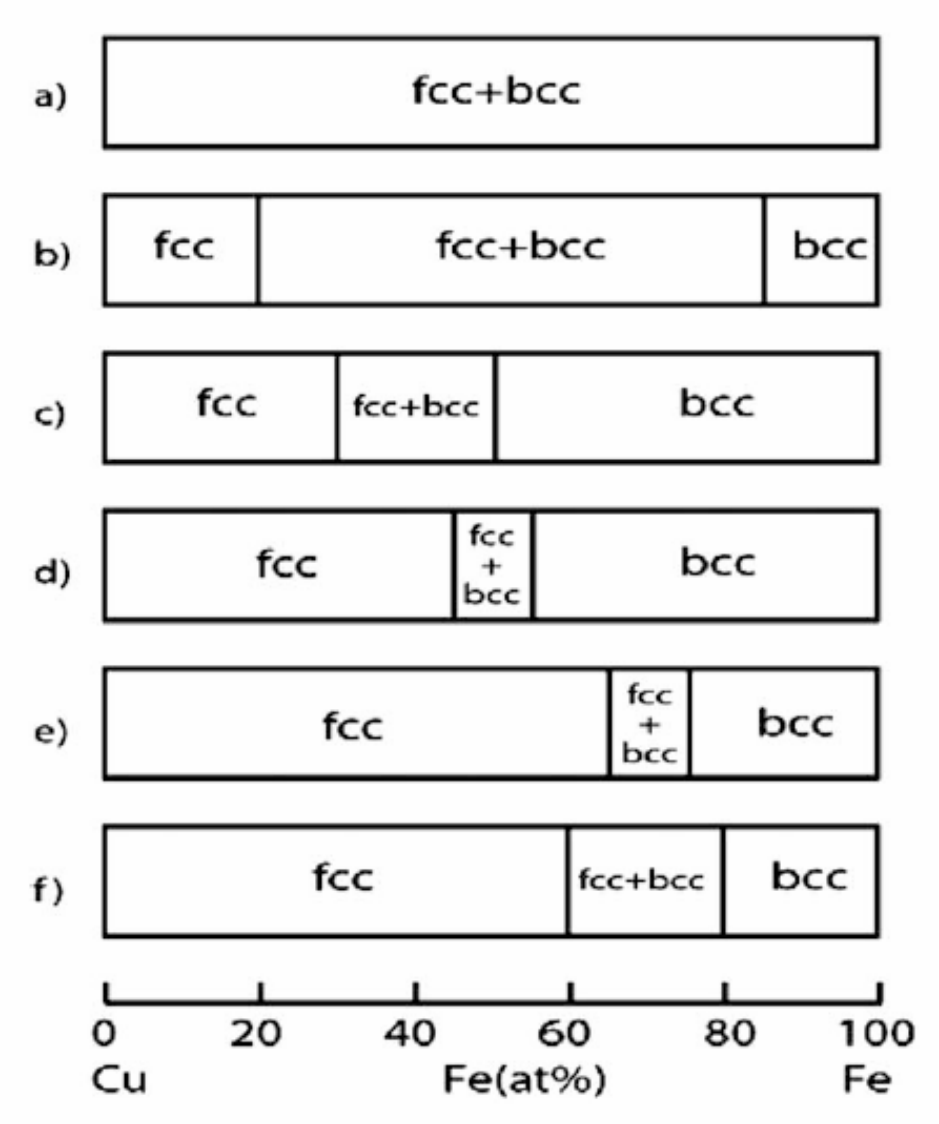

Fig. 19 Schematic diagram of Fe-Cu alloying formation. (a) the equilibrium phase boundary at room temperature. Included for comparison is the phase boundaries obtained by (b) liquid quenching, (c) thermal evaporation, (d) sputtering, (e) sputtering on cryogenic substrates, and (f) mechanical alloying. E. Ma, Alloys created between immiscible elements, Progress in material science 50 2005

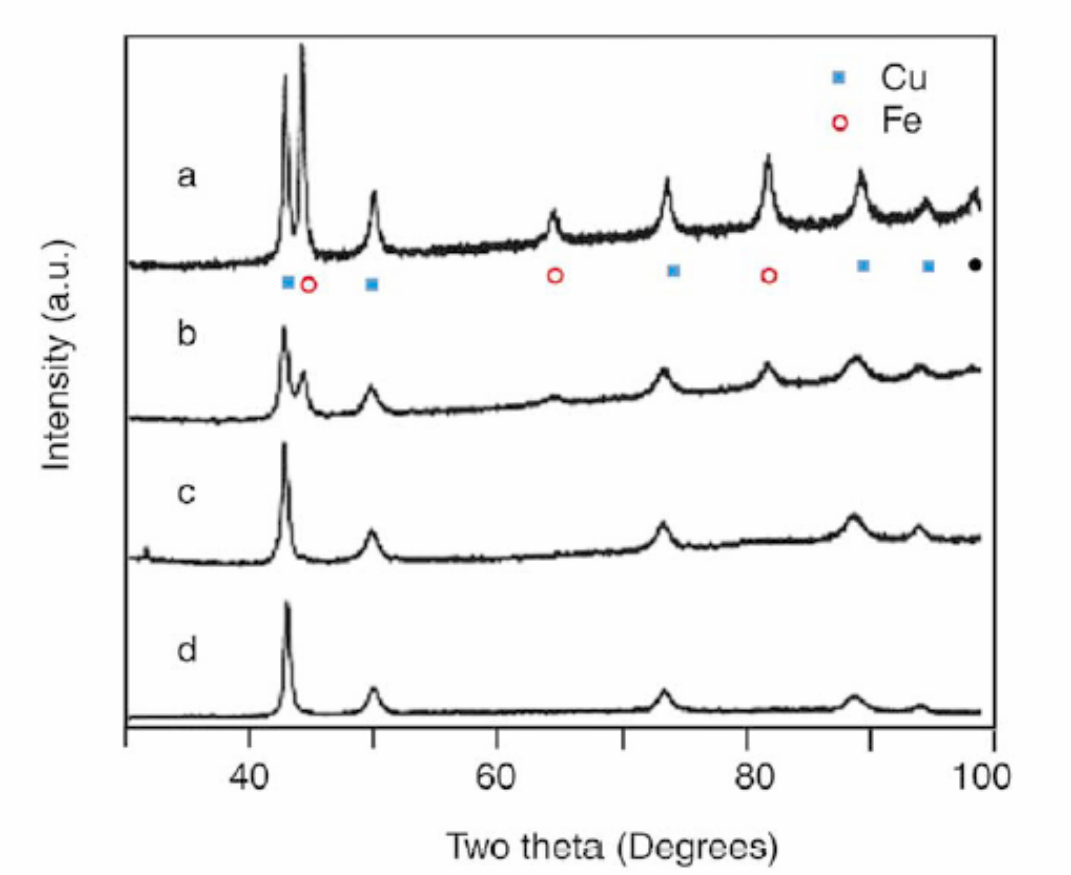

Fig. 20 Typical X-ray diffraction patterns for Fe50Cu50 powder samples after different ball-milling times: (a) 10 h, (b) 30 h, (c) 50 h, and (d) 100 h.
J. Z. Jiang, C. Gente, R. Bormann, Mater Sci Eng A 1998;242:268

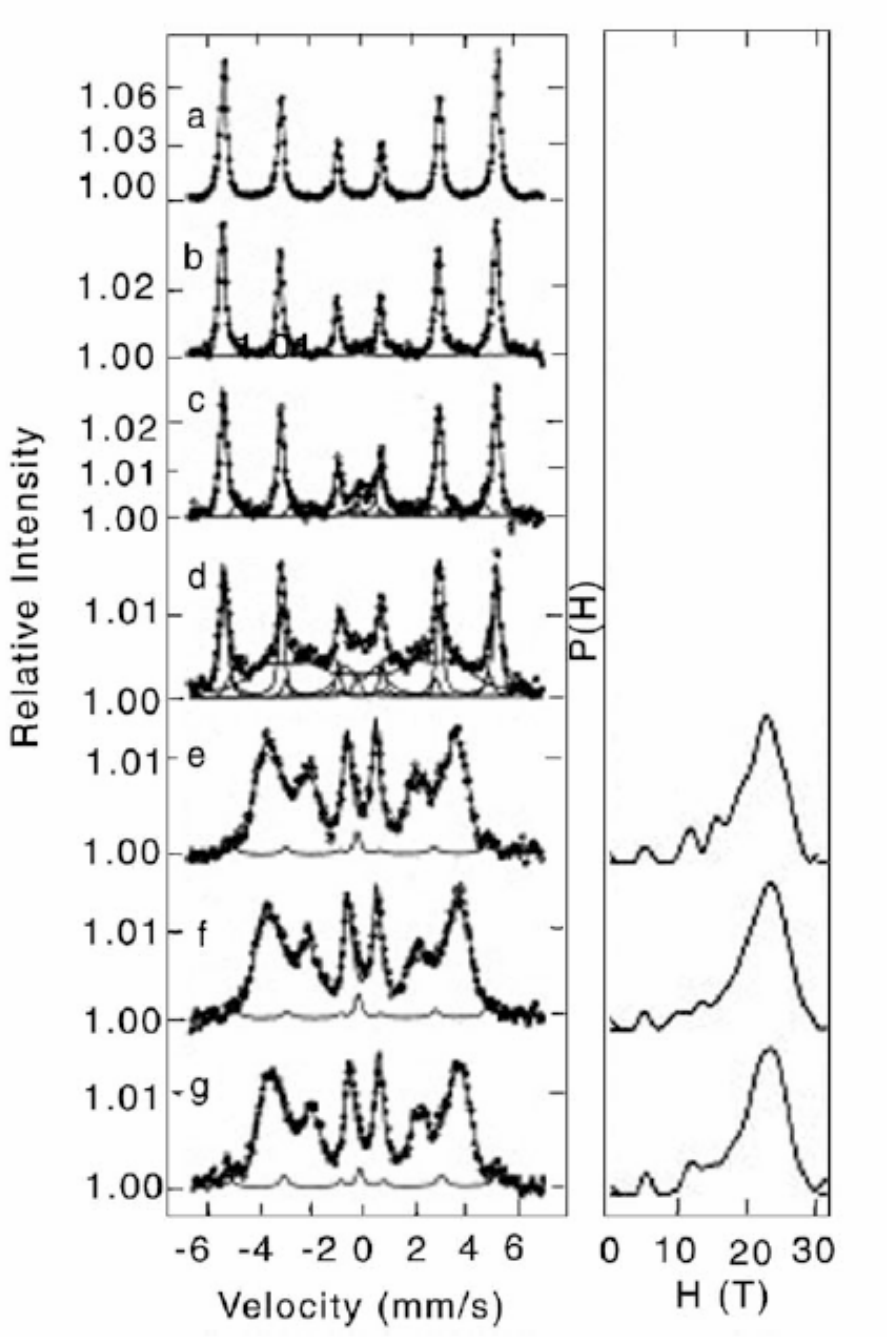

Fig. 21 Room-temperature CXMS spectra and the corresponding hyperfine field distributions for Fe50Cu50 samples after different milling times. (a) 0.5 h, (b) 10 h, (c) 20 h, (d) 30 h, (e) 50 h, (f) 75 h, and (g) 100 h.
J. Z. Jiang, C. Gente, R. Bormann, Mater Sci Eng A 1998; 242:268.

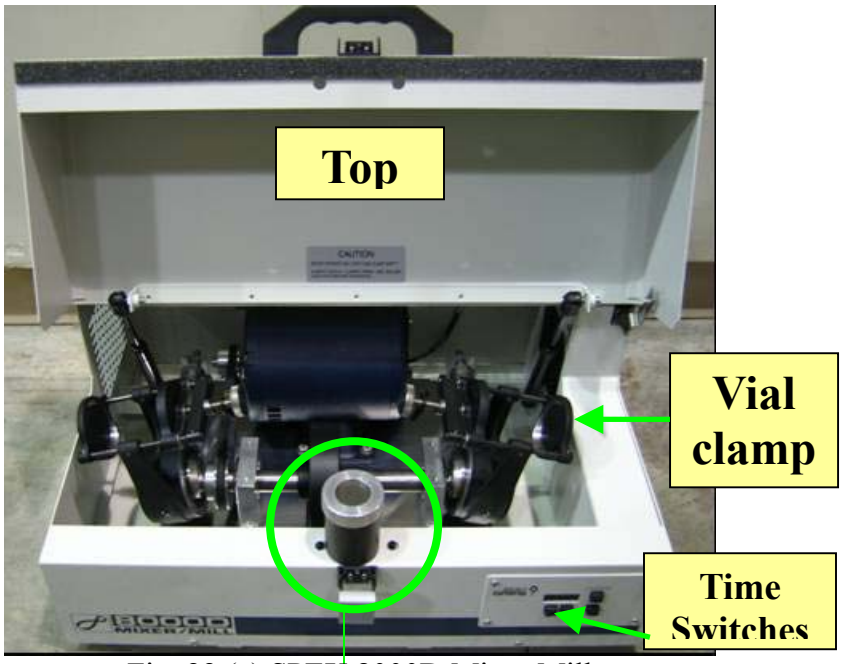

Fig. 22 (a) SPEX 8000D Mixer Mill

Fig. 22 (b) Stainless steel vial and stainless steel grinding balls

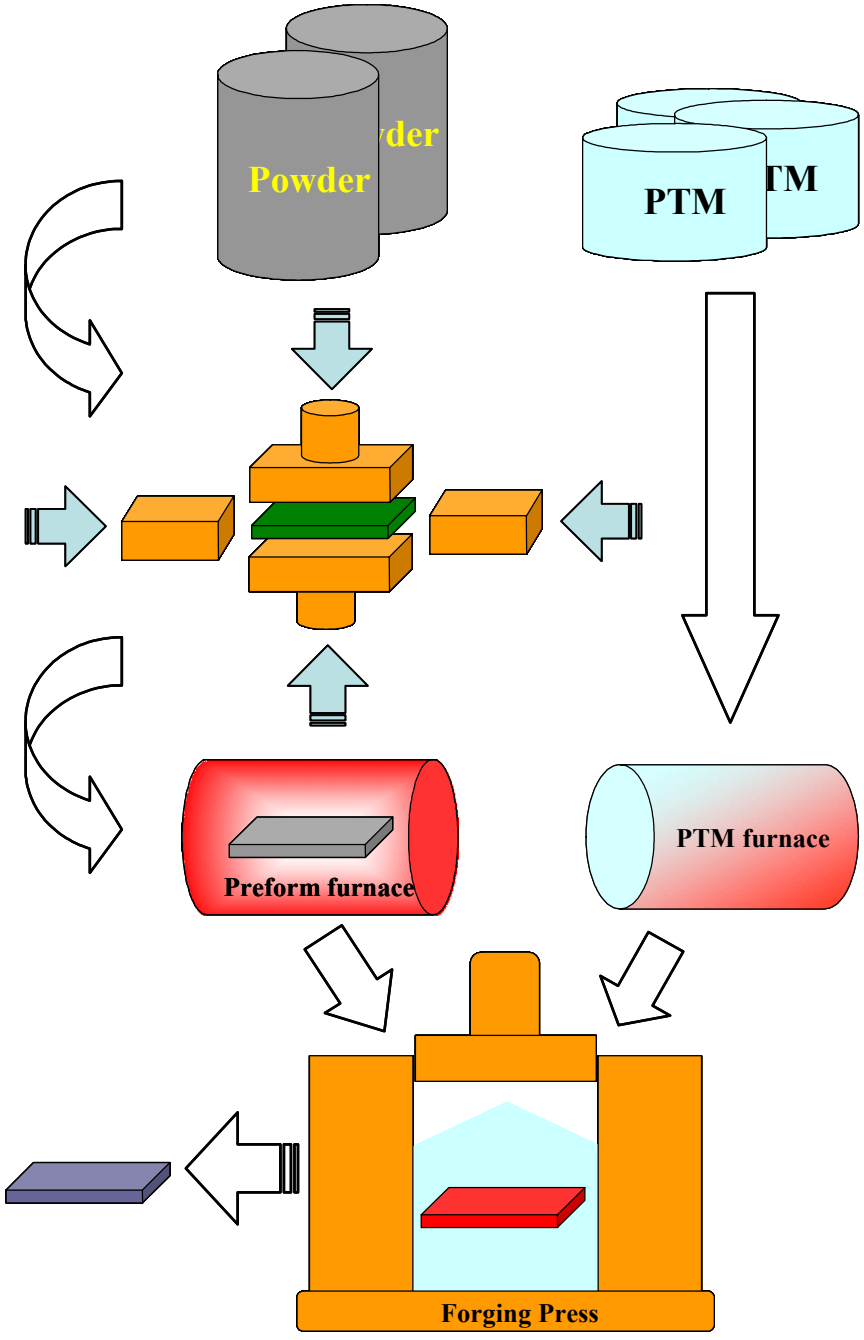

Fig. 23 Schematic of Ceracon sinter-forging process

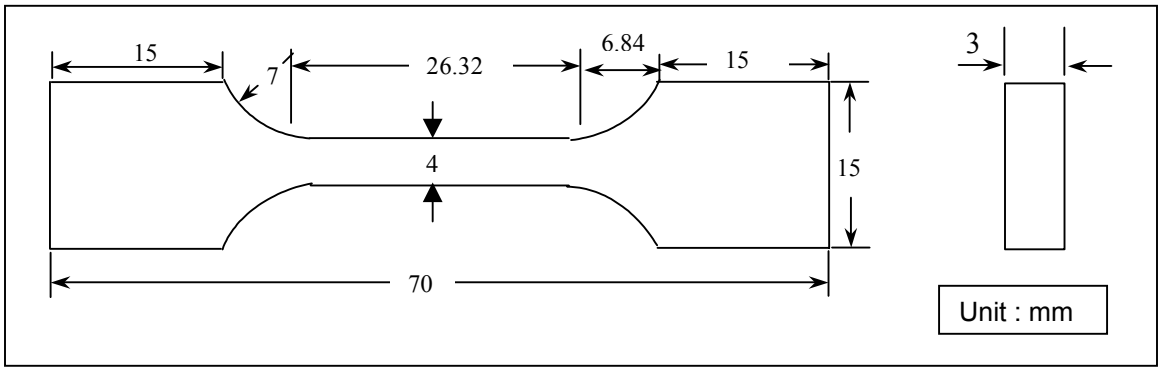

Fig. 24 Flat tensile sample

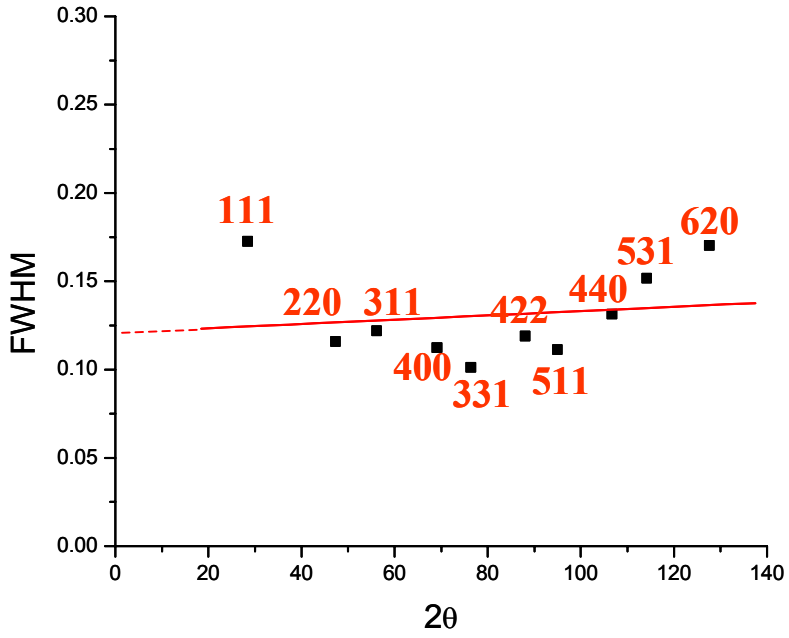

Fig. 25 (a) FWHM vs. diffraction angle of Si640b standard

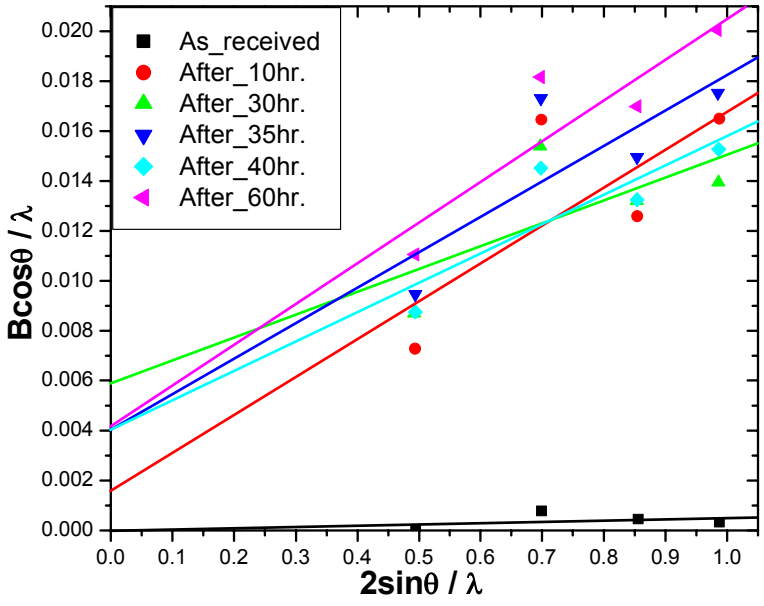

Fig. 25 (b) Williamson-Hall plot to remove strain effects on FWHM

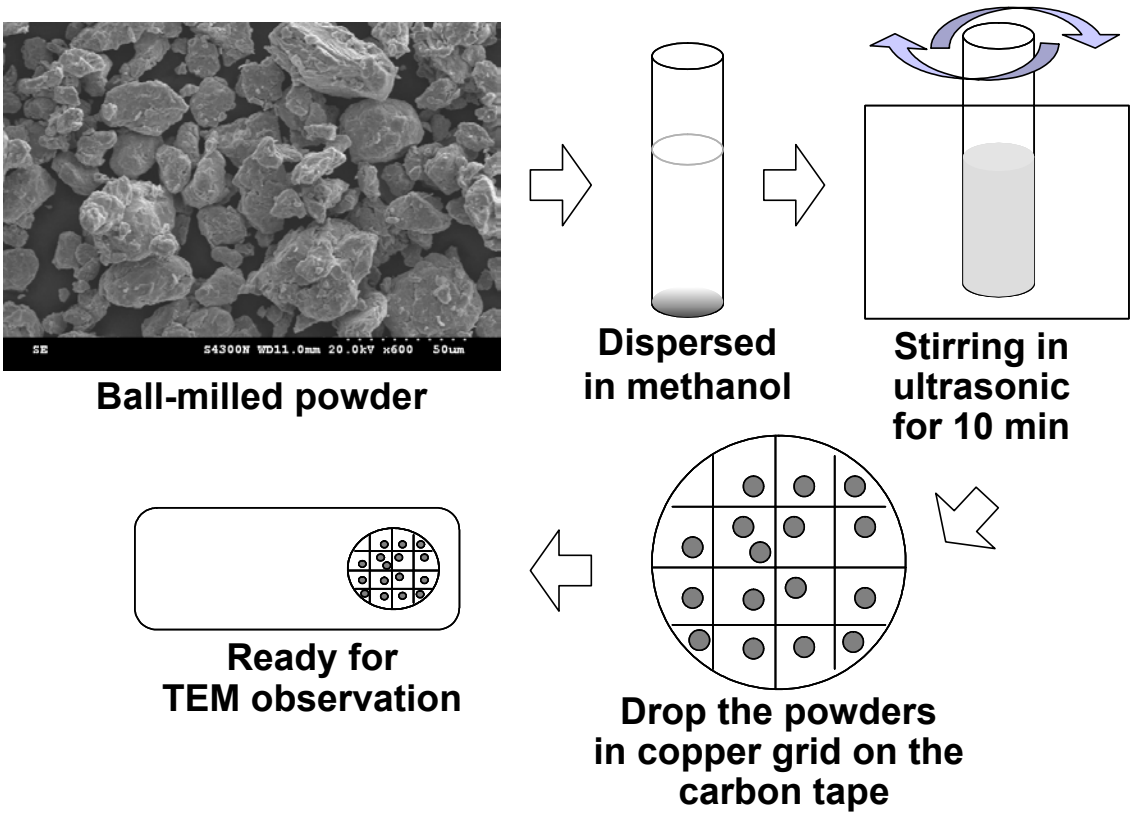

Fig. 26 The procedure of powder preparation for the TEM observation

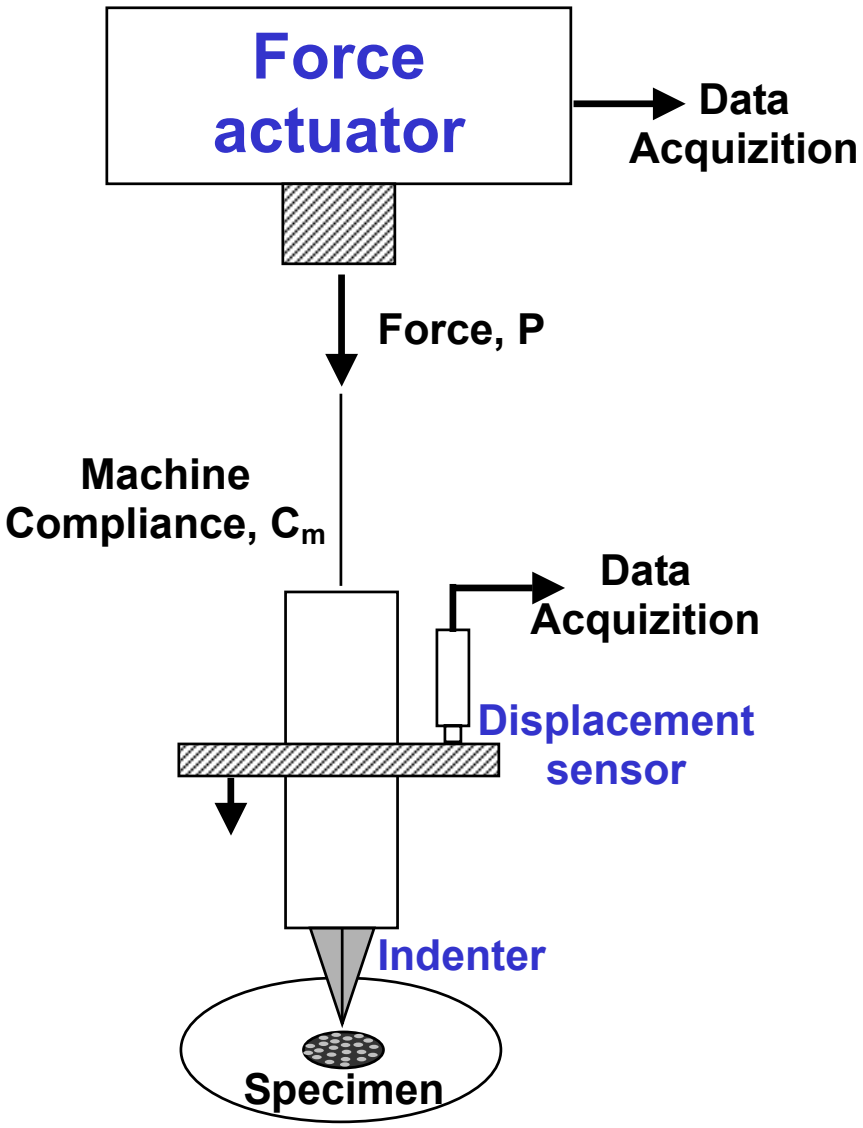

Fig. 27 Schematic of nanoindentation system [3]

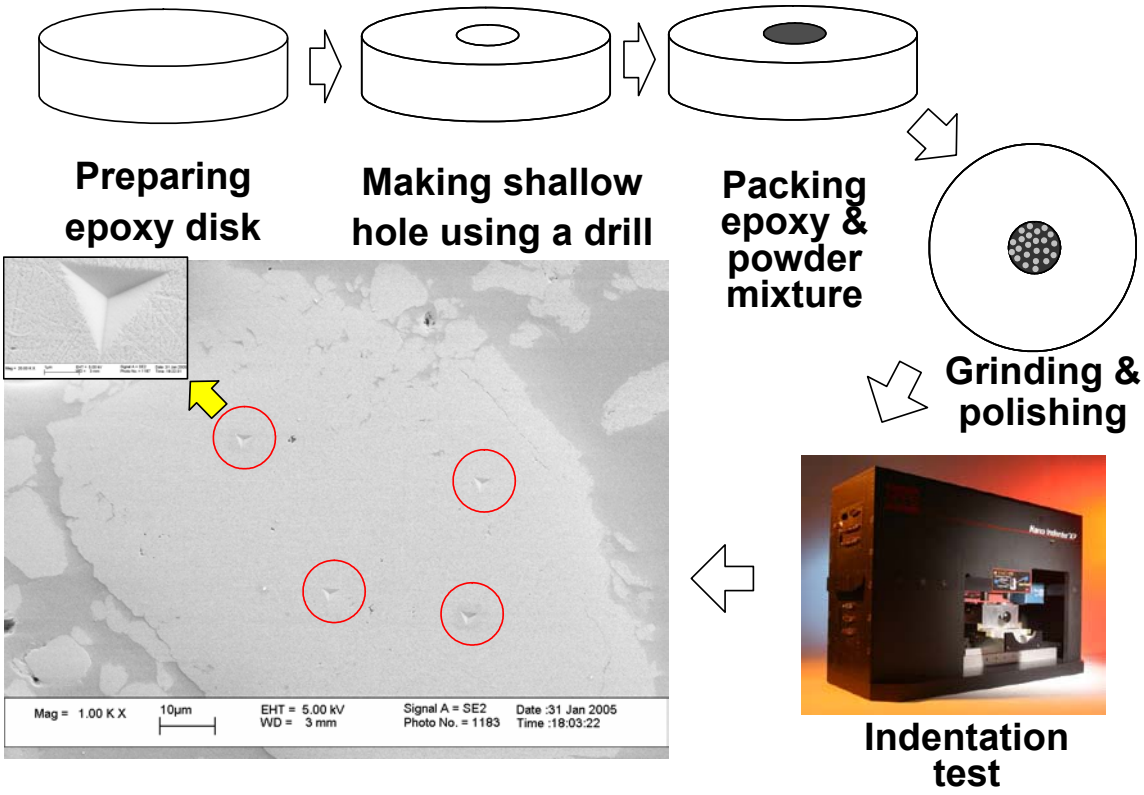

Fig. 28 Powder specimen preparation for nanoindentation test

Fig. 29 Wedge grips and flat tensile specimens used in ENGIN-X

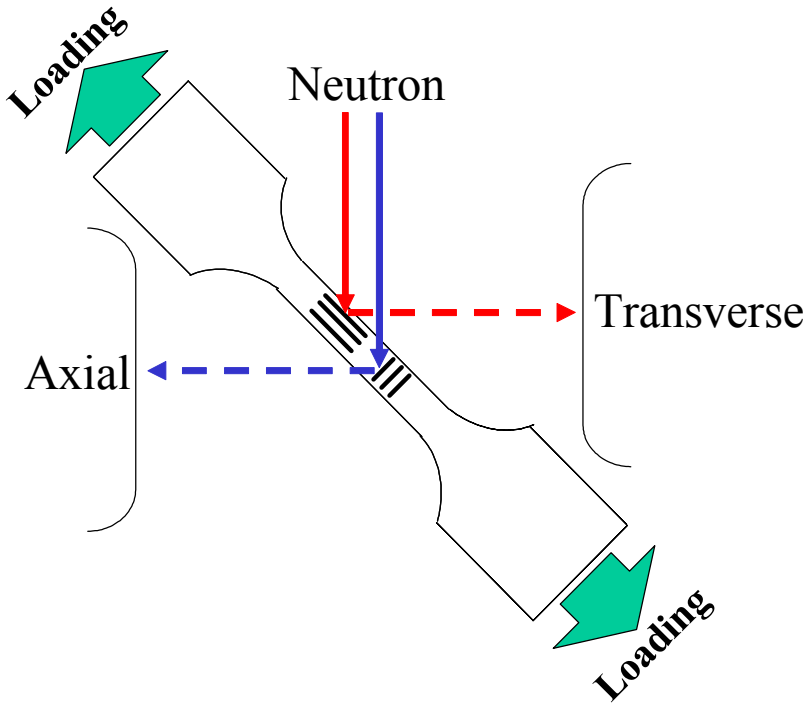

Fig. 30 Scattering geometry illustrating the sample orientation with respect to the neutron beams during *in-situ* loading measurements

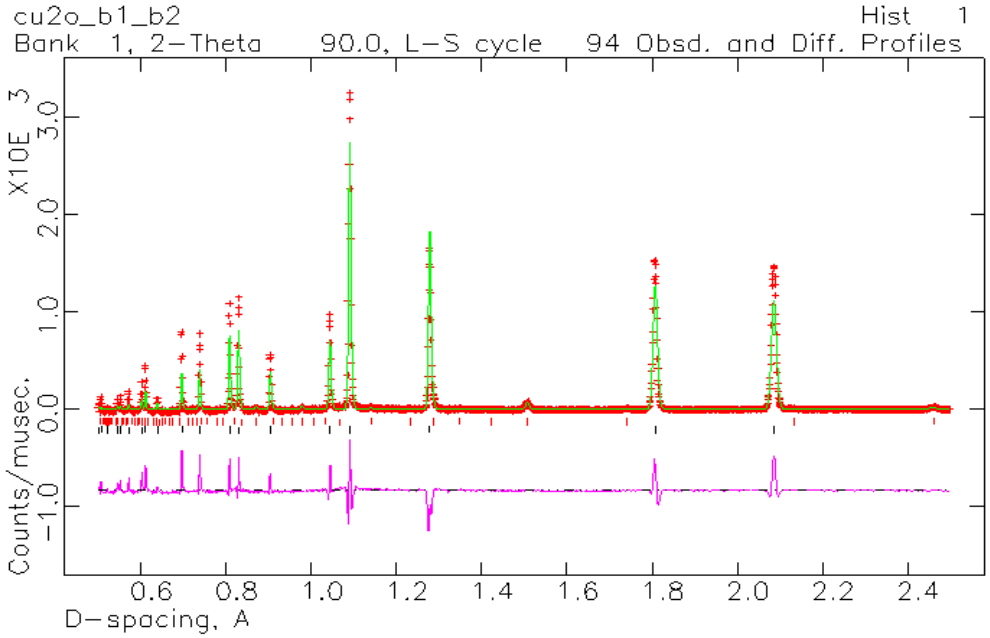

(a) Transverse direction

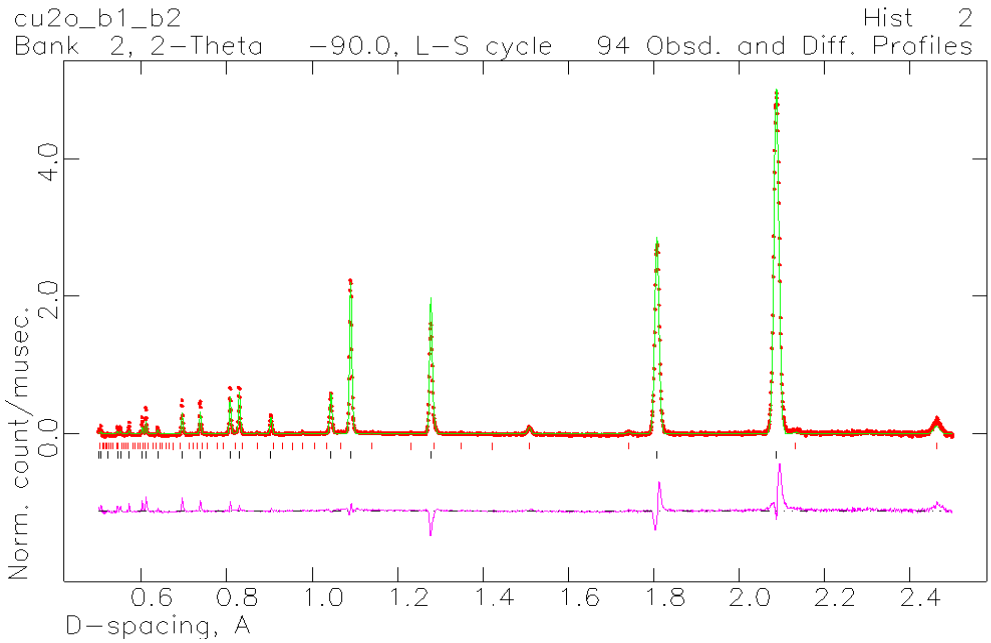

(b) Axial direction

Fig. 31 Rietveld fitted diffraction patterns of pure Cu (a) transverse; (b) axial direction

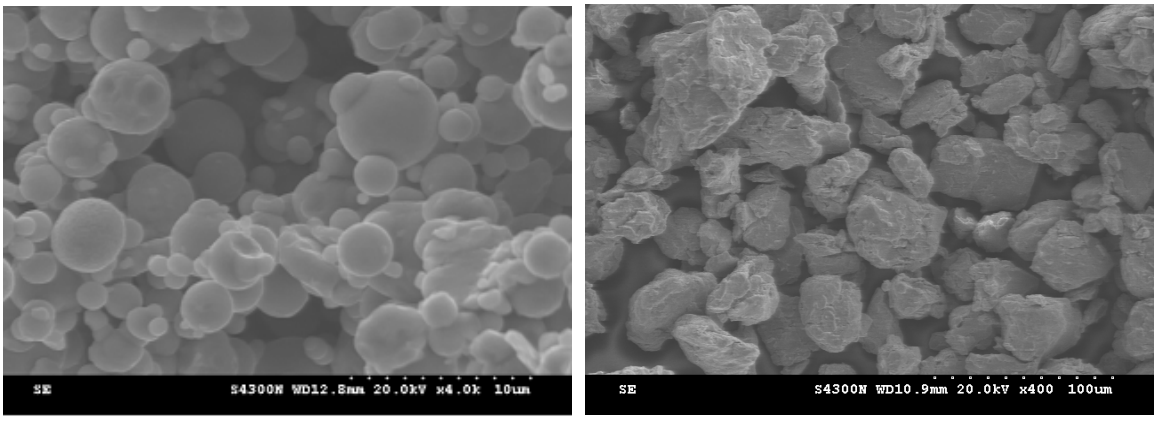

Fig. 32 Fe particle morphology changes as a function of milling time.

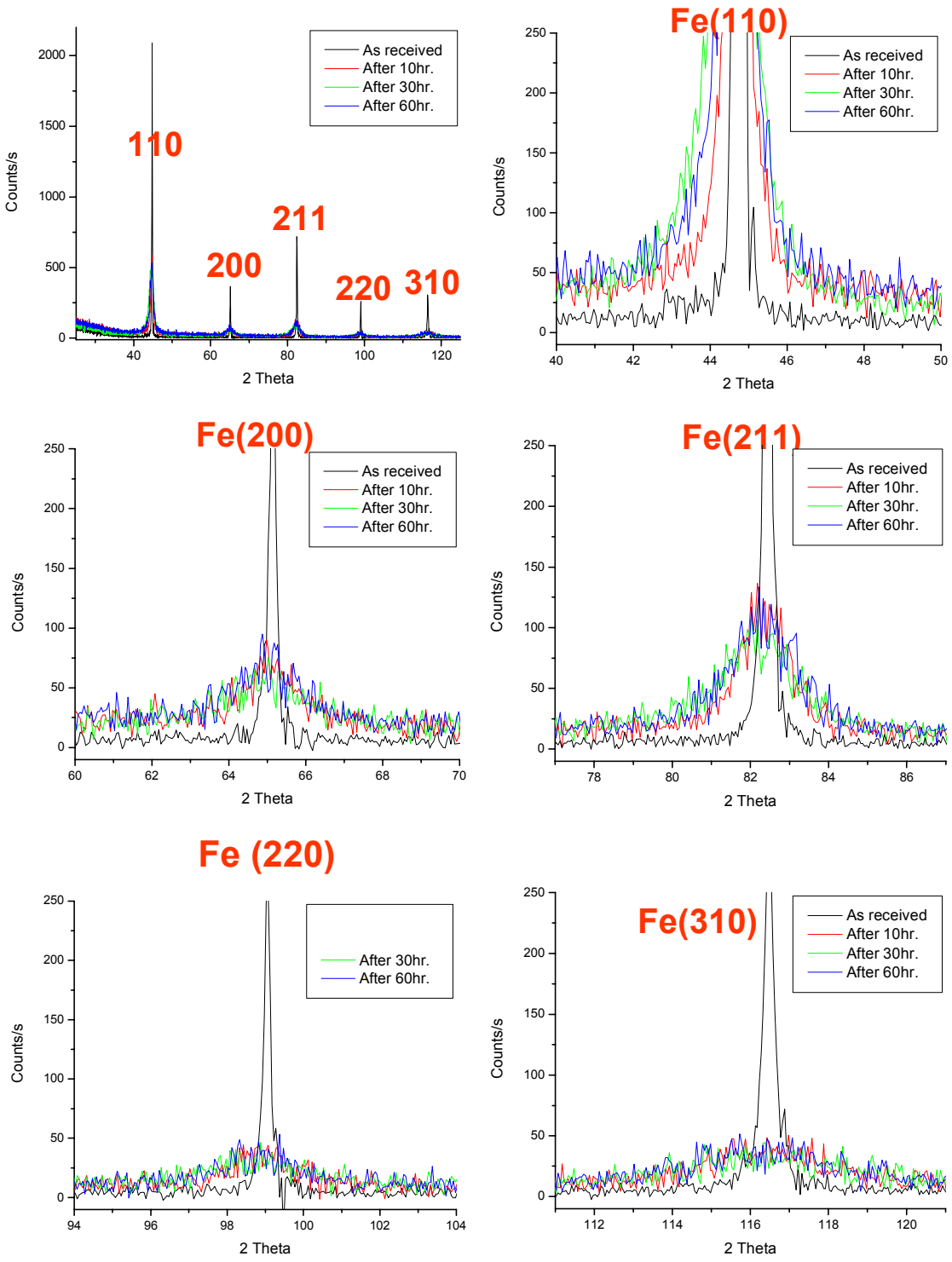

Fig. 33 Changes of peak shape as a function of the milling time

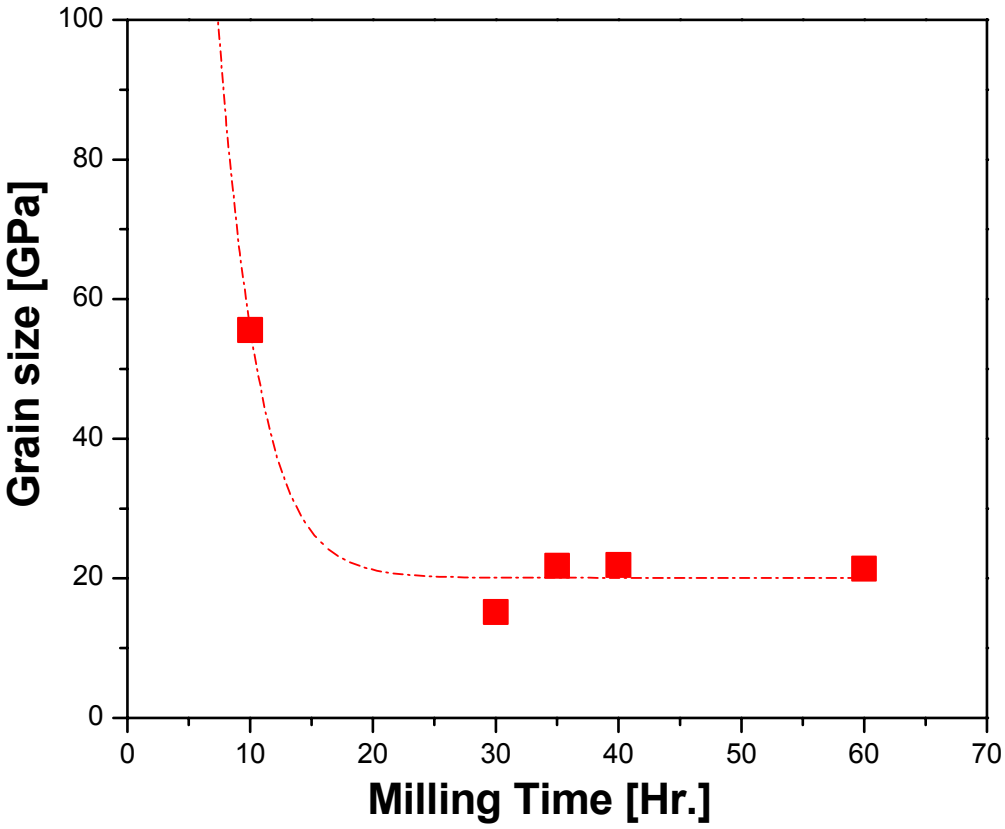

Fig. 34 Grain size vs. ball-milling time

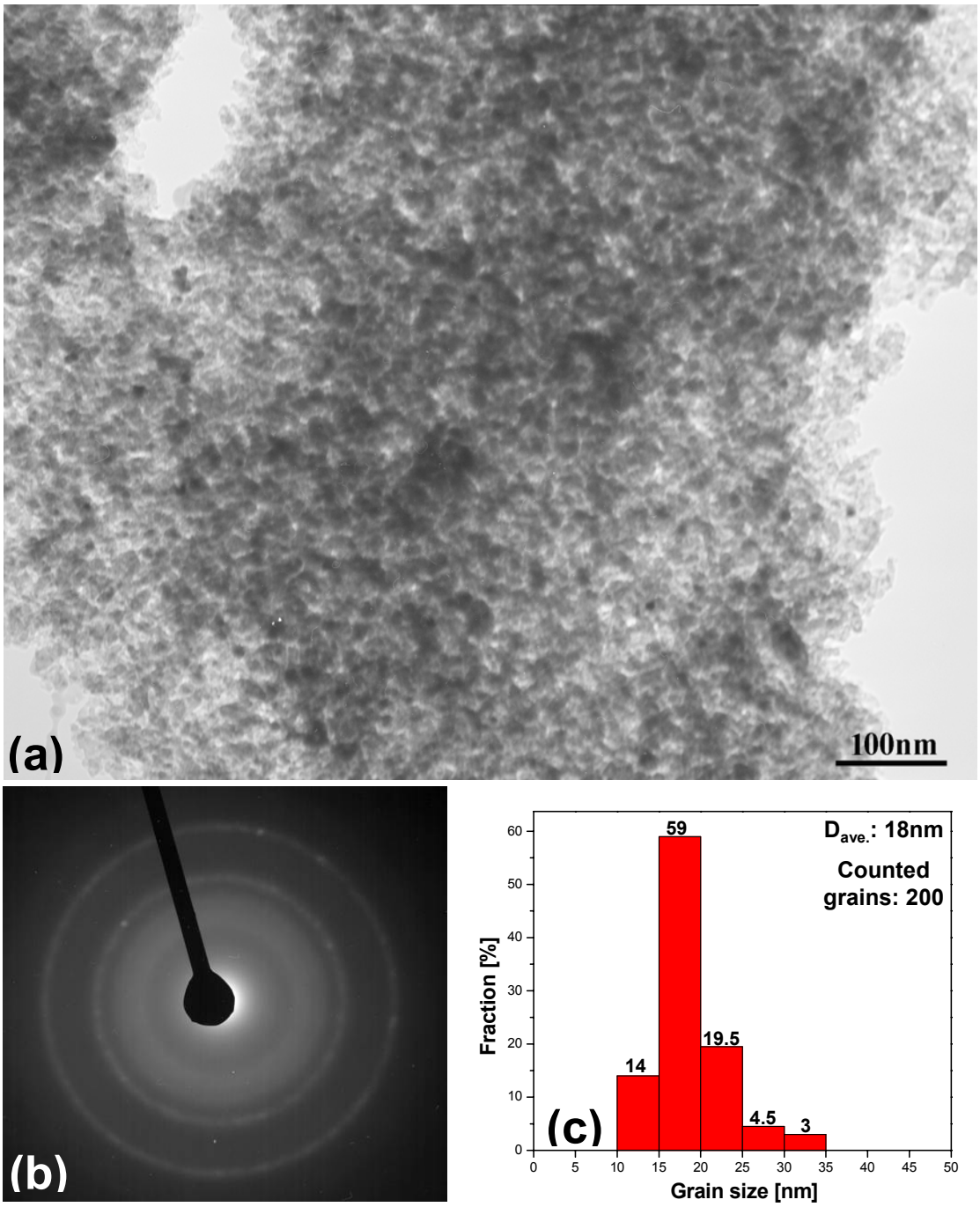

Fig. 35 TEM picture of the 30-hr ball-milled Fe powder (a), the diffraction pattern (b), and the grain size distribution (c)

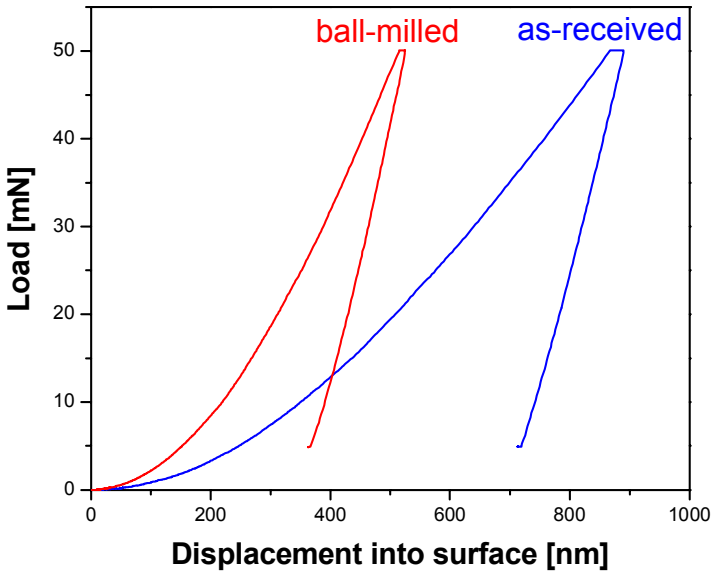

Fig. 36 (a) Load vs displacement curve of two sample which as received (blue) and 30hr ball milled (red) powder

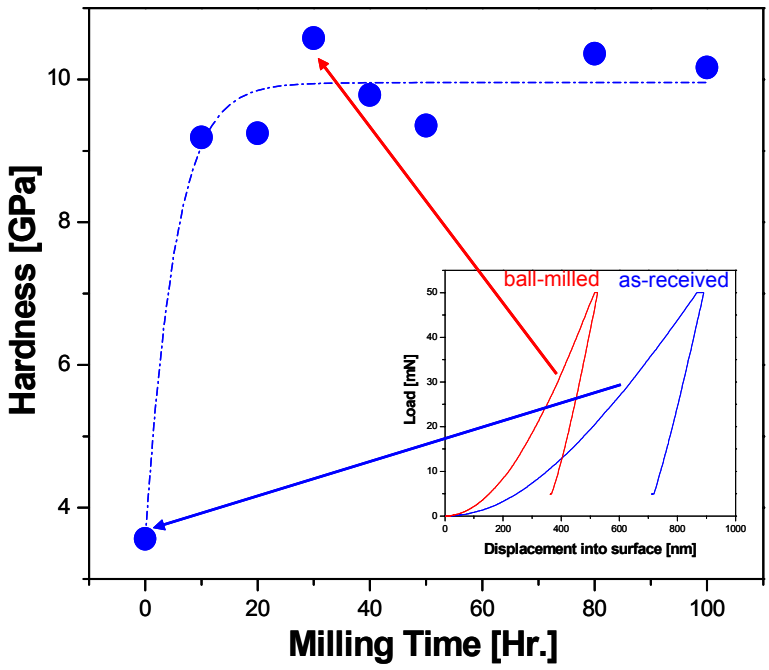

Fig. 36 (b) Grain size vs. ball-milling time

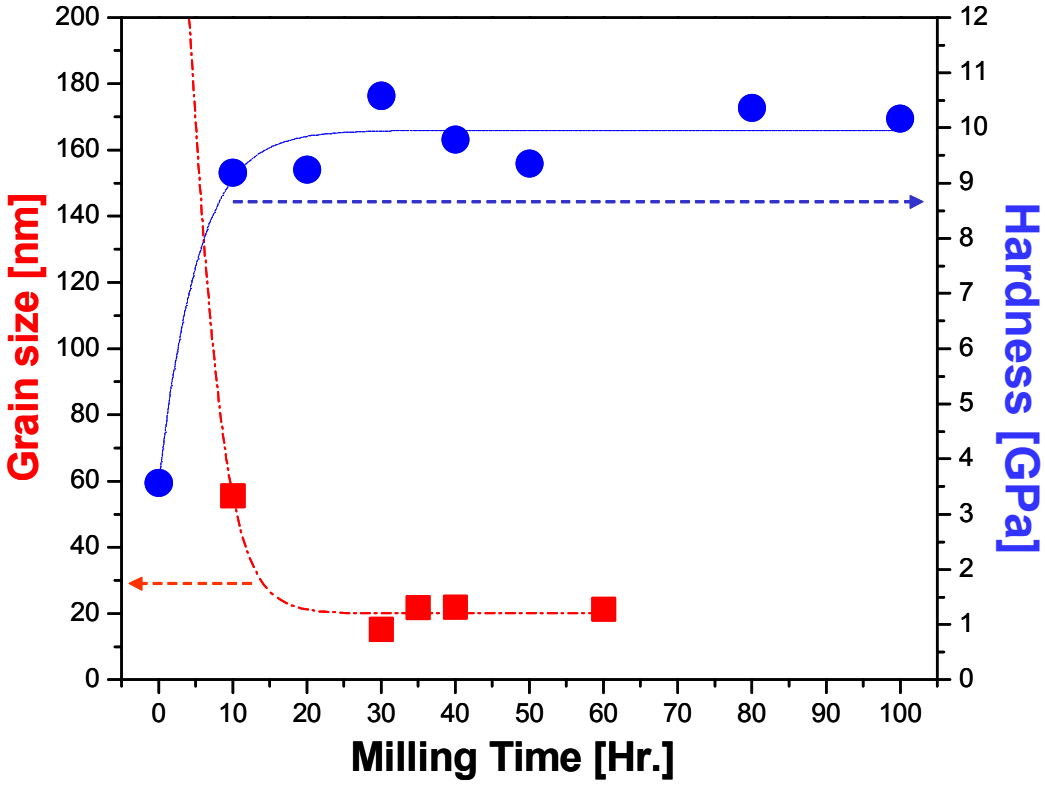

Fig. 37 (a) Grain size and hardness vs. ball-milling time.

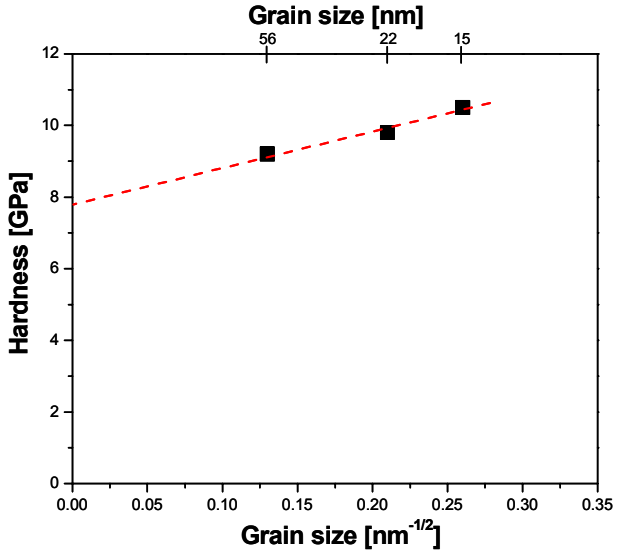

Fig. 37 (b) Grain size vs. hardness of ball-milled Fe

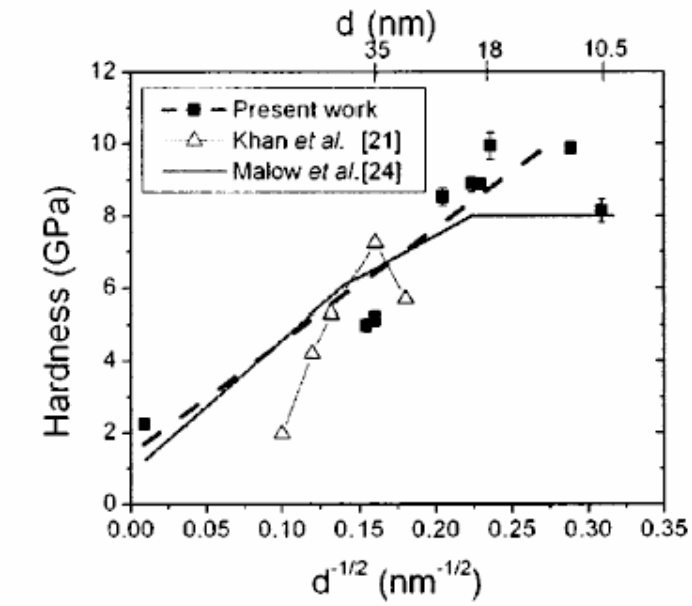

Fig. 38 Hardness of nanocrystalline Fe as a function of $d^{-1/2}$, where d is the volume-averaged grain size.
D. Jang, M. Atzmon, Grain-size dependence of plastic deformation in nanocrystalline Fe, Journal of applied physics, vol. 93, no.11, 1 June 2003

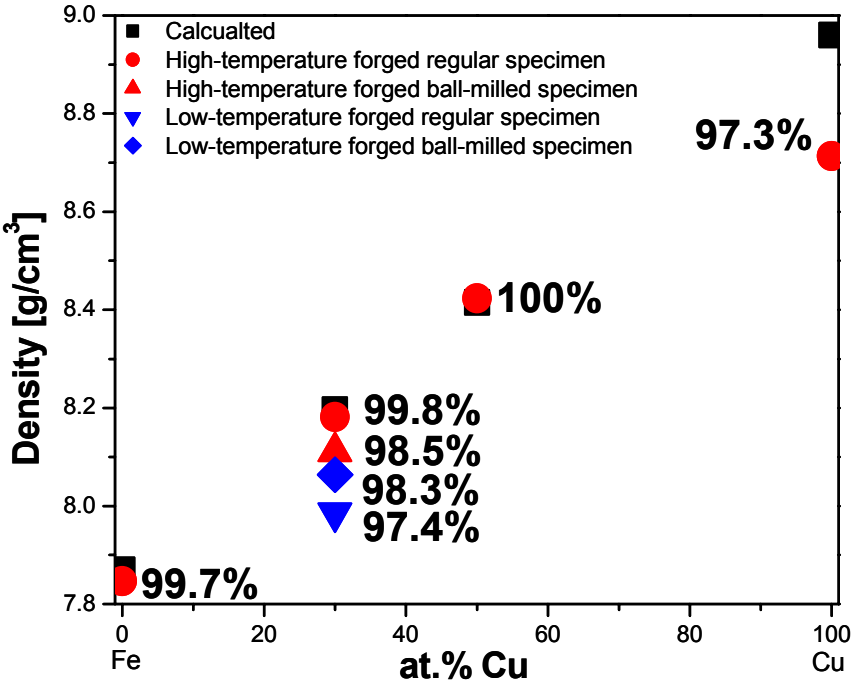

Fig. 39 Density of seven consolidated specimens

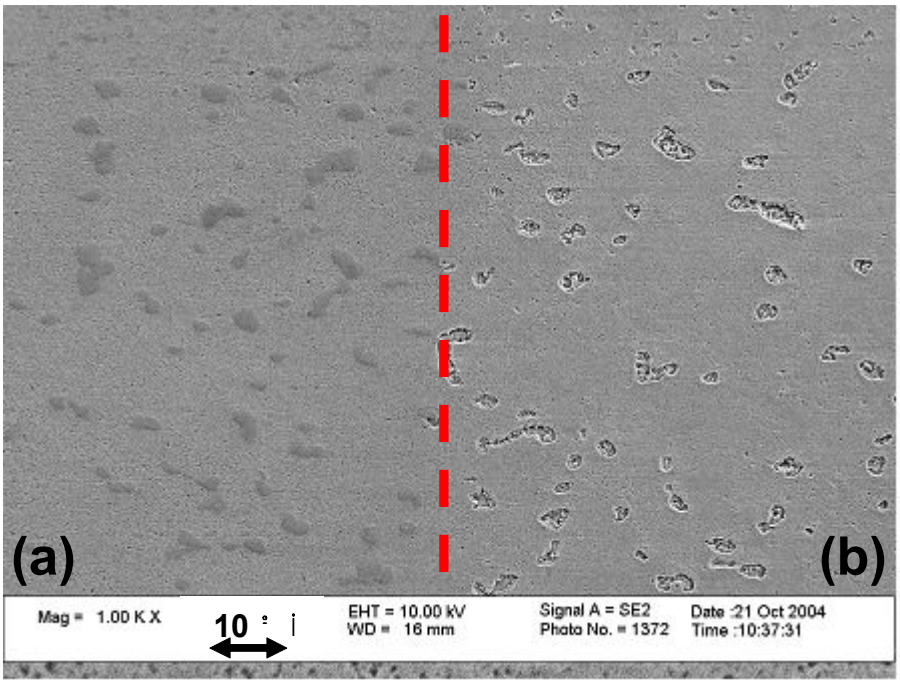

Fig. 40 SEM micrographs of ARCu (a):unetched, (b):etched

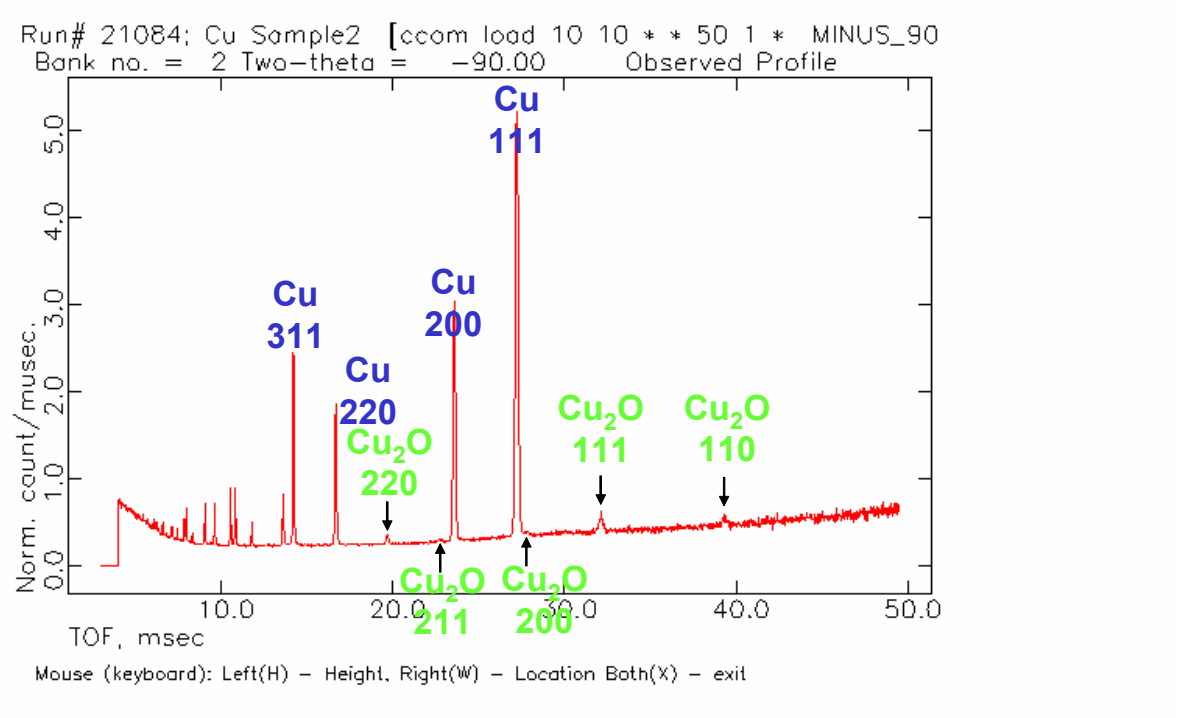

Fig. 41 Neutron diffraction pattern of ARCu

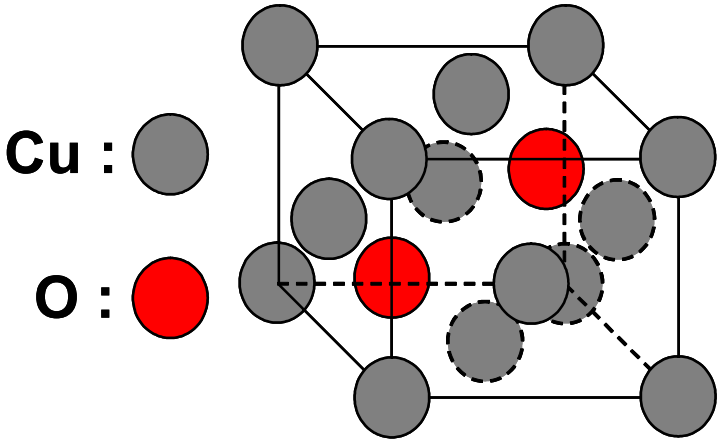

Fig. 42 The crystal structure of Cu_2O

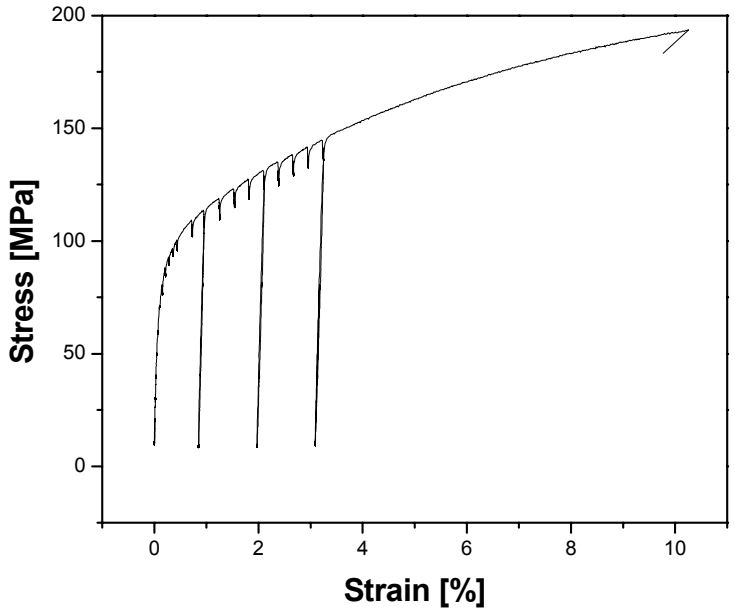

Fig. 43 Engineering stress-strain curve of ARCu

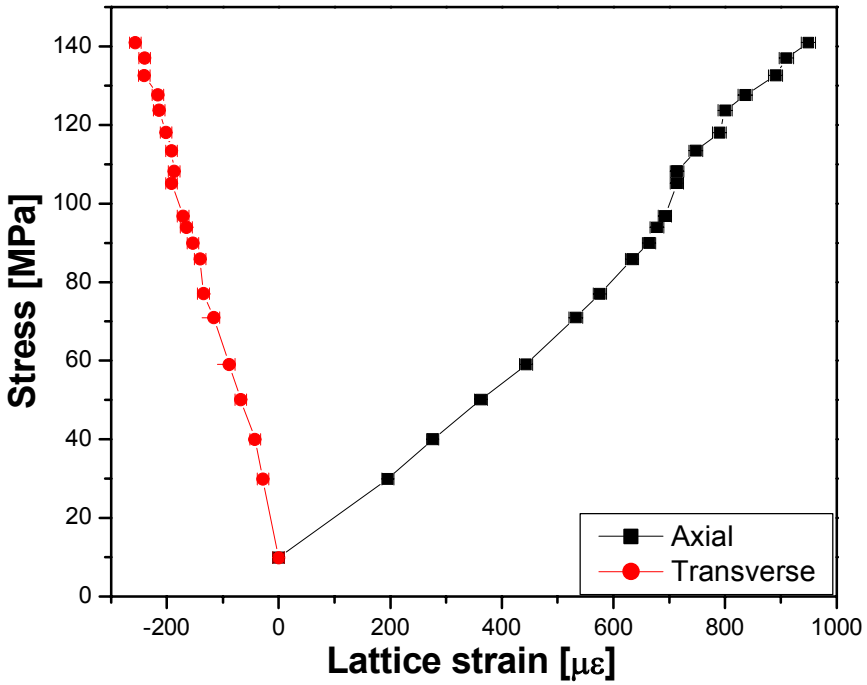

Fig. 44 Lattice strain response of the Cu phase in the ARCu

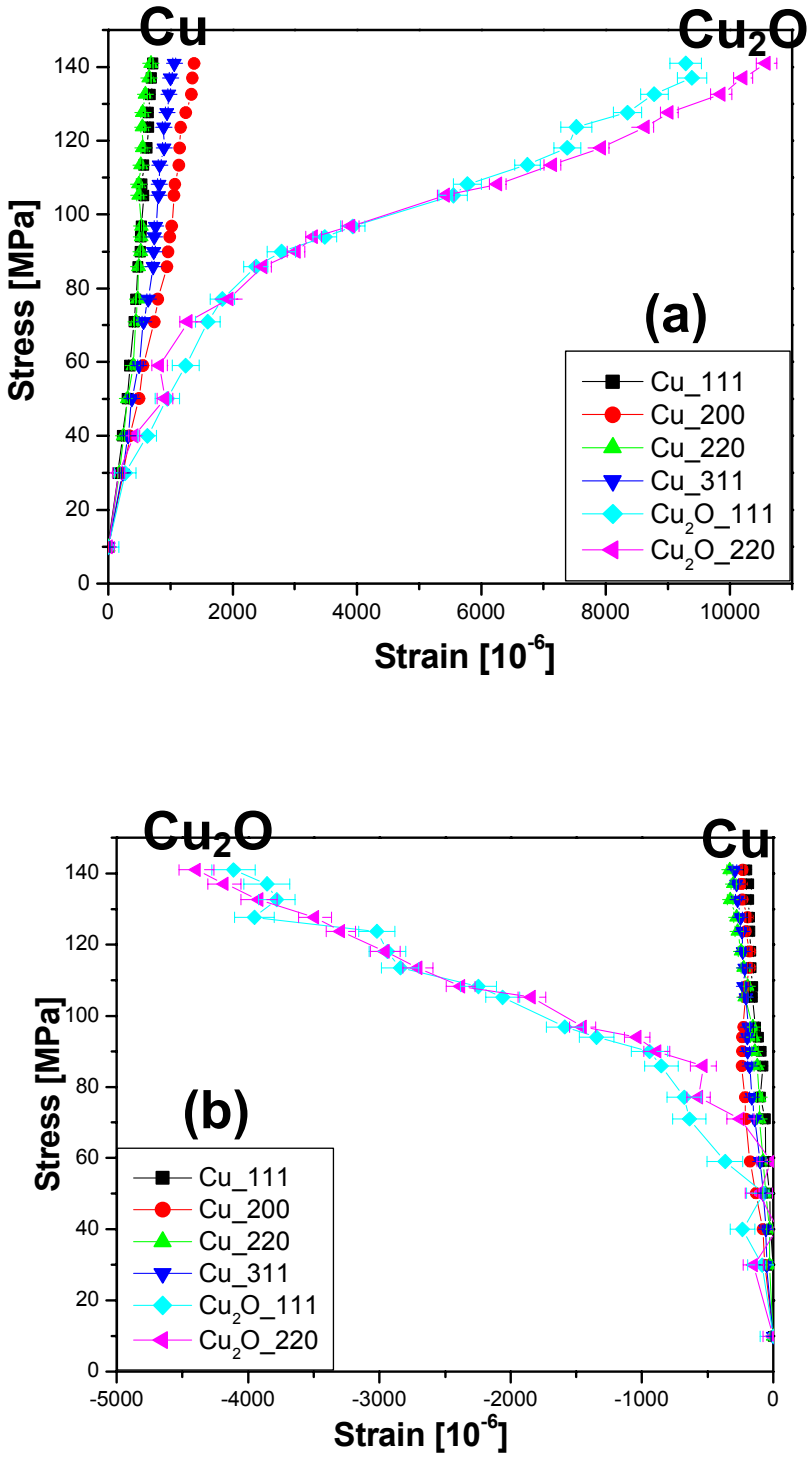

Fig. 45 Lattice strains of Cu & Cu2O phase in the ARCu: (a) transverse direction, (b) axial direction

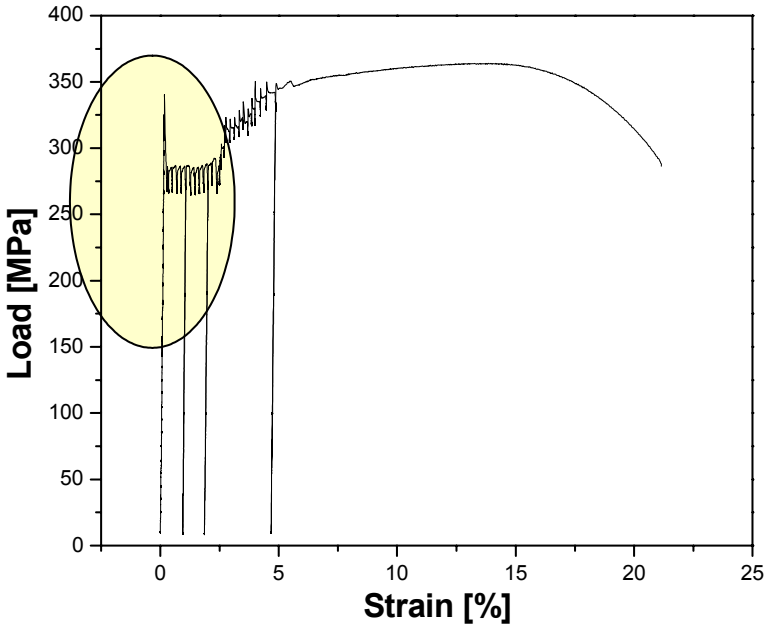

Fig. 46 (a) Overview of macroscopic stress strain response

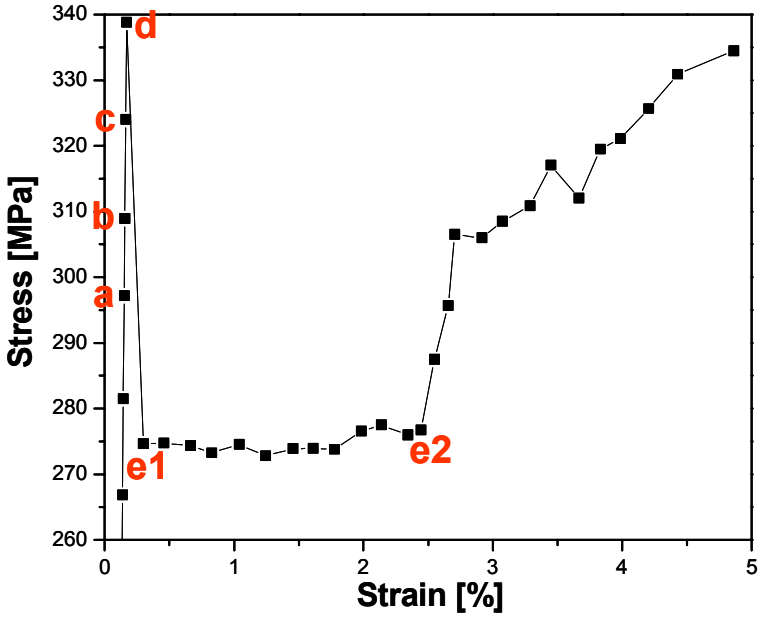

Fig. 46 (b) Detail of macroscopic stress strain response

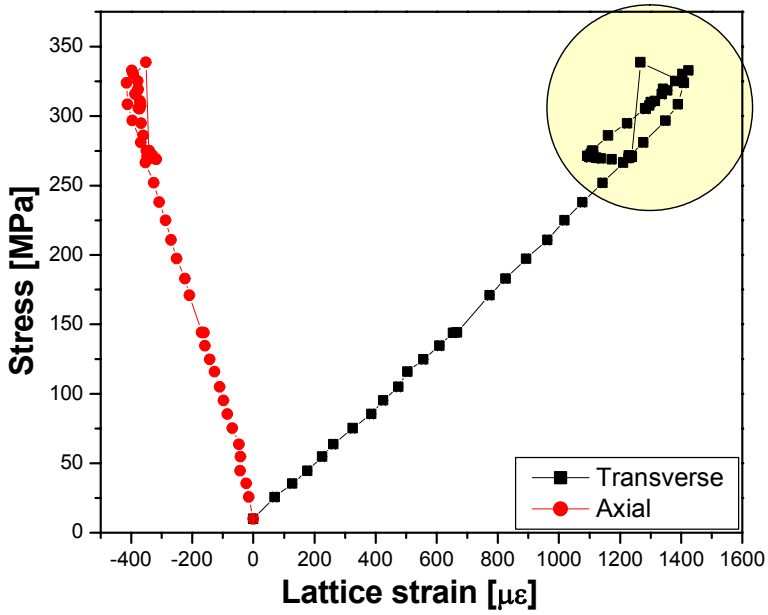

Fig. 47 (a) The lattice strain change of ARFe in transverse and axial direction

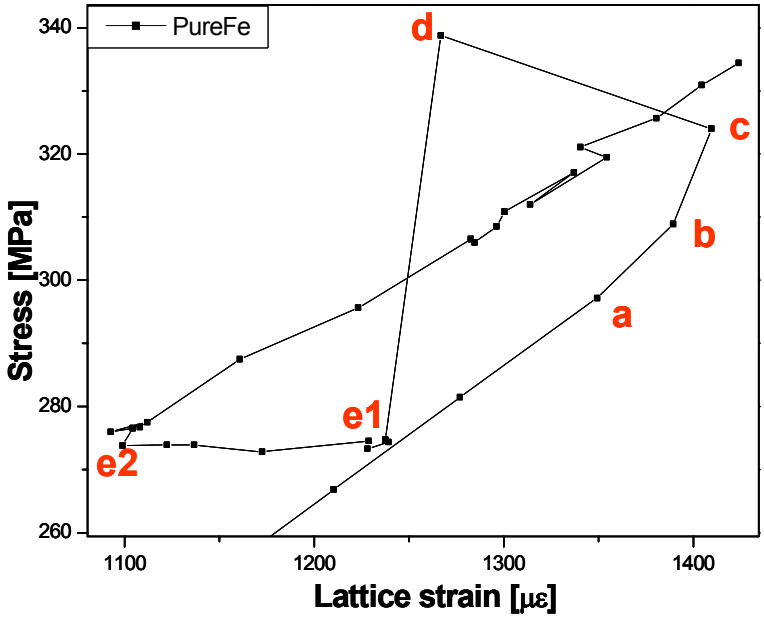

Fig. 47 (b) The lattice strain change of ARFe: the magnified yielding regions in the axial direction

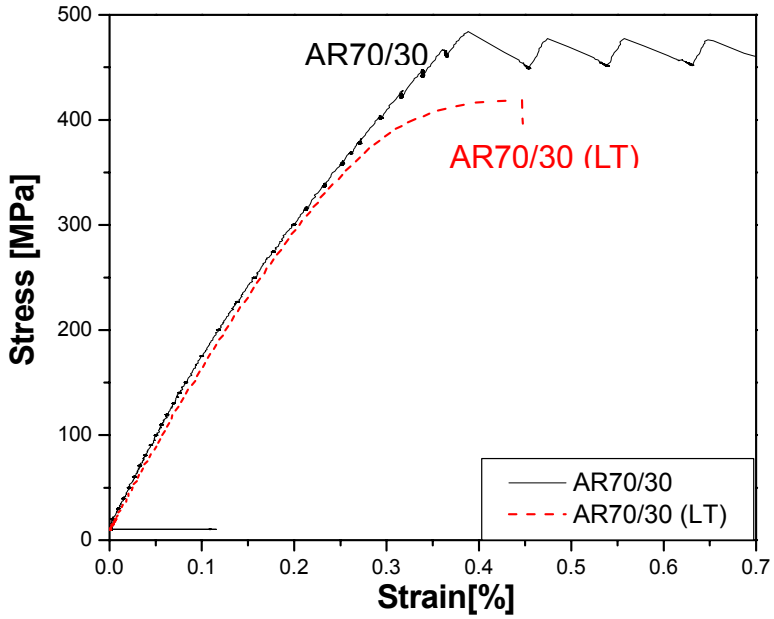

Fig. 48 The tensile behavior of AR70/30 and AR70/30 (LT)

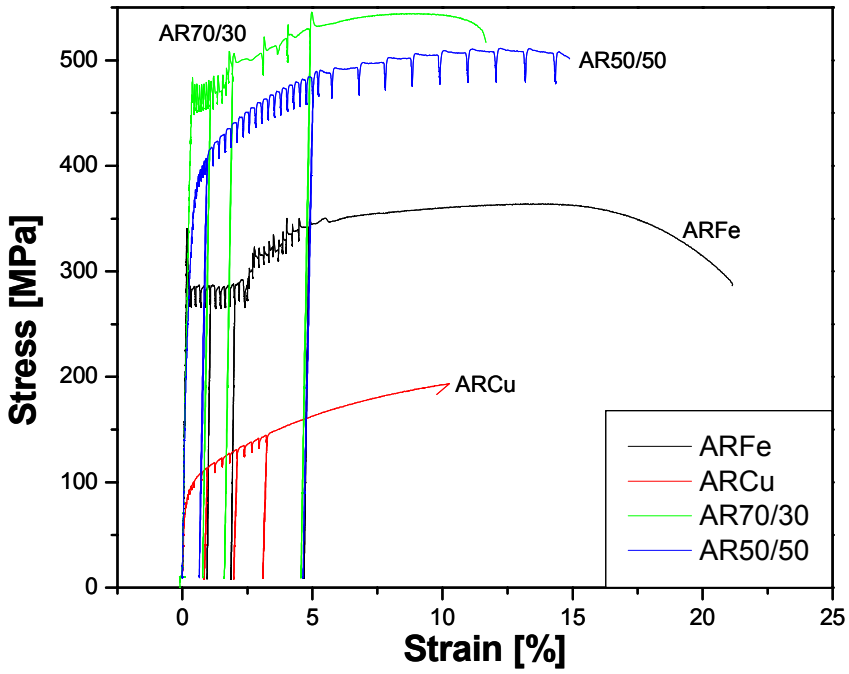

Fig. 49 The tensile behavior of ARFe, ARCu, AR70/30, and AR50/50

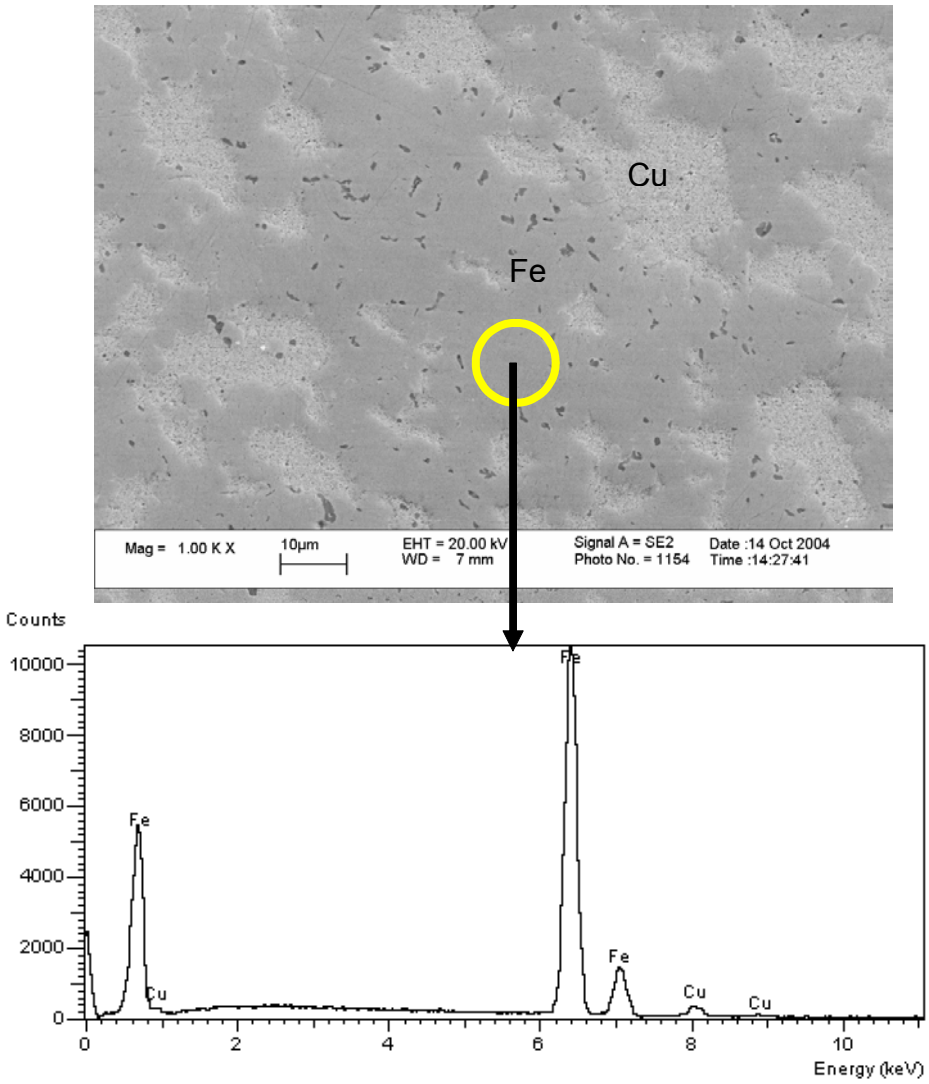

Fig. 50 EDX result from Fe matrix phase in AR70/30 specimen

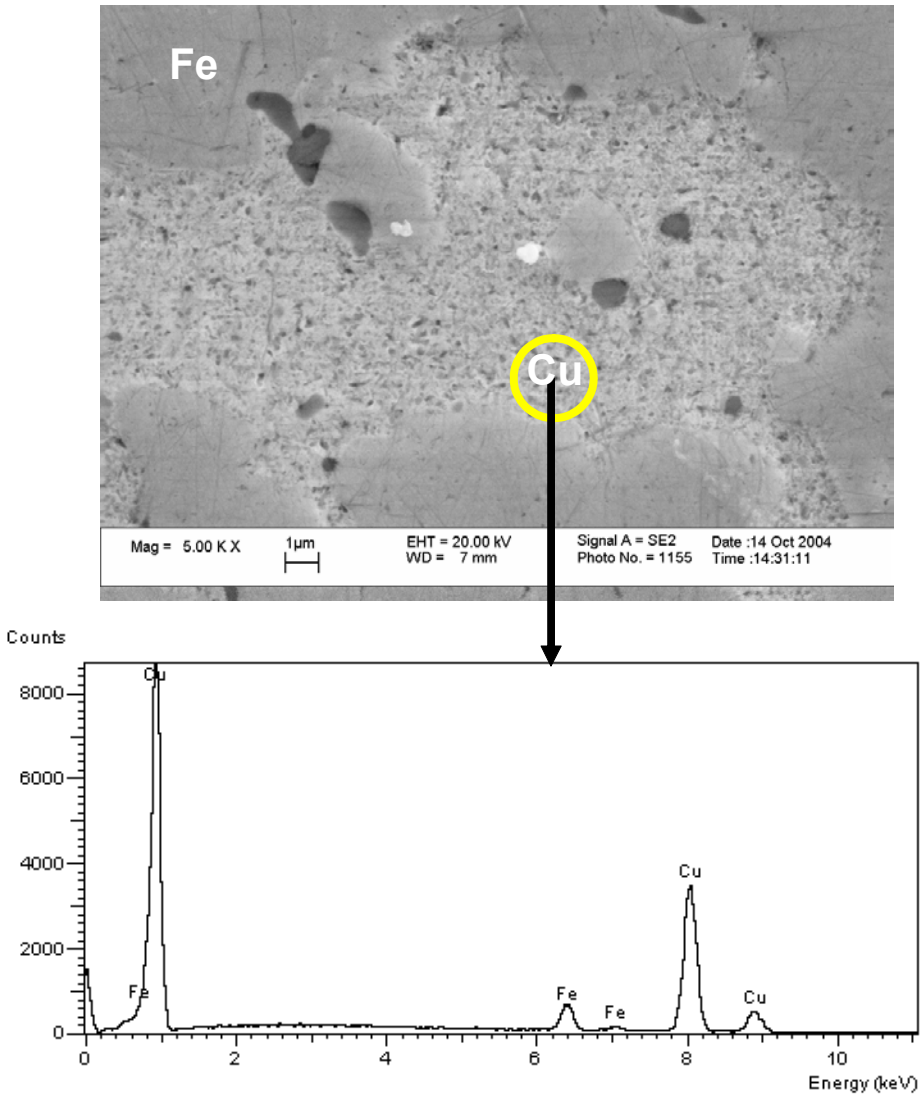

Fig. 51 EDX result on Cu phase in AR70/30 specimen

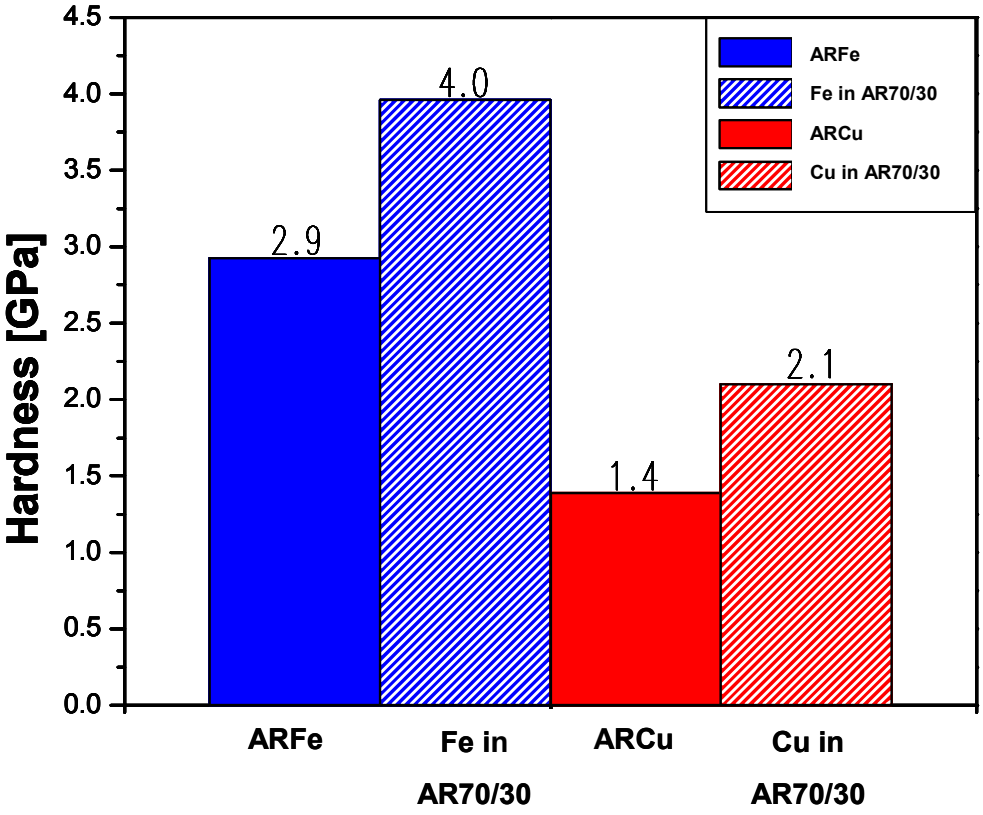

Fig. 52 The nanoindentation results of AR70/30 specimen

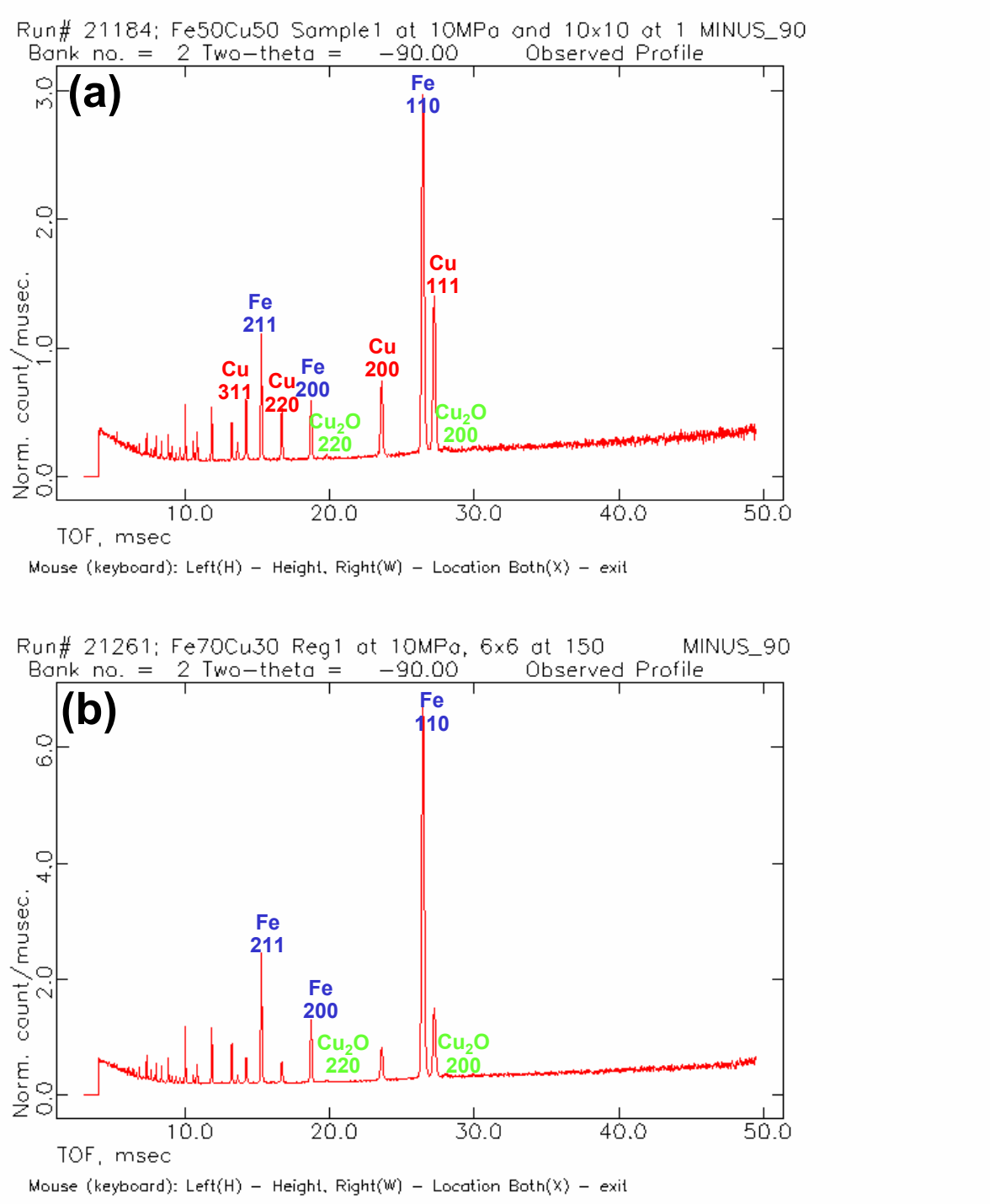

Fig. 53 Neutron diffraction patterns of AR50/50 (a) and AR70/30 (b)

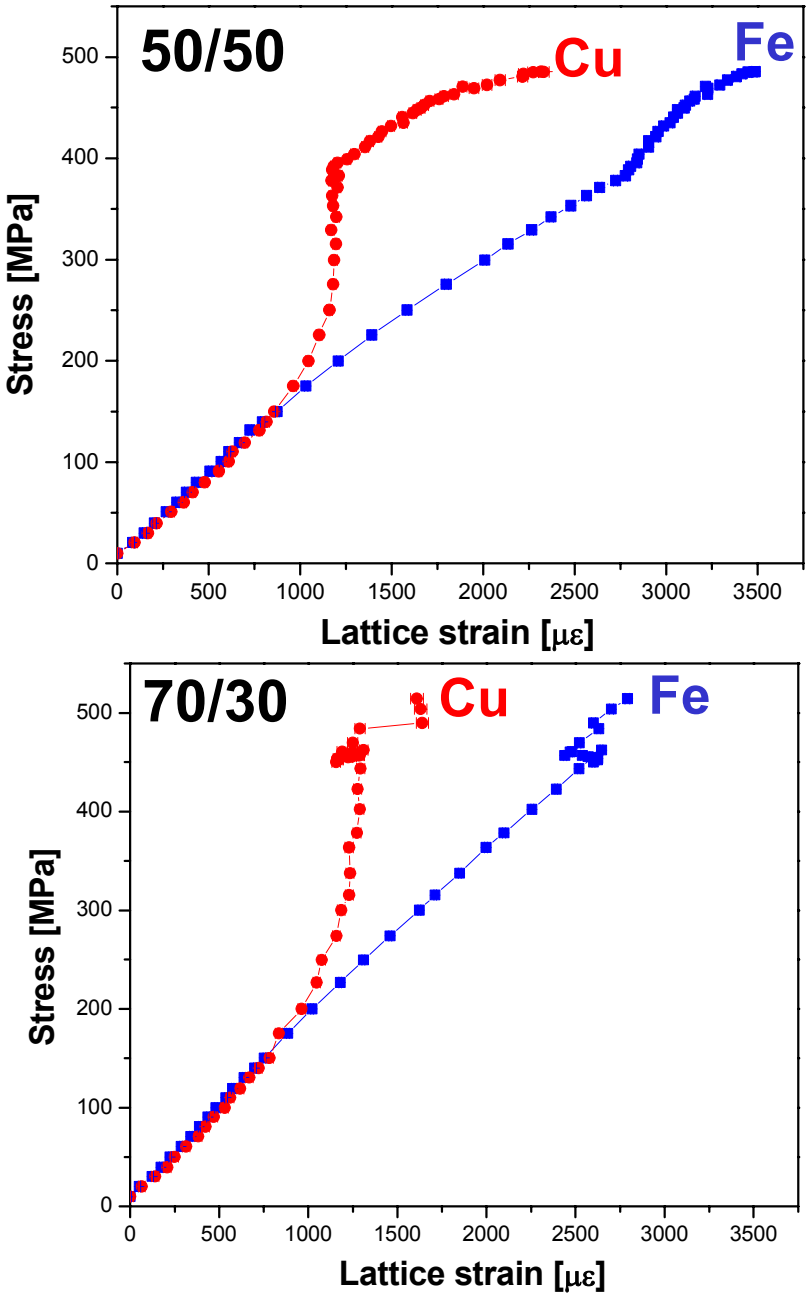

Fig. 54 Lattice strains of Fe & Cu in AR50/50 and AR70/30

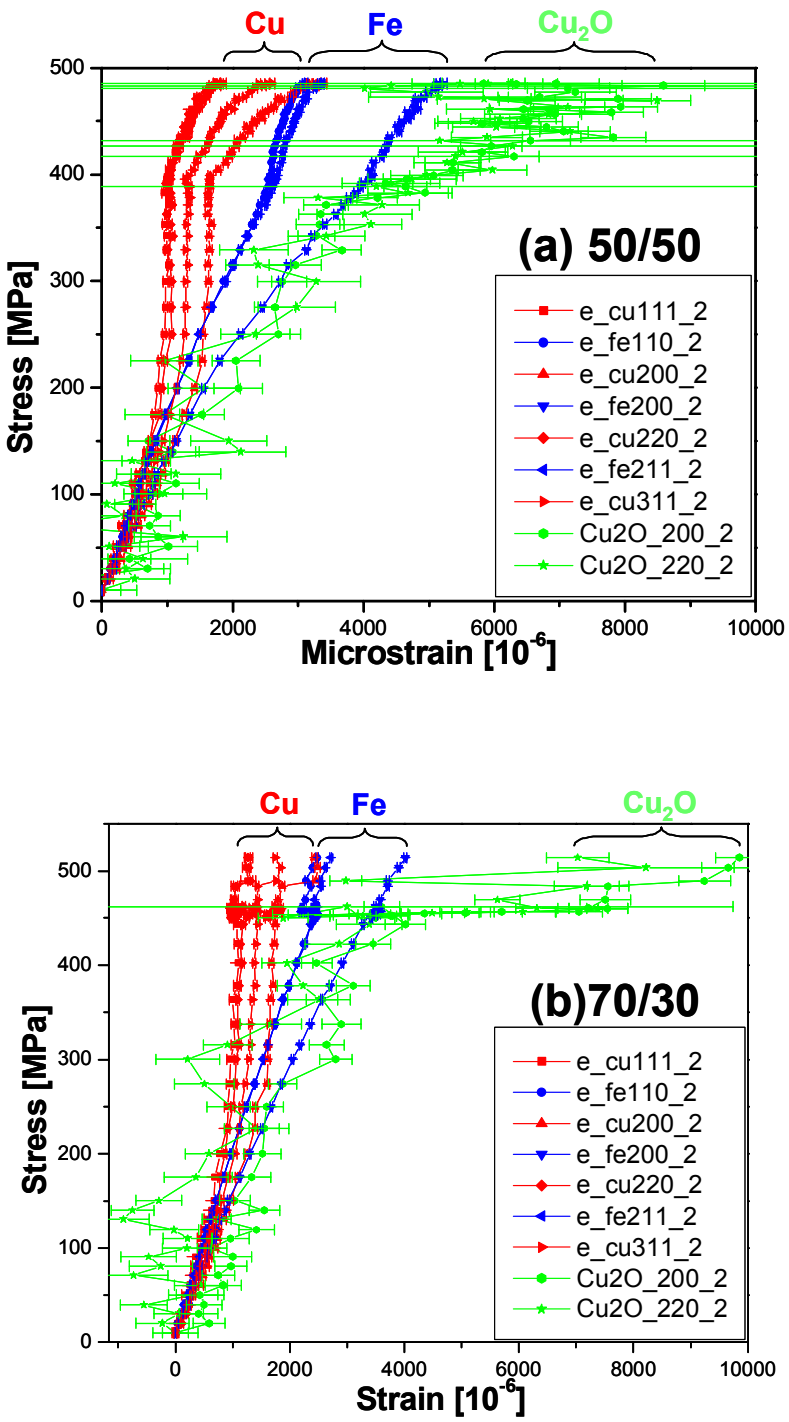

Fig. 55 Axial single peak strains in Fe, Cu, and Cu2O phases in (a) AR50/50 and (b) AR70/30 composites

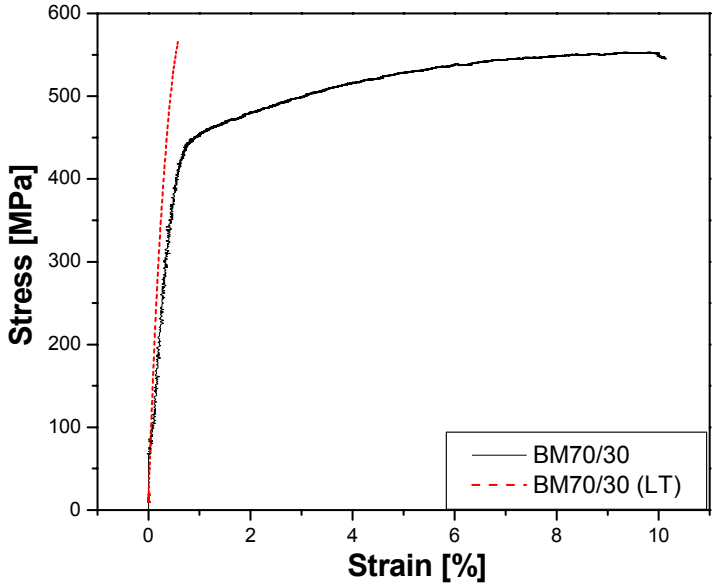

Fig. 56 The tensile behavior of BM70/30 and BM70/30(LT)

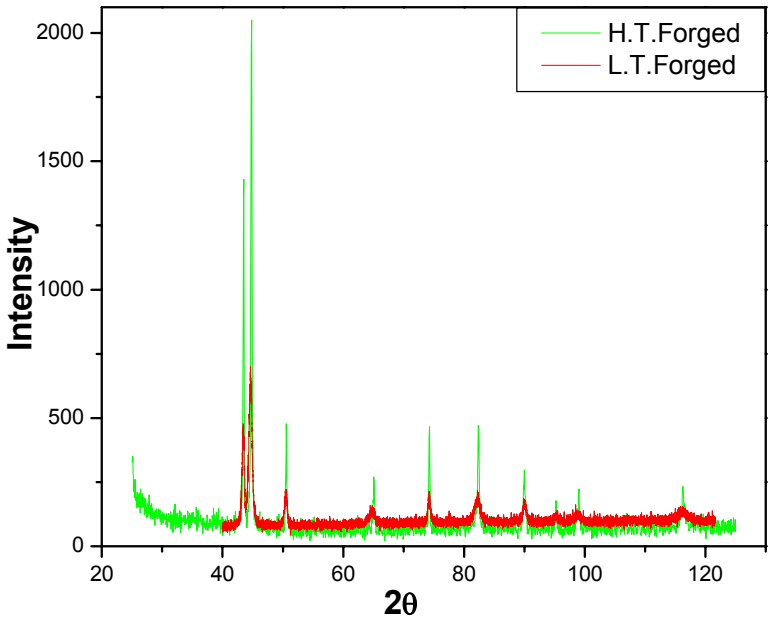

Fig. 57 XRD patterns of HT forged and LT forged of composites

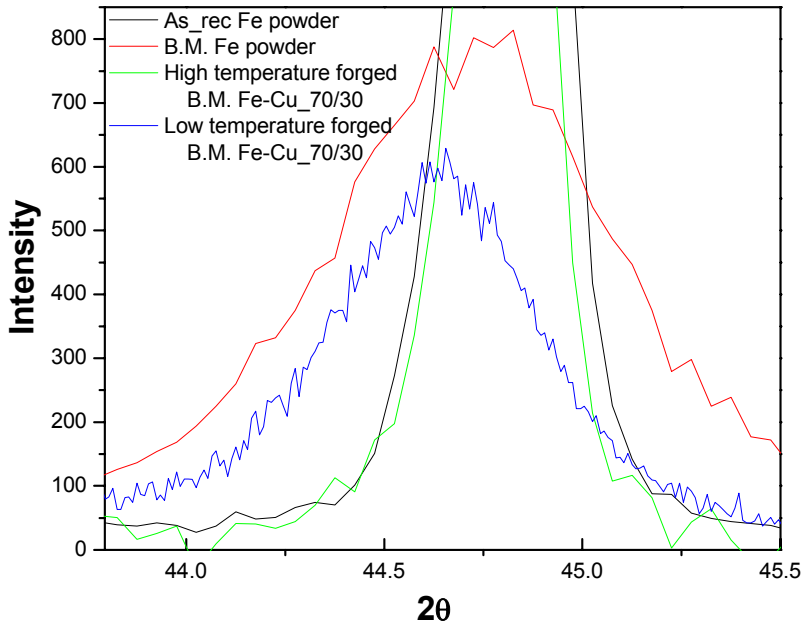

Fig. 58 110 reflection measured from four specimens. ARFe (P), BMFe (P), BM70/30, and BM70/30 (LT)

Vita

Jin-woo Jeon was born in Busan, South Korea in 1977. During his 7 years college periods (1996-2003), he spent 2 years and 2 months in the Korean Army for the mandatory military service. In the February 2003, he received his bachelor degree in Materials Science and Engineering at Sungkyunkwan University, Seoul, South Korea.

He started his Master's program in the Material Science and Engineering Department, University of Tennnessee, U.S.A. in August 2003. The Master's degree is expected in December 2005.